ABSTRACT

Title of dissertation: Measurement of radiation pressure and tailored momentum transfer through switchable photonic devices

Dakang Ma, Doctor of Philosophy, 2016

Dissertation directed by: Professor Jeremy N. Munday
Department of Electrical and Computer Engineering

Light carries momentum, which can be transferred to an object upon reflection or absorption. The resulting force per unit area from light, so called radiation pressure, is rather weak but can have macroscopic consequences. For example, sunlight imparts momentum on dust particles causing a comet's tail to be directed away from the sun. In a microscopic world, micro/nano-mechanical transducers have become sensitive enough that radiation pressure can influence them greatly. However, photothermal effects often accompany and overwhelm the radiation pressure, complicating its measurement. In this thesis, we first show a quantitative measurement of the radiation force on an uncoated silicon nitride microcantilever in an ambient condition. We identify and separate the radiation pressure and photothermal effects through an analysis of the cantilever's frequency response. Further, we demonstrate the first measurement of a wavelength-dependent radiation pressure due to optical interference in a silicon microcantilever. We utilize an in-situ optical transmission measurement at the excitation position to determine the local optical properties.

Another interesting application of radiation pressure is a solar sail. Solar sails use solar radiation pressure for propulsion and offer an opportunity for propellant-free space travel, enabling long-term and long-distance missions that are impossible with traditional methods. Although solar sail propulsion alleviates the need to carry chemical fuel, attitude control and steering are still performed using traditional methods involving reaction wheels and propellant ejection. In the second part of the thesis, we present a steerable solar sail concept based on a polymer dispersed liquid crystal (PDLC) device that switches between transparent and scattering states, enabling attitude control without mechanically moving parts or chemical propellant. Devices are fabricated and characterized (transmission, reflection, absorption and scattering) over the visible and near infrared range of the solar spectrum (400 nm - 1100 nm) and are found to outperform previous designs by more than a factor of four in terms of over-all weighted momentum switchablility between on and off states. Devices require no power in the diffusely reflective state and dissipate less than 0.5 mW/cm^2 while in the on state, showing great potential as a low-power switching mechanism for solar sail attitude control.

Measurement of radiation pressure and tailored momentum transfer through switchable photonic devices

by

Dakang Ma

Dissertation submitted to the Faculty of the Graduate School of the
University of Maryland, College Park in partial fulfillment
of the requirements for the degree of
Doctor of Philosophy
2016

Advisory Committee:
Professor Jeremy N. Munday, Chair/Advisor
Professor Christopher Davis
Professor Thomas Antonsen
Professor Raymond Sedwick
Doctor Henri Lezec

© Copyright by
Dakang Ma
2016

Acknowledgments

More than four years of graduate research at the Munday Lab has been a challenging but rewarding journey. I owe my gratitude for all the people who supported me along the way that have made this thesis possible. This is an unforgettable experience that I will cherish for the rest of my life.

First and foremost, I'd like to thank my advisor, Professor Jeremy N. Munday for giving me this opportunity to work on this challenging but interesting project and guiding me all the way through my doctoral study. His broad knowledge and unique insight into various research fields have always enlightened me. His patience and positive attitude have always been the motivation for me to tackle the challenges. It has been a real pleasure and blessing to work with and learn from such an extraordinary individual.

I would also like to thank Professor Christopher Davis, Professor Thomas Antonsen, Professor Raymond Sedwick and Doctor Henri Lezec for serving on my thesis committee and for sparing their time reviewing this thesis.

I want to thank all the members of the Munday Lab, who have made my time at work a joyful day everyday. Especially, I would like to thank Joe Garrett for getting me started on using the atomic force microscope and providing his detailed knowledge about the instrument, David Somers for the insightful discussions about various interesting problems that inspire me to think outside the box, Joe Murray for helping me building up experimental setups and Tao Gong and Yunlu Xu for helping me with the nanofabrication.

I wish to thank Dr. Henri Lezec for his insightful discussions on the radiation pressure measurements a couple of years ago and his postdoc back then, Dr. Ting Xu for fabricating nanostructures on cantilevers for us. I would like to thank Professor Marina Leite and Professor Liangbing Hu and their students for their generosity in sharing lab resources and I had a wonderful time collaborating with them. I would also like to thank our collaborators at NASA - Tiffany Russell Lockett, Mary Nehls, Andrew Heaton, and Keats Wilkie for their helpful discussion during our monthly meetings. My sincere gratitude also goes to Dr. Aleks Labuda at Asylum Research for his helpful discussion about photothermal effects and the rainbowDrive setup.

I owe my deepest thank to all my family members, especially my parents, for supporting and caring about me everyday along this journey. I want to thank my girlfriend for always being there for me when I am down and all the friends who have made my years at the University of Maryland a wonderful experience. I am also very grateful for the help from the extraordinary stuff members in IREAP and the Department of Electrical and Computer Engineering.

Lastly, I would like to thank NASA for funding the project through a NASA Early Career Faculty Award (No.NNX12AQ50G) and a NASA Smallsat Technology Partnership Award (No.NNX15AW53A). This thesis could not have been done without their financial support.

Table of Contents

List of Tables vi

List of Figures vii

1 Introduction 1
1.1 A brief history of radiation pressure . . . 1
1.2 The Abraham-Minkowski controversy . . . 4
1.2.1 The classical electromagnetic picture . . . 5
1.2.2 Experiments supporting Minkowski's description . . . 8
1.2.3 Experiments supporting Abraham momentum . . . 9
1.2.4 Other experiments and conclusion . . . 11
1.3 Radiation pressure in space: solar sails . . . 13
1.4 Radiation pressure in nanoscale devices . . . 15
1.5 Outline of Thesis . . . 15

2 Radiation pressure measurement 17
2.1 Quantitative radiation pressure measurement in ambient environment 17
2.1.1 Background and motivation . . . 17
2.1.2 Experimental approach . . . 18
2.1.3 Results and analysis . . . 19
2.2 Wavelength dependent radiation pressure due to thin film interference 26
2.3 Fano-like resonances in optically driven cantilevers . . . 35

3 Cantilever beam theory 41
3.1 Static bending . . . 41
3.2 Cantilever vibration and eigenmodes . . . 43
3.3 Forced vibration under an external force . . . 47
3.4 Forced vibration under an external bending moment . . . 51

4 Photon absorption induced bending 52
4.1 Introduction . . . 52
4.2 Bimetallic bending of a coated cantilever . . . 53
4.2.1 Temperature distribution upon illumination . . . 54

4.2.2 Bending moment and effective force . . . 61
4.3 Temperature and carrier density gradient induced bending . . . 64
4.3.1 Electronic elastic bending from carrier density gradient . . . 65
4.3.2 Thermal-elastic bending from a temperature gradient . . . 70
4.3.3 Conclusion from electronic and thermal calculations . . . 74
4.4 Polarization dependent photothermal bending based on nanophotonic gratings . . . 75

5 Switchable optical materials for attitude control 80
5.1 Attitude control of a solar sail . . . 80
5.2 Overview of switchable optical materials . . . 81
5.2.1 Electrochromic materials . . . 81
5.2.2 Thermochromic phase change materials . . . 84
5.2.3 Switchable metamaterials . . . 88
5.2.4 Summary . . . 90

6 Polymer dispersed liquid crystals (PDLCs) 91
6.1 Background and motivation . . . 91
6.2 Device fabrication . . . 95
6.3 Device characterization . . . 95
6.4 Momentum calculation . . . 101

7 Conclusions and outlook 109
7.1 Radiation pressure measurements . . . 109
7.2 Polymer dispersed liquid crystals for solar sail attitude control . . . 111
7.3 Future work for PDLCs . . . 112
7.4 Potential experiments to solve the Abraham-Minkowski controversy . 114

A Modifications of the Cypher AFM 117
A.1 Free space optical path through the side window . . . 117
A.2 Free space coupling into the RainbowDrive . . . 117
A.3 Fiber coupling into the RainbowDrive . . . 120
A.4 Determining the spot size of a laser beam focused by an objective . . 122
A.5 Wavelength-dependent force measurement procedure . . . 124

B Additional information about the PDLC 126
B.1 Estimation of droplet size from SEM image . . . 126
B.2 PDLC device made with flexible substrate . . . 127

Bibliography 129

List of Tables

2.1 Fitted photothermal and radiation pressure amplitudes at zero frequency and the corresponding thermal time constants from Equation(2.3) for excitation near the base and near the free end of the cantilever. The error indicates the 95% confidence intervals of the fitting process. Note: The value of A_{rp} near the base is estimated from the measured value of A_{rp} near the free end, because the contribution of the radiation pressure to the total bending amplitude cannot be resolved by the fitting procedure when illumination is near the pivot point of the cantilever. 22

6.1 Comparison of figure of merits between our device and IKAROS. . . . 105

A.1 Percentage of optical power loss at each optical element in the fiber coupling optical path for a wavelength of 1060 nm. The total end-to-end coupling efficiency and the final beam wavefront quality are also listed in the table. 121

List of Figures

1.1 Schematic of the photon momentum transfer process for a perfect reflector and a perfect absorber. 3

2.1 Experimental setup for measuring the radiation pressure. An external laser (660 nm) is used to excite oscillation of the SiN_x cantilever, and a probe laser beam (860 nm) is used to detect the cantilever motion. . 19

2.2 Frequency response of the cantilever under external illumination near the base (a, b) and near the free end (c, d). When the excitation position x_0 is near base ($x_0 = 5$ μm) of the cantilever, the amplitude (a) and phase (b) of the response are dominated by the photothermal component (note: the radiation pressure component is too small to affect the total fit and is estimated from (c, d). For excitation near the free end ($x_0 = 185$ μm), the amplitude (c) and phase (d) of the response are dominated by the radiation pressure. (e) An SEM image of the cantilever and excitation positions (the x-axis is defined along the longitudinal direction of the cantilever, the y-axis is along the width, and the origin is at base of the cantilever). 21

2.3 Determination of force components (radiation pressure and effective photothermal) under sinusoidal illumination (9.32 mW at $\lambda = 660$ nm). The amplitude and phase of the experimental data are simultaneously fit to Equation (2.3) and applied to Equations (2.4)-(2.6) to determine the force magnitude (a) and phase (b). At low frequencies, the effective photothermal force is dominant, while at high frequencies the radiation pressure force is dominant. 24

2.4 Measured and calculated radiation pressure force are in agreement within the experimental and calculated errors. The measured force corresponds to the peak value of the sinusoidal response in the time domain resulting from sinusoidal external illumination. 25

2.5 Experimental setup for measuring radiation pressure under tunable-wavelength laser excitation. The thin film interference effect in the silicon cantilever causes the cantilever to experience wavelength-dependent radiation pressure and photothermal effects given the same incident optical power for different wavelengths. 28

2.6 (a) Measured and fitted amplitude of cantilever oscillation as a function of excitation frequency (tuning curve) at incident wavelength of 750 nm and laser power of 0.37 mW. (b) Optical properties of the cantilever at the excitation position near the free end of the cantilever. Black circles represent the measured transmission spectrum (2 nm step size). Black solid line represents the fitted transmission spectrum based on the thin film interference. Red and blue solid line represent the reflection and absorption spectrum calculated from the thickness and incident angle obtained from the transmission spectrum fitting. 31
2.7 (a) Measured and fitted amplitude of cantilever oscillation as a function of excitation frequency (tuning curve) at incident wavelength of 750 nm and laser power of 0.37 mW. (b) Measured and calculated radiation force normalized by the incident optical power F_0/P_0. The red curves represents the F_0/P_0 calculated by Equation (1) using the reflection and absorption spectrum shown in FIG.2. The shaded region shows the uncertainty in the calculated radiation force based on error propagation from the transmission fitting error. The black circle represents the measured F_{rp}/P_{in}, and the error bars are plotted every three data points for clarity. 33
2.8 Cantilever response for laser excitation (a) near the free end and (b) near the base of the cantilever. Left axis: Cantilever amplitude response (fitted zero-frequency amplitude A_0) normalized by the incident optical power. Right axis: (a) reflection spectrum and (b) absorption spectrum. (a) For excitation near the free end, the maxima in the amplitude response occur when the reflection is also a maximum, showing a radiation pressure dominated behavior. (b) Correlation between absorption maxima and cantilever response for excitation near the base shows behavior is dominated by photothermal effects. 34
2.9 Fitting of the experimental tuning curve using the Fano expression. Black dots are the measured data and the red line is the fit. 37
2.10 Nyquist plots showing the fitting of the complex cantilever oscillation amplitude using the Fano expression under different laser excitation positions on the cantilever (0 μm corresponds to the base and 180 μm corresponds to the free end). Black dots are the measured data and the red lines are the fit. 39
2.11 Magnitude of the fitted resonant amplitude in the Fano expression as a function of excitation position. 40

3.1 A cantilever with length L, width b, and thickness h, ... 41
3.2 A simple load: a point force is applied to the cantilever at position x_0. The positive direction of the bending moment is defined to be counterclockwise. 43

3.3 Force analysis of an infinitesimal cantilever section under a linear transverse force density $f(x,t)$ and a thermal moment $M_T(x,t)$. . . . 44
3.4 First three flexural vibration eigenmodes of the cantilever. 46

4.1 Infinitesimal length of the cantilever generates a bending moment due to the longitudinal thermal stress caused by a thermal expansion difference between two different materials. Dash-dot line is the neutral axis of the composite beam (where the stress is zero). $\sigma_{xxi}(i = 1, 2)$ is the normal stress of the cross section in x-axis for each material respectively. 54
4.2 Calculation of the temperature increase distribution along the x-axis for a 350 μm-long Al coated silicon cantilever when the intensity modulated laser is focused at the middle of the cantilever ($x_0 = 175$ μm). The modulation frequency is 10 kHz. 57
4.3 Calculation of the frequency response of the temperature increase at the illumination position. 59
4.4 Image of damages to a Si cantilever under extended high laser power illumination during an experiment. 60
4.5 Calculation of the first-eigenmode effective force of bimetallic effect (blue) and radiation pressure (red). 63
4.6 Magnitude of photogenerated carrier density along the thickness of a 1-μm-thick cantilever $\Delta n(x_0, z)$ at the center of laser spot ($x = x_0$). Two different combination of surface recombination rates are shown. s_1 is surface recombination rate at top surface ($z = 0$), and s_2 is surface recombination rate at bottom surface ($z = h$). Light intensity modulated at frequency of 10 kHz and The bulk recombination lifetime is set to 5×10^{-5} s 69
4.7 Effective force (a) magnitude and (b) phase of the fundamental mode due to electronic deformation. The incident power is 5 mW, laser sport radius 5 μm, absorption coefficient is 0.15, and excitation frequency 10 kHz, the top surface recombination rate 0.01 m/s, the bottom surface recombination rate 1 m/s and the bulk recombination lifetime 5×10^{-5} s. 71
4.8 Comparison of the effective force of the fundamental mode due to radiation pressure and electronic deformation at different excitation positions along the cantilever. 72
4.9 Magnitude of temperature increase distribution along the thickness of a 1-μm-thick cantilever $\Delta T(x_0, z)$ at the center of laser spot ($x = x_0$) at the center of laser excitation. Contributions from three heat sources are shown: (a) surface recombination, (b) body recombination, and (c) thermalization. (d) is the their sum. The incident power is 5 mW, laser sport radius 5 μm, absorption coefficient 0.15 and excitation frequency 10 kHz, the top surface recombination rate 0.01 m/s, the bottom surface recombination rate 1 m/s and the bulk recombination lifetime 5×10^{-5} s 73

4.10 Comparison of the effective force of the fundamental mode due to radiation pressure and thermal-elastic deformation at different excitation positions along the cantilever. 74
4.11 (a) Schematic illustration of fabricating grating structures near the base of the cantilever and the definition of TE and TM polarization. (b) Absorption difference (TE minus TM polarization) at 660 nm illumination given different combination of grating period and duty cycles. 77
4.12 SEM image of the grating structures fabricated by focused ion beam. The camera is tilted at an angle of 52°, the actual grating area is a 35 μm $\times$ 35 μm square. 78
4.13 Measured cantilever amplitudes (A_0) with changing laser polarization at two different excitation positions. Blue: laser is focused on the grating area. Red: laser is focused on planar Al coating area. 0° corresponds to the TM polarization and 90° corresponds to the TE polarization. 79

5.1 Coloration of the WO_3 thin film sputtered on glass slide using chemical H^+ injection. 82
5.2 Optical transmission spectrum of a WO_3 film before and after coloration. The coloration process reduces long wavelength transmission. 83
5.3 Schematic of the working principle of an electrochromic device. When a positive voltage is applied as shown in the figure, ions transport from the ion storage layer to the electrochromic material through the electrolyte, causing coloration. 84
5.4 (a) Fraction of photon momentum transfered to the 30 nm VO_2 thin film. (b) Fraction of photon momentum transfered to the 25 nm VO_2 thin film on top of 100 nm Al film. (c) AM0 solar irradiance spectrum. 87

6.1 Schematic showing propellantless altitude control of a solar sail using PDLC devices. The optical properties of PDLC devices are controlled individually, which results in spatial-variation of the radiation pressure across the solar sail. 94
6.2 a) The direct transmission as a function of input wavelength and RMS (root mean square) voltage applied to the PDLC cell. b) The direct transmission as a function of RMS voltage at 650 nm, corresponding to the black line in a). The turn-on voltage V_{90} at this wavelength, where the transmission reaches 90% of the maximum transmission, is 70 V, and the corresponding turn-on field is 2.12 V/m. Insets: photos of the PDLC cell in the (i) off state and (ii) on state. c) The direct transmission across the visible on state (100 V) and off state (0 V), corresponding to the blue and red lines in a), respectively. 97

6.3 a) Experimental setup for measuring the angular distribution of light scattering for the PDLC cell. Input light is at normal incidence. b) A series of angular distribution measurements using 632.8 nm illumination with increasing voltages applied to the PDLC cell. Each curve shows the optical power measured at different scattering angles normalized to the incident laser power and is mirrored with respect to zero degrees (incident direction). Scattering distribution of the PDLC is shown in the off state under c) visible and d) infrared illumination. 98
6.4 Total transmission, absorption, and reflection of the PDLC cell in the on and off states under near normal incidence measured with an integrating sphere. 100
6.5 Fraction of momentum per photon transferred to the PDLC (left axis) in the on and off states at different wavelengths (400-1100 nm) overlaid with the AM0 solar irradiance spectrum (right axis). The measured data covers 77.1% of the total energy (or momentum) of the AM0 solar spectrum. 102
6.6 a) Optical images of (1 in x 1 in) devices in the off state (1st row) and the on state (2nd row) of five PDLC cells with increasing thickness from left to right. Cell thickness is measured by optical interferometry. b) Average fraction of momentum transferred to the PDLCs weighed by the AM0 solar spectrum over the measurement range (400 nm to 1100 nm) for the five devices. c) Turn-on voltages (left), determined by 90% transmission at 650 nm incident illumination, and power consumption per unit area (right) in the on state as a function of PDLC thickness. The black and red lines are linear fits to the turn-on voltage and power consumption data, respectively. Inset: direct transmission under 650 nm illumination versus applied RMS voltage. 107

7.1 Images of flexible PDLC devices made on ITO coated PET material with a thickness of 200 μm. 113
7.2 Schematics of the momenta of reflected, absorbed and transmitted photons at each stage when interacting with a medium with refractive index n which is free to move (*e.g.* a cantilever). The gray slab represents the cantilever. p_i is the initial photon momentum in air, p_n is the photon momentum in the medium and p_f is the final momentum of that photon. 115
7.3 Proposed cantilever schematic for measuring the photon momentum inside the cantilever. 116

A.1 (a) External laser coupled into the atomic force microscope through a customized transparent window on the side of the Cypher. (b) Optics inside the Cypher chamber (the area in the white circle in (a)). A 45° diachronic hot mirror is placed above the objective using a custom designed holder to reflect the external laser beam down while letting pass the light for imaging. (c) Image of the cantilever with the focused external laser beam. The actual spot size of the focused light is much smaller than it seems in the photo because many pixels in the photodetector are saturated, appearing white thus making the spot bigger. 118
A.2 (a) External laser coupled into the atomic force microscope through the RainbowDrive from the front of the Cypher. (b) Image of the cantilever with the focused external infrared laser beam. 119
A.3 Design schematic of the fiber optic coupling system that launches the laser beam into the RainbowDrive. 120
A.4 Actual images of the fiber coupling setup. 121

B.1 (a) An SEM image of the surface of the PDLC film. (b) Circle detection within ImageJ to determine the droplet size. 127
B.2 PDLC device made with ITO-coated PET substrate (200 μm thick) shows good optical switchability even when it is bent significantly. . . 128

List of Publications

Dakang Ma and Jeremy N. Munday, Demonstration of wavelength-dependent radiation pressure in silicon microcantilever due to thin film interference (manuscript in preparation)

Dakang Ma, Joseph Murray and Jeremy N. Munday, Controllable propulsion by lightsteering a solar sail via tunable radiation pressure. *Advanced Optical Materials* (2017) (DOI:10.1002/adom.201600668).

Joseph Murray, **Dakang Ma** and Jeremy N. Munday, Electrically Controllable Light Trapping for Self-Powered Switchable Solar Windows. *ACS Photonics* (2016).

Qing Zhang, Wenzhong Bao, Amy Gong, Tao Gong, **Dakang Ma**, Jiayu Wan, Jiaqi Dai, Jeremy N. Munday, Jr-Hau He, Liangbing Hu and Daihua Zhang, A highly sensitive, highly transparent, gel-gated MoS2 phototransistor on biodegrad- able nanopaper. *Nanoscale* 8, 14237-14242 (2016).

Dakang Ma, Joseph L. Garrett, and Jeremy N. Munday, Radiation Pressure Measurement under Ambient Conditions Using a Microcantilever. *Frontiers in Optics 2015, OSA Technical Digest (online) (Optical Society of America, 2015)*, paper FTh1A.7 (2015).

Dakang Ma, Joseph L. Garrett, and Jeremy N. Munday, Quantitative measurement of radiation pressure on a microcantilever in ambient environment. *Appl. Phys. Lett.* 91107, 4 (2015)

Wenzhong Bao, Jiayu Wan, Xiaogang Han, Xinghan Cai, Hongli Zhu, Dohun Kim, **Dakang Ma**, Yunlu Xu, Jeremy N Munday, H Dennis Drew, Michael S Fuhrer and Liangbing Hu, Approaching the limits of transparency and conductivity in graphitic materials through lithium intercalation. *Nature communications*, **5** (2014).

Chapter 1: Introduction

1.1 A brief history of radiation pressure

Light carries momentum, which can be transferred to an object upon reflection or absorption. The resulting force per unit area from light, so called radiation pressure, is rather weak but can have macroscopic consequences. For example, sunlight imparts momentum on dust particles causing a comets tail to be directed away from the sun, as first suggested by German astronomer Johannes Kepler in 1619 [1, 2]. James Clerk Maxwell first deduced and predicted that light carries momentum based on his wave theory of electromagnetism [3].

In the same year, chemist Sir William Crookes invented the famous "Crookes radiometer", also known as "light mill" [4]. It consist of a glass bulb with partial vacuum, inside which is a set of vanes able to spin around a spindle. One side of each vane is black and the other side is silver. The vanes rotate upon illumination and rotate faster as light intensity increases. Crookes suggested that this was the evidence of radiation pressure and was first supported by Maxwell who thought the radiometer as a confirmation of his theory. However, it turned out that it was the black sides of the vanes, not the silver sides that got pushed away from the light source, exactly opposite to what could have been caused by radiation pressure.

Because the silver side is close to a perfect reflector and the black side is close to a perfect absorber, momentum transfer on the silver side should be larger than that on the black side, pushing the silver side away from light if it was caused by radiation pressure. It seemed reasonable, in this case, to suspect that the darker side heated up, causing a higher pressure, which rotated the vanes. However, this idea was soon rejected by Maxwell based on his analysis that proved equal pressures on both sides of the vane [4]. The final piece of puzzle was provided qualitatively by Osborne Reynolds in 1879 by his theory of "thermal transpiration" [5]. According to Reynolds, the net force is generated on the edges of the vanes, not the surface, when hotter molecules from the black side strike the edges obliquely and impart a higher force than the colder molecules on the silver side [6]. Maxwell was the referee for Reynolds unpublished paper and soon adopted the idea and made his own mathematical derivation, and his paper was published shortly before his death [7].

A precise measurement of radiation pressure was conducted independently by Lebedev in 1901 [8] and Nichols and Hull in 1903 [9]. Nichols and Hull conducted the experiment using a radiometer with small silvered glass mirrors suspended in the manner of a torsion balance and were able to obtain an agreement between observed and computed radiation pressures within about 0.6% [10].

With the development of quantum mechanics, the momentum of light could be described more simply through the notion of photons, exploiting the particle aspect of wave-particle duality of light. The momentum of a photon in vacuum is given by

the De Broglie's relationship:

$$p = \frac{h}{\lambda} = \frac{\hbar\omega}{c}, \tag{1.1}$$

where h is the Plank constant and λ is the vacuum wavelength of light. Momentum transfer takes place when light is either reflected or absorbed by an object. Twice the original photon momentum is transferred to the object if it is a perfect reflector ($p = 2h/\lambda$) and if the object is a perfect absorber, its final momentums is equal to that of the original photon ($p = h/\lambda$) (Figure 1.1).

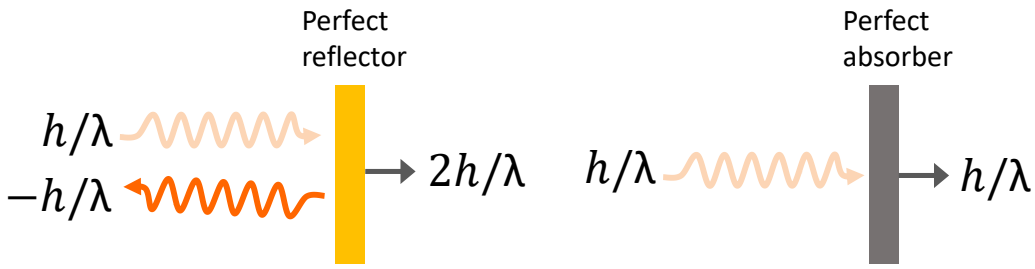

Figure 1.1: Schematic of the photon momentum transfer process for a perfect reflector and a perfect absorber.

For a laser beam with power P normally incident on a flat surface with reflectivity R and absorptivity A, the number of photons per unit time hitting the surface is:

$$\frac{dN}{dt} = \frac{P}{hc/\lambda}. \tag{1.2}$$

Thus the radiation pressure exerted on the surface is:

$$F_{rp} = (2R + A)p\frac{dN}{dt} = \frac{(2R + A)P}{c}. \tag{1.3}$$

1.2 The Abraham-Minkowski controversy

Since the early 1900s, two proposals for the momentum of light in dielectric media have led to a century-long controversy [1]. In 1908, Minkowski proposed a formalism for the electromagnetic momentum density in a medium that is equivalent to a photon momentum of:

$$p_M = \frac{n\hbar\omega}{c} = np_{vac}, \tag{1.4}$$

where n is the phase refractive index in the medium, $\hbar\omega$ is the photon energy and p_{vac} is the photon momentum in vacuum. A year later, Abraham proposed another formalism that resulted in a photon momentum of:

$$p_A = \frac{\hbar\omega}{nc} = \frac{p_{vac}}{n}, \tag{1.5}$$

i.e. the photon momentum is decreased by a factor of $\frac{1}{n}$. A simple explanation of Minkowski's argument roots from wave-particle duality. Inside a medium with dielectric index of n, the wavelength of light is decreased to $\lambda = \lambda_0/n$. Using the De Broglie relation, the particle's momentum is $p_M = h/\lambda = nh/\lambda = n\hbar\omega/c = np_{vac}$. Abraham's argument, on the other hand, can be framed in Einstein's relativity theory. The energy-mass equivalence formula $E = mc^2$ implies an effective photon mass $m = E/c^2$. Because the photon's velocity is reduced upon entering a medium by a factor of $1/n$, the momentum is subsequently reduced: $p_A = mv = (E/c^2)(c/n) = \hbar\omega/nc = p_{vac}/n$. Thus far, various experiments have claimed to support both Minkowski's description and Abraham's description [11–16], leading to a

number of theoretical attempts at a resolution and controversies [17,18]. Meanwhile, many physicists believe that the Abraham-Minkowski debate is about how an electromechanical system can be partitioned into "electromagnetic" and "mechanical" subsystems, *i.e.* field momentum and material momentum [19–21].

1.2.1 The classical electromagnetic picture

Although quantum theory conveniently produces momenta carried by single photons, radiation pressure is a classical effect and the controversy started when quantum theory had not been fully developed. So it is more insightful to look classically at the origins of the controversy. Just like the energy continuity equation that relates the energy density and energy flux density (Poynting vector), momentum density and momentum flux density also follow the conservation equation (in vacuum) [22]:

$$\frac{d}{dt}(\vec{P}_{mech} + \vec{P}_{field})_i = \sum_j \int_V \frac{\partial}{\partial x_j} T_{ij} d^3x, \tag{1.6}$$

where the subscripts i, j represent the coordinate components, T_{ij} is the Maxwell stress tensor, which represents the momentum flux density, $\vec{P}_{mech}$ is the total momenta of all the charges and currents within the integration volume, and $\vec{P}_{field}$ is the momentum of the electromagnetic wave in vacuum:

$$\vec{P}_{field} = \epsilon_0 \int_V \vec{E} \times \vec{B} d^3x, \tag{1.7}$$

which means the electromagnetic momentum density in vacuum is:

$$\vec{g}_{vac} = \epsilon_0 \vec{E} \times \vec{B}. \tag{1.8}$$

The force acting on the charges and currents within the integration volume can be calculated directly through the Lorentz force:

$$\vec{F} = \frac{\vec{P}_{mech}}{dt} = \int_V (\rho \vec{E} + \vec{J} \times \vec{B}) d^3x. \tag{1.9}$$

Alternatively, the force can also be calculated from Equation 1.6, which leads to a force density:

$$(\vec{f}_{vac})_i = \sum_{j=1}^{3} \frac{\partial T_{ij}}{\partial x_j} - (\frac{\partial \vec{g}_{vac}}{\partial t})_i, \tag{1.10}$$

In a dielectric medium, Equation 1.6 still holds with a stress tensor different from that in vacuum [20]:

$$T_{ij}^m = \frac{1}{2}\delta_{ij}\vec{E} \cdot \vec{D} - E_i D_j + \frac{1}{2}\delta_{ij}\vec{B} \cdot \vec{H} - B_i H_j. \tag{1.11}$$

However, the partition between the field momentum and mechanical momentum is more complicated. Minkowski defined the field momentum density as:

$$\vec{g}_M = \vec{D} \times \vec{B}, \tag{1.12}$$

while Abraham defined the field momentum as:

$$\vec{g}_A = \frac{1}{c^2}\vec{E} \times \vec{H}. \tag{1.13}$$

Analogous to Equation 1.10, the force density acting on the medium, assuming that the field has the Minkowski momentum density form, is given by [20]:

$$(\vec{f}_M)_i = \sum_{j=1}^{3} \frac{\partial T_{ij}^m}{\partial x_j} - (\frac{\partial \vec{g}_M}{\partial t})_i, \tag{1.14}$$

while the force density acting on the medium, assuming that the field has the Abraham momentum density form, is given by:

$$(\vec{f}_A)_i = \sum_{j=1}^{3} \frac{\partial T_{ij}^m}{\partial x_j} - (\frac{\partial \vec{g}_A}{\partial t})_i. \tag{1.15}$$

This indicates that the force acting on the medium is different for the two forms of the momentum density definition. The difference $\vec{f^A}$ is called the Abraham force density, given by [21]:

$$\vec{f^A} = \vec{f_A} - \vec{f_M} = \frac{\partial \vec{g}_M}{\partial t} - \frac{\partial \vec{g}_A}{\partial t} = \frac{1}{c^2}(n^2 - 1)\frac{\partial}{\partial t}(\vec{E} \times \vec{H}). \tag{1.16}$$

$\vec{f}_M$ is called the Lorentz force density and for an isotropic medium that is free of free electrons (ρ) and current sources ($\vec{J}$), it reduces to [21]:

$$\vec{f}_M = -\frac{1}{2}\epsilon_0 E^2 \nabla n^2, \tag{1.17}$$

which is also the total force density given by Minkowski. Alternatively, the total force density given by Abraham is:

$$\vec{f_A} = -\frac{1}{2}\epsilon_0 E^2 \nabla n^2 + \vec{f}^A. \tag{1.18}$$

While there are many theoretical works discussing these differences [14,17–21], there have been only limited experimental demonstrations [12, 13, 15, 16]. Perhaps more interestingly, there is evidence in support of both momentum forms as described in the following subsections.

1.2.2 Experiments supporting Minkowski's description

The first experiment that supports Minkowski momentum was conducted by Jones and Richard in 1954 [11]. They measured the recoil of a metal vane mounted on a torsional suspension upon illumination when the vane is immersed in liquids and in air. The deflection of the vane was detected by an optical level. They found that the ratio of deflection in liquids to that in air is equal to the refractive index of the liquid for six of the liquids. The precision of the measurement was further improved by Jones and Leslie in 1978 [12].

In 1980, Gibson *et al.* studied the radiation pressure in dense medium through the photon drag effect in silicon and germanium [23]. The photon drag effect happens when the light momentum absorbed in semiconductor materials are transfered to electrons in conduction or valence bands. When the semiconductor material is long in the incident light direction, in the open-circuit condition, a noticeable potential

difference will exist across the two ends. At sufficiently long wavelengths the effect is independent of the semiconductor band structure and depends on the radiation pressure in the dielectric. In their experiment, Gibson *et al.* used radiation with wavelengths varying from far infrared (28 μm) to millimerter wave (1.2 mm) and the photon drag effects agree with the Minkowski momentum prediction in the long wavelength limit.

In 2005, Campbell *et al.* measured the photon recoil momentum in a Bose-Einstein condensate (BEC), a diluted medium cooled to nearly absolute zero temperature [13]. They illuminated the atoms with two beams of light travelling in opposite directions, forming a standing wave. When the atoms absorb the photons, the momentum transfer could be inferred from the interference fringes of the atom waves. The recoil momentum for absorbing the photon indicated agreement with Minkowski's description of the momentum.

1.2.3 Experiments supporting Abraham momentum

Experiments supporting the Abraham momentum are even rarer and more controversial. The first compelling case is the Balazs "thought experiment" back in 1953 [14]. The concept consists of a transparent slab that is initially at rest and has perfect antireflection coatings at the entrance and exit facets. When a plane-wave light pulse enters the slab, its velocity reduces to c/n, which must be compensated by a movement of the slab in the same direction with the light propagation, leaving the Abraham momentum the only plausible form to satisfy the momentum conservation

and center-of-mass theorems at the same time [20, 24].

The smoking gun to the A-M controversy lies in the existence of the time-varying Abraham force. The only experiment that successfully measured this to my knowledge was conducted by Walker *et al.* in 1975 with a quasi-static electromagnetic field of 0.3 Hz [15]. The experiment was performed by suspending a disk of high dielectric constant material, barium titanate, creating a torsional pendulum. A fixed magnetic field was maintained parallel to the normal axis of the disk (vertical), and a time-varying radial electric field was applied between the center and outer shell of disk. This generated an Abraham force that provided a torque that rotated the disk. Although this experiment was conducted at a low frequency rather than at optical frequencies using a similar fashion, it shows a very nice example of the existence of Abraham force based Abraham's description of the light momentum, which is perhaps more convincing than the previously mentioned experiments that supported Minkowski's description.

Modern experiments that claim to have observed the Abraham momentum are more controversial. She *et al.* observed the recoil pattern of a nano fiber filament when light exited and concluded that it could only be caused if light follows the Abraham momentum inside the fiber [16]. The experimental result seems simple and straight forward. The upward recoil seen in the experiment indeed could not be explained by just the Lorentz force because of the sign of the Lorentz force is opposite to what is observed in the experiment. Abraham force does not average out to zero because of the pulsed laser used in the experiment and it would be an upward force when the pulse is leaving the fiber. However, the paper lacks essential

quantitative analysis to back up the results. The recoil of the fiber end could be caused by many other factors that have nothing to do with the photon momentum, as suggested by Brevik [25] and Mansuripur [18].

1.2.4 Other experiments and conclusion

More recently, there were a couple of experiments that revisited the original experiment of Ashkin and Dziedzic [26], with modified setups and more detailed analysis [27, 28]. These experiments tried to measure the deformation of a liquid surface when light shines from air into liquid. The results are mixed; both the bulging and indenting of the liquid surfaces were observed. Interpretation of these experiments is complicated because not only the momentum transfer is dependent upon n, but also is the power transfer. It also involves complicated fluid dynamics and thermal effects. Zhang *et al.* claimed that the Abraham momentum emerges when the fluid is moving and the Minkowski momentum when the light is too focused or the container too small to set the fluid into motion [28]. However, indenting of the liquid surface could be caused just by the radiation pressure due to reflection at the interface, so it is not a definitive evidence of the Abraham momentum.

It is worth mentioning that several experiments have been proposed to measure the Abraham force at optical frequencies. The key principle behind these proposals is to make the light pulse stay inside the medium as long as possible. Brevik *et al.* proposed that by wrapping a long optical fiber around a cylindrical light-weight torsion pendulum and launching a train of optical pulses into the long fiber, one should

be able to detect a significant angular displacement along the light propagation direction caused by the Abraham force. Or if the Abraham force does not exist, one would observe the rotation in the opposite direction [29]. Labardi *et al.* suggested measuring the Abraham force utilizing the atomic force microscopy cantilever. The force is in the magnitude of $P_0\omega_0\tau/c$, where P_0 is the laser power amplitude, ω_0 is the power modulation frequency, and τ is the transit time for light to travel through the slab. This quantity is usually too small to measure, but if the speed of light can slow down in the material, like in the frequency range within a material with strong polaritonic effects, the force could be measurable [30].

The controversy surrounding the correct form of the momentum of light in a medium has run for a century and will likely continue to inspire researchers to develop new experimental and theoretical methodologies to tackle this problem. Stronger theoretical arguments such as the symmetry of the energy-momentum tensor and compatibility with the relativity theory favor Abraham's momentum as the real kinetic momentum of the electromagnetic field in a medium. Minkowski's momentum, on the other hand is considered the canonical momentum [19], which is the amount of momentum the field imparts to atoms or objects within a dielectric medium. Consensus seems to have been reached between scientists, while lacking support from convincing experiments.

Future experimental design should focus on measuring the Abraham force in the optical frequencies. Reducing the radiation pressure at the medium interface will help to separate out the Abraham force. Moreover, other side effects beside momentum transfer should be carefully considered quantitatively before drawing a

conclusion.

1.3 Radiation pressure in space: solar sails

The concept of radiation pressure for space propulsion has a long history in both popular culture and as a next generation space technology [31, 32]. Most space missions are limited by the amount of chemical propellant carried on board; however, as an alternative, solar sails use solar radiation pressure as propulsion and offer an opportunity for propellant-free space travel, enabling long-term and long-distance missions that are impossible with traditional methods. Unlike the strong but temporal acceleration provided by chemical rockets, the acceleration from solar radiation pressure is small but continuous and can ultimately reach a much higher speed [33]. Further, depending on how the sail is angled with respect to the sun, solar radiation pressure can either increase or decrease its orbital velocity. Therefore, solar sails are believed to be the only reasonable means of propulsion for deep space interstellar travel. A solar sail is usually made of a large area light-weight substrate with a highly reflective coating. The total solar radiant flux I_0 at one astronomical unit (AU) is 1361 W/m^2, the maximum radiation pressure P_m (normal incidence on a perfectly reflecting planar surface) is: $P_m = 2I_0/c = 9.08\ \mu$N/m^2 where c is the speed of light.

Serious attempts have been made to turn solar sail propelling from science fiction to reality in the past decade. In June 2005, Cosmos 1, a project led by The Planetary Society, was the first attempt to send a solar sail into orbit. However the

submarine launched rocket failed to deliver the spacecraft into the orbit [34].

2010 became a milestone year in solar sail history. In May, JAXA (The Japan Aerospace Exploration Agency) successfully launched IKAROS (Interplanetary Kite-craft Accelerated by Radiation of the Sun), the first-ever spacecraft to use a solar sail for propulsion in space. Not only did IKAROS successfully deploy its 170 m^2 solar sail, it also achieved attitude control using reflection control devices (RCD) attached on the sail [35]. A few month later, NASA's NanoSail-D2 cubesat solar sail spacecraft was successfully deployed in a low earth orbit. The sail is made of an aluminum coated polymer, called CP-1, with a thickness of 7.5 μm and a surface area of about 10 m^2 [36].

After the success of the NanoSail project, NASA partnered with L'Garde and to launch the Sunjammer project, which aimed at using solar sail technology to propel the spacecraft to the Earth-Sun L1 Lagrangian point. From there, it would be used to provide early detection and warning of the geomagnetic storms on the Sun that can damage power and communication systems on earth and orbiting spacecrafts. Although the mission was unfortunately canceled in October 2014, L'Garde demonstrated the ability to make a 38 m $\times$ 38 m solar sail, a surface area of 1444 m^2. It was the largest solar sail made and tested in a vacuum chamber on ground [37].

The Planetary Society followed the path of the Nanosail-D project in developing a smaller solar sail with cubesats as payload and started the LightSail project. As a test flight, LightSail 1 (formerly LightSail-A), was launched on May 20th, 2015 from Cape Canaveral Air Force Station, Florida to a low orbit. The solar sail was

successfully deployed on June 7th, 2015. The orbit is so low that atmospheric drag brought LightSail 1 down seven days after sail deployment [38]. The solar sail measures 5.6 m $\times$ 5.6 m, for a total surface area of 32 m^2 of 4.5 μm thick aluminized mylar film, which is the thinnest sail to be deployed in space [39]. Its successor, LightSail 2 is scheduled to launch in March 2017 to a much higher orbit altitude of 500 miles (800 km). NASA also has a project called, Near-Earth Asteroid Scout, which uses a solar sail to carry cubesats to collect data and is planned to launch in 2018 [40].

1.4 Radiation pressure in nanoscale devices

Thanks to the advancement of microelectronicmechanical systems (MEMS) fabrication technology, micro/nano-mechanical transducers have become sensitive enough that radiation pressure can influence them greatly. Radiation pressure is of interest to many research areas at micro/nano scales, including active cooling of mechanical resonators in cavity optomechanics [41–44], cantilever spring constant calibration [45], enhanced radiation force in a microwave resonant unit [46], etc. Thus, there is a need to better understand, measure and control radiation pressure in both micro and macro systems.

1.5 Outline of Thesis

The thesis consists of two major parts. The first part consists of two radiation pressure experiments and related findings about photothermal effects (Chapter 2-4).

Chapter 2 first discusses a quantitative measurement of the radiation pressure using a microcantilever in an ambient environment under a single wavelength illumination, followed by another experiment showing the wavelength-dependent radiation pressure due to thin-film interference in a cantilever. Chapter 3 discusses cantilever beam theory and how to turn a distributed force or moment into mode-dependent effective forces so that their effects can be compared directly. Chapter 4 discusses different mechanisms of photothermal bending and calculations of their magnitudes. The second part of the thesis concentrates on switchable optical material and devices in potential solar sail application (Chapter 5-6). Chapter 5 gives an overview of current switchable optical materials and Chapter 6 focuses on our efforts in making and characterizing polymer dispersed liquid crystal devices for the purpose of switchable momentum transfer.

Chapter 2 is based on material published in D. Ma *et al.* "Quantitative measurement of radiation pressure on a microcantilever in ambient environment", *Appl. Phys. Lett.* 91107, 4 (2015) and D. Ma *et al.* "Demonstration of wavelength-dependent radiation pressure in silicon microcantilever due to thin film interference", (manuscript in preparation). Chapter 6 is based on material published in D. Ma *et al.* "Controllable propulsion by lightsteering a solar sail via tunable radiation pressure", *Advanced Optical Materials* (2017) (DOI:10.1002/adom.201600668).

Chapter 2: Radiation pressure measurement

2.1 Quantitative radiation pressure measurement in ambient environment

2.1.1 Background and motivation

Micromechanical systems such as microcantilevers and atomic force microscope (AFM) detection scheme are an ideal platform for the study of radiation pressure due to their high sensitivity and commercial availability. In order to explore the radiation pressure in more exotic material systems, it is important to be able to first quantitatively measure radiation pressure on microresonators made of simple, uniform materials, such as dielectrics (*e.g.* Si_3N_4) and semiconductors (*e.g.* Si). However, this is not an easy task because quantitative measurements of radiation pressure in micromechanical systems are often obscured by photothermal effects [42, 47–49]. Compared with macroscopic resonators, microscopic mechanical resonators have much shorter thermal time constants, ranging from tens of milliseconds to tens of nanoseconds [41, 42, 48]. In order to mitigate photothermal effects, previous experiments required complex resonator designs consisting of highly-reflective multilayer stacks deposited onto large customized cantilevers [45],

micro-scale transfer of a mirror onto a microcantilever [41], and attachment of a gold mass to a cantilever to increase the thermal time constant [50]. Earlier experiments used a two-laser actuation technique and showed the dominance of radiation pressure on uncoated cantilevers [51,52], but they lacked accurate quantitative agreement with theory. Further, most measurements are performed in vacuum to avoid radiometric effects [53], which limit their applicability in micro-scale technologies that operate under ambient conditions. In this chapter, we show an accurate measurement of radiation pressure in an ambient environment on an uncoated silicon nitride microcantilever. We estimate the photothermal contribution to the total measured force, identify the bending direction of the cantilever, and compare experimental results with theoretical calculations, finding agreement within the calculated errors.

2.1.2 Experimental approach

The apparatus used for measuring the radiation pressure consists of a modified atomic force microscope (AFM), shown in Figure 2.1. We modified the system (Asylum Research, Cypher) by introducing a second laser source ($\lambda = 660$ nm) into the optical path and by focusing the light on the backside of the cantilever through the same objective ($20\times$) as the probe laser. The focused spot size is estimated to be about 6 μm from the full-width-at-half-max of the beams Gaussian profile. This laser is driven by a sinusoidal reference signal from a lock-in amplifier and is used to excite the cantilever. The cantilever deflection is detected by a split-quadrant photodetector using the optical lever method, and the amplitude and phase of the

signal are determined by the lock-in amplifier. An uncoated rectangular silicon nitride (SiN_x) cantilever (Bruker, MLCT-O10, uncoated) is used in the experiment to reduce photothermal effects caused by photon absorption. It lacks absorption throughout the visible spectrum, and is free from bimorphic bending effects found with coated cantilevers.

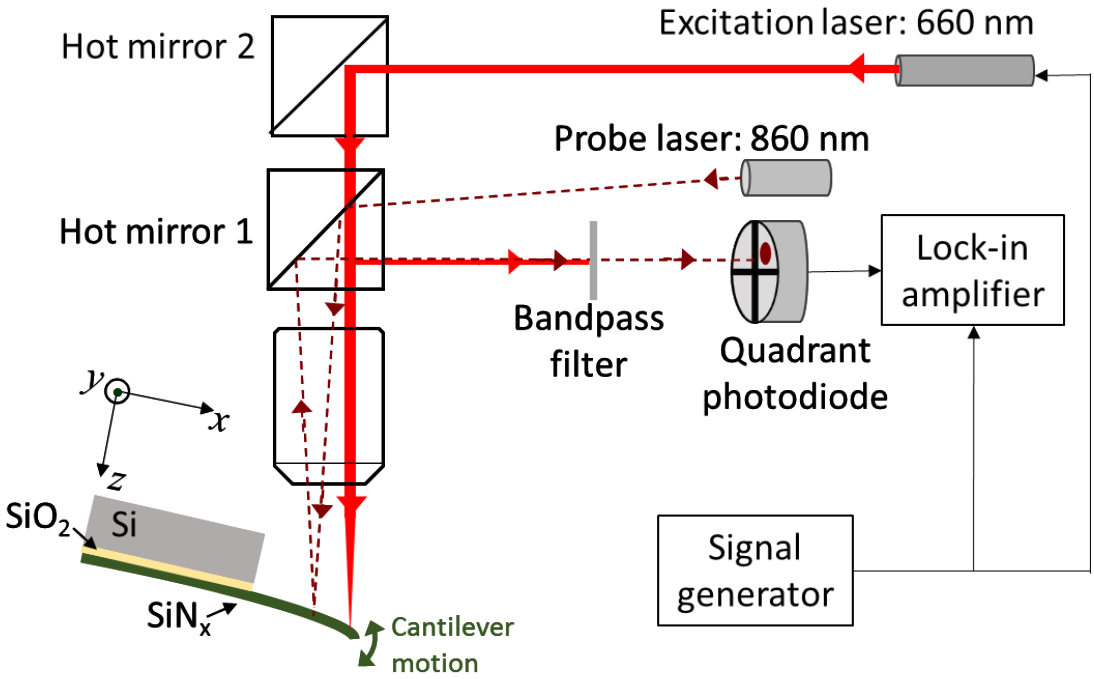

Figure 2.1: Experimental setup for measuring the radiation pressure. An external laser (660 nm) is used to excite oscillation of the SiN_x cantilever, and a probe laser beam (860 nm) is used to detect the cantilever motion.

2.1.3 Results and analysis

The radiation pressure induced bending can be distinguished from photothermal bending by its frequency response and bending direction. While radiation pressure is independent of modulation frequency, photothermal bending is not, due to

its finite thermal relaxation time. The total effective photothermal force has a low pass frequency response of the form [41]:

$$F_0^{pt}(\omega) = F_0^{pt}(0) / (1 + i\omega\tau), \tag{2.1}$$

where ω is the laser driving frequency, and τ is the photothermal characteristic time constant. While the origin of the photothermal response is difficult to determine in materials with little absorption (*e.g.* SiN_x), the photothermal bending in our experiment is likely due to the difference in thermal expansion coefficients between the cantilever and the substrate chip, which is most pronounced when illumination occurs near the base of the cantilever. Although the suspended cantilever is made of silicon nitride only, the base of the cantilever sits atop a silicon oxide layer on a silicon chip (Figure 2.1). In this geometry, the cantilever bends towards the silicon substrate when heated [54], which corresponds to an upward bending in our setup, opposite to that of the radiation pressure.

To determine the forces exerted on the cantilever, we measure the magnitude and phase of the cantilever oscillation under sinusoidal external laser excitation whose modulation frequency is swept across the fundamental resonance frequency of the cantilever. Under this sinusoidal excitation, the force on cantilever has the harmonic form:

$$F(t) = Re\left[F_0(\omega)\, e^{i\omega t}\right]. \tag{2.2}$$

The measured amplitude and phase are then combined to form a complex

amplitude phasor, which is fit to a modified damped harmonic oscillator model incorporating the contribution from the radiation pressure and photothermal effects, given by:

$$A(\omega) = \frac{A_{rp} + A_{pt}(0)/(1 + i\omega\tau)}{1 - (\omega/\omega_1)^2 + i(\omega/\omega_1 Q)}, \tag{2.3}$$

where ω_1 is cantilevers fundamental resonance frequency, and A_{rp} and $A_{pt}(0)$ are the amplitudes of the cantilever displacement at the free end due to the radiation force and the effective photothermal force (i.e. the effective bending force resulting from photothermal bending) at zero-frequency, respectively. Positive values of A_{rp} and $A_{pt}(0)$ indicate a downward bending, while negative values indicate an upward bending according to our coordinate (Figure 2.1).

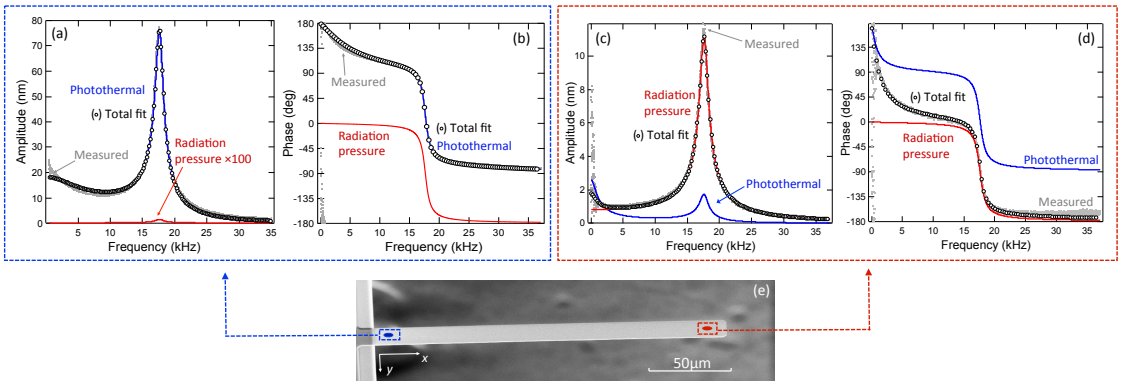

Figure 2.2: Frequency response of the cantilever under external illumination near the base (a, b) and near the free end (c, d). When the excitation position x_0 is near base ($x_0 = 5$ μm) of the cantilever, the amplitude (a) and phase (b) of the response are dominated by the photothermal component (note: the radiation pressure component is too small to affect the total fit and is estimated from (c, d). For excitation near the free end ($x_0 = 185$ μm), the amplitude (c) and phase (d) of the response are dominated by the radiation pressure. (e) An SEM image of the cantilever and excitation positions (the x-axis is defined along the longitudinal direction of the cantilever, the y-axis is along the width, and the origin is at base of the cantilever).

The dominant driving mechanism (radiation pressure or photothermal) de-

pends on the position of cantilever excitation. By controlling the laser excitation position along the longitudinal direction of the cantilever, we determine the frequency response of the cantilever at each position (Figure 2.2). The data are fit to Equation (2.3) to determine the parameters describing the cantilevers response.

	A_{rp} (nm)	$A_{pt}(0)$ (nm)	τ (μs)	f_0 (Hz)	Q
Near free end	-0.813±0.002	2.53±0.05	186±4	17632±1	13.59±0.04
Near base	-1e-4	18.7±0.1	31.1±0.3	17663±3	14.78±0.07

Table 2.1: Fitted photothermal and radiation pressure amplitudes at zero frequency and the corresponding thermal time constants from Equation(2.3) for excitation near the base and near the free end of the cantilever. The error indicates the 95% confidence intervals of the fitting process. Note: The value of A_{rp} near the base is estimated from the measured value of A_{rp} near the free end, because the contribution of the radiation pressure to the total bending amplitude cannot be resolved by the fitting procedure when illumination is near the pivot point of the cantilever.

When excited near the base, the cantilever displays a large vibration amplitude, which increases at low frequencies driven by the photothermal effects. For excitation near the free end of the cantilever, radiation pressure dominates at excitation frequencies above a few kHz. This is because that radiation pressure generates a larger total bending moment when its farther away from the pivot point. On the other hand, photothermal effects are more effective when heating is closer to the pivot point [55].

The phase signal in our experiments can also indicate different driving mechanisms. The radiation pressure causes a downward deflection of the cantilever (positive) when illuminated from above, in phase with the excitation signal at dc and lags 90° at resonance (resulting in a phase of -90°). On the other hand, the effective photothermal force causes an upward bending (negative), so the phase signal is 180°

at dc and lags more than 90° and at most 180° at resonance, depending on the thermal constant of the low-pass behavior (resulting in 0° to 90°). In our measurement, when exciting near the free end, the phase at resonance is approximately -80°, indicating that radiation pressure is dominant but when exciting near the base, the phase at resonance is approximately 20°, indicating that photothermal bending is dominant.

In order to measure the radiation pressure, we focus our attention on the situation where the laser excitation is near the free end ($x_0 = 185$ μm, where x0 is the distance from the base). The total measured force is given by:

$$F_{0,measure}(\omega) = A(\omega)\left[1 - (\omega/\omega_1)^2 + i(\omega/\omega_1 Q)\right] k_1 \frac{1}{\gamma}, \tag{2.4}$$

where k_1 is the spring constant of the fundamental mode determined by the Sader method [56, 57], and γ is the distributed force correction factor that takes into account the fact that the forces are not point forces exerted at the end of the cantilever $x = L$(see below). The fitted radiation force and effective photothermal force can be determined, respectfully, from Equations (2.3) and (2.4) as:

$$F^{rp}_{0,fit} = A_{rp} k_1 \frac{1}{\gamma}, \tag{2.5}$$

and

$$F^{pt}_{0,fit}(\omega) = \frac{A_{pt}(0)}{(1 + i\omega\tau)} k_1 \frac{1}{\gamma}. \tag{2.6}$$

The distributed force correction factor γ is calculated as the ratio of the cantilever

oscillation amplitude generated by a Gaussian distributed pressure at $x = x_0$ with total force F_0 to that generated by a point force F_0 at $x = L$:

$$\gamma = \frac{\int_0^L f_{Gauss}(x)\,\varphi_1(x)\,dx}{\int_0^L F_0\delta(x-L)\,\varphi_1(x)\,dx} = B\frac{\int_0^L e^{-2(x-x_0)^2/w_0^2}\varphi_1(x)\,dx}{\varphi_1(L)} \approx 0.862, \tag{2.7}$$

where $f_{Gauss}(x)$ is the force per unit length in the longitudinal direction for the Gaussian distributed pressure, $\varphi_1(x)$ is the normalized eigenfunction of the cantilevers fundamental mode [58,59], w_0 is the beam waist of laser spot, W is the width of the cantilever, and prefactor $B = \sqrt{2/\pi}erf\left(W/\sqrt{2}w_0\right)/w_0$.

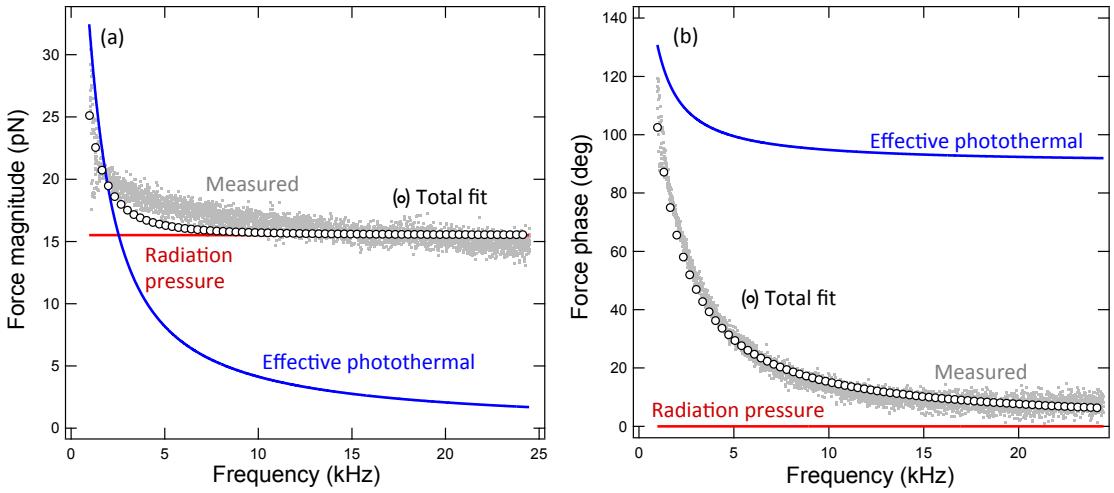

Figure 2.3: Determination of force components (radiation pressure and effective photothermal) under sinusoidal illumination (9.32 mW at $\lambda = 660$ nm). The amplitude and phase of the experimental data are simultaneously fit to Equation (2.3) and applied to Equations (2.4)-(2.6) to determine the force magnitude (a) and phase (b). At low frequencies, the effective photothermal force is dominant, while at high frequencies the radiation pressure force is dominant.

A clear distinction can be made between photothermal and radiation pressure effects for laser excitation rates above a few kHz (Figure 2.3). At low frequencies, the effective photothermal force is larger but decays to about 10% of radiation pressure

force at the resonance frequency (17.632 kHz). Furthermore, because the two forces are nearly 90° out of phase at resonance frequency, when adding in quadrature, the effective photothermal force accounts for less than 1% of the total amplitude at resonance. Therefore the radiation pressure is the dominant driving force for cantilever resonance.

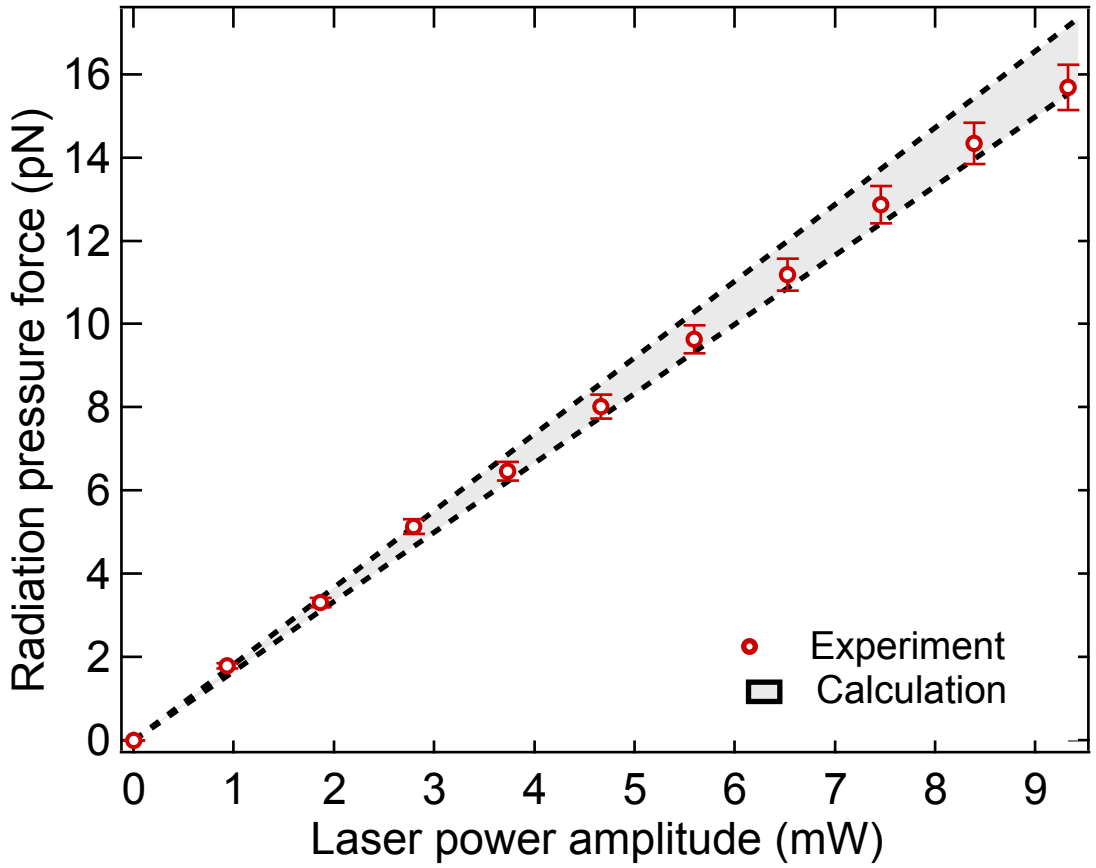

Figure 2.4: Measured and calculated radiation pressure force are in agreement within the experimental and calculated errors. The measured force corresponds to the peak value of the sinusoidal response in the time domain resulting from sinusoidal external illumination.

The measured radiation pressure force agrees with the calculated values from Equation (1.3) (Figure 2.4). To determine the expected radiation force, we use measured values for the laser power and reflectivity from the cantilever. The reflectivity

coefficient, R, is determined from a measurement of the transmitted power through the cantilever, T, as $R = 1-T$. We have taken the absorption in the cantilever to be approximately zero because the absorption coefficient for SiN_x is much smaller than the reflection and transmission coefficients at 660 nm. The shaded area in Figure 2.4 shows the uncertainty in the calculated force based on the uncertainty in the laser power. The error bars on the experimental data result from the uncertainty in the fitting process and the precision of Sader method in determining the spring constant.

2.2 Wavelength dependent radiation pressure due to thin film interference

Previous measurements of radiation pressure are all based on a single wavelength excitation [45,52,60]. It is true that radiation pressure on a perfect reflecting mirror is independent of wavelength and only depends on the incident optical power. However, with real-world materials, different reflection and absorption coefficients at different wavelengths will generate different amounts of radiation pressure given the same incident power. The total radiation force per unit incident power is given by:

$$\frac{F_{rp}}{P} = \frac{2R(\lambda) + A(\lambda)}{c} cos\theta, \tag{2.8}$$

where F_{rp} is the photon radiation force, P is the incident optical power, $R(\lambda)$ and $A(\lambda)$ are the reflection and absorption coefficients at incident angle θ, and c is the speed of light.

Observing the wavelength dependent radiation pressure based on material dispersion is difficult because radiation pressure measurements are usually performed at a wavelength that has little absorption to avoid photothermal effects, but such a wavelength range also has negligible refractive index and optical property changes. However, if a coherent light source is incident on a thin film structure, such as a microcantilever, the thin-film interference effect can cause dramatic change in the optical property within a short wavelength range. Another challenge in the measurement lies in providing the baseline radiation pressure based on the reflection and absorption coefficients, which cannot be calculated from the nominal cantilever thickness because the cantilever thickness is not well controlled in the traditional lithography process and has large variations even from the same batch [61]. Therefore, in-situ measurement of cantilever thickness at the laser excitation position is essential.

Here, we demonstrate the first measurement of radiation pressure across a continuous wavelength spectrum and show the wave-like wavelength dependent radiation pressure due to optical interference in silicon microcantilever. We utilize in-situ optical transmission measurement at the excitation position to determine the local thickness and the angle of incidence in order to calculate the local optical properties. We also demonstrate that the tunable wavelength excitation measurement is a good way to separate photothermal and radiation pressure.

The experimental setup of measuring wavelength dependent radiation pressure is based on a modified atomic force microscope (Asylum Research, Cypher AFM). The combination of the super continuum white fiber laser (Fianium WhiteLase

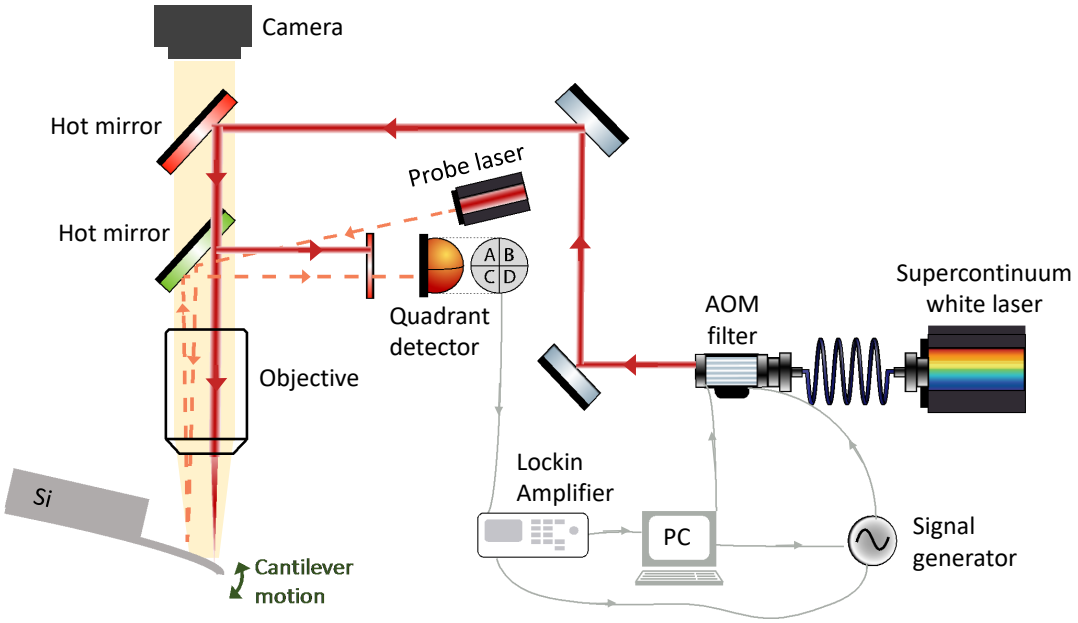

Figure 2.5: Experimental setup for measuring radiation pressure under tunable-wavelength laser excitation. The thin film interference effect in the silicon cantilever causes the cantilever to experience wavelength-dependent radiation pressure and photothermal effects given the same incident optical power for different wavelengths.

SC400UV) and the AOM filter (AOTF with NIR1 crystal) serve as the tunable laser source to excite the oscillation of the silicon cantilever. The laser beam is directed and focused on the backside of the cantilever through the same objective (20×) as the probe laser (860nm). The output optical power of the excitation laser is modulated sinusoidal by driving the AOTF with a sinusoidal reference signal from the lock-in amplifier. The frequency of sinusoidal excitation is swept from near dc across the fundamental frequency of the cantilever to magnify the oscillation. The cantilever deflection is detected by using a quadrant-photodiode to record the probe laser light reflected off the back of cantilever, which is then fed into the lock-in amplifier to obtain the frequency response of the amplitude and phase of the oscillation. An uncoated rectangular cantilever (Mikromasch CSC38) is used in the experiment because silicon has well-known refractive indices across the whole spectrum. An optical power meter (Thorlab PM100D and S130C) is put under the cantilever to measure the optical power transmitted through the cantilever. The wavelength range used in this experiment is between 664 nm and 772 nm. This wavelength window is limited by the output power of the AOTF NIR1 filter and the band-pass filter in front of the quadrant detector used to measure the cantilever deflection (power is too low below 664 nm and excitation above 772 nm will cause stray light into the quadrant photodetector and interfere the probe laser signal due to diffraction within the optical path.)

For the radiation pressure to contribute most effectively to the deflection signal, the excitation laser is focused near the free end of the cantilever. The detection laser is placed near the middle of the cantilever, away from the excitation laser to

avoid the Fano-like resonances caused by stray light and local thermal deformation not coupled into cantilever oscillation [62]. The transmission spectrum of the cantilever at the excitation position is measured to determine the local cantilever thickness and incident angle. This spectrum is the ratio of the power measured underneath the cantilever and the power measured when the cantilever is removed after the experiment, shown in Figure 2.6.

The measured transmission spectrum through the cantilever is used to determine the absorption and reflection from the cantilever. The measured data is fit to the calculated transmission through a single layer of silicon using the transfer matrix method [63]. The two variable parameters in the fitting process are cantilever thickness and incident angle. The incident light is TM polarized, and the index of refraction of Si is obtained from tabulated data [64]. The fitted thickness and incident angle from the measurement are then used to calculate the reflection and absorption (Figure 2.6). It is worth noting that the absorption spectrum is "in-phase" with the transmission spectrum, meaning that their maxima and minima are at the same wavelength while the reflection spectrum is always "out-of-phase" with the transmission spectrum, meaning that their maxima and minima are exactly the opposite. This property, fortunately, can be used to distinguish the dominant driving mechanism of the cantilever. If the measured cantilever amplitude response (normalized by optical power) is opposite to the transmission spectrum, it aligns with the reflection spectrum and indicates that the radiation pressure excitation is dominant. On the other hand, if the measured cantilever amplitude response aligns with the transmission/absorption spectrum peaks, then the photothermal excitation

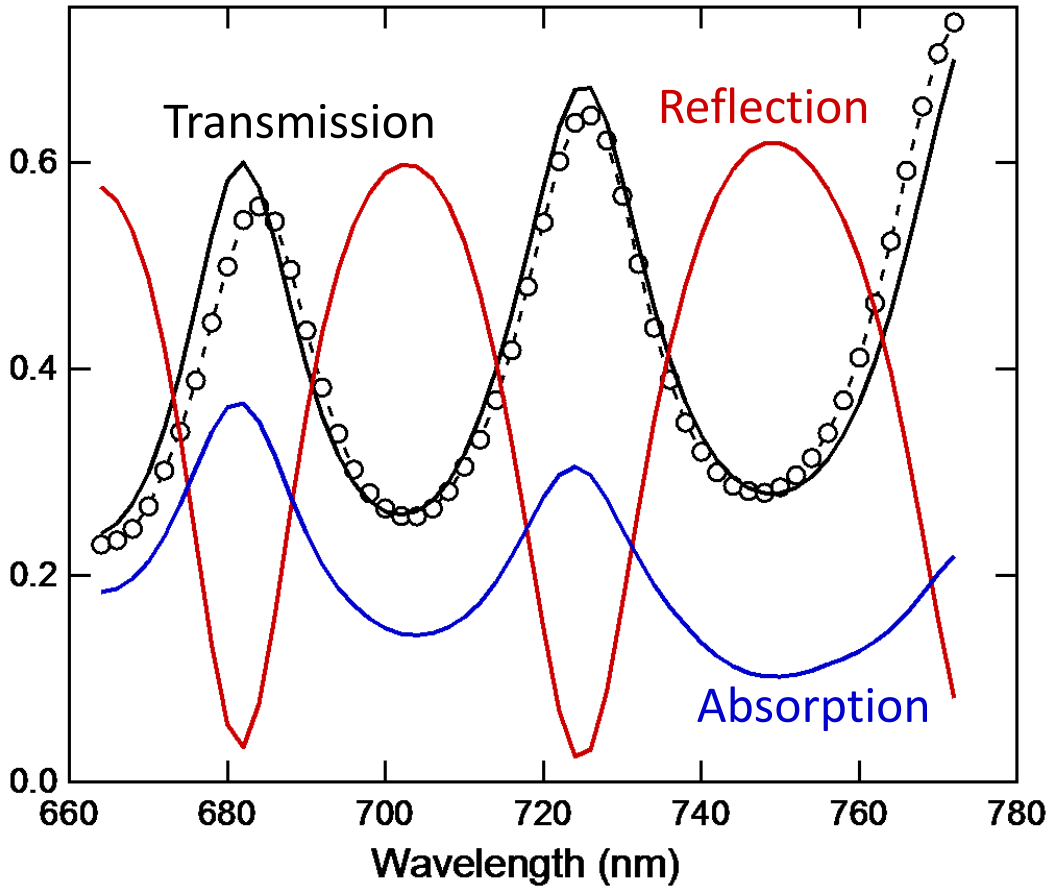

Figure 2.6: (a) Measured and fitted amplitude of cantilever oscillation as a function of excitation frequency (tuning curve) at incident wavelength of 750 nm and laser power of 0.37 mW. (b) Optical properties of the cantilever at the excitation position near the free end of the cantilever. Black circles represent the measured transmission spectrum (2 nm step size). Black solid line represents the fitted transmission spectrum based on the thin film interference. Red and blue solid line represent the reflection and absorption spectrum calculated from the thickness and incident angle obtained from the transmission spectrum fitting.

is dominant.

In order for radiation pressure to be the dominant driving mechanism, the external laser is focused near the free end. The amplitude of cantilever oscillation under sinusoidal excitation is measured every 2 nm for incident wavelengths between 664 nm and 772 nm. At each wavelength, the laser modulation frequency is swept across the fundamental resonance frequency of the cantilever, and the cantilever oscillation amplitudes are recorded, forming a tuning curve (Figure 2.7(a)). Each tuning curve is then fitted to the simple harmonic oscillator model:

$$A(\omega) = A_0 \frac{\omega_0^2}{\sqrt{(\omega_0^2 - \omega^2)^2 + (\omega\omega_0/Q)^2}}, \tag{2.9}$$

to obtain the zero-frequency amplitude A_0, resonant frequency of fundamental mode ω_0 and the quality factor Q. The measured force at each wavelength is calculated by $F_0 = A_0 k_0$, where k_0 is the spring constant of the fundamental frequency calibrated by the thermal method [59]. The measured force (normalized by incident optical power) at each wavelength is compared directly to the optical spectrum (Figure 2.7(a)).

The measured radiation force spectrum agrees with the calculation from Equation (1). The uncertainty in the measurement comes mainly from the spring constant calibration, power measurement and the fitted incident angle. The uncertainty in the calculation comes mainly from the fitting of the transmission spectrum. The minima in the measured force spectrum do not go as deeply as the calculation because the cantilever oscillation driven by the weak radiation pressure due to the

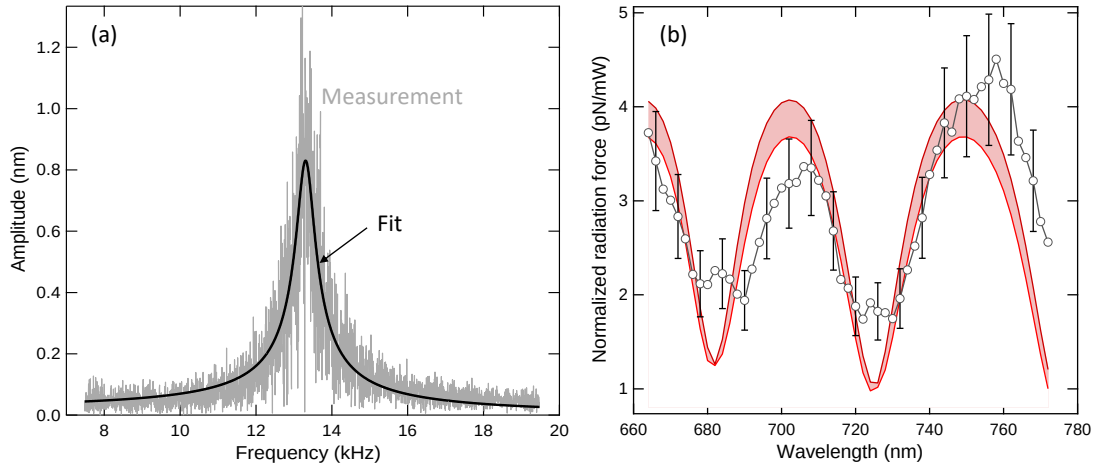

Figure 2.7: (a) Measured and fitted amplitude of cantilever oscillation as a function of excitation frequency (tuning curve) at incident wavelength of 750 nm and laser power of 0.37 mW. (b) Measured and calculated radiation force normalized by the incident optical power F_0/P_0. The red curves represents the F_0/P_0 calculated by Equation (1) using the reflection and absorption spectrum shown in FIG.2. The shaded region shows the uncertainty in the calculated radiation force based on error propagation from the transmission fitting error. The black circle represents the measured F_{rp}/P_{in}, and the error bars are plotted every three data points for clarity.

small reflection coefficient is close to the noise level so that the tuning curve collected is not a good representation of the radiation pressure alone. A significant increase of laser power could potentially increase the accuracy of the measurement.

The tunable wavelength excitation measurement discussed here is also a good way to determine whether the dominant driving mechanism of the cantilever oscillation is radiation pressure or photothermal. To demonstrate this, another experiment is conducted with the external laser excitation near the base of the cantilever. The same procedure is used to obtain the absorption spectrum from the measured transmission spectrum (Figure 2.8).

It is clear that, in the case of excitation near the free end, the normalized cantilever oscillation amplitude aligns with the reflection spectrum (Figure 2.8a), indi-

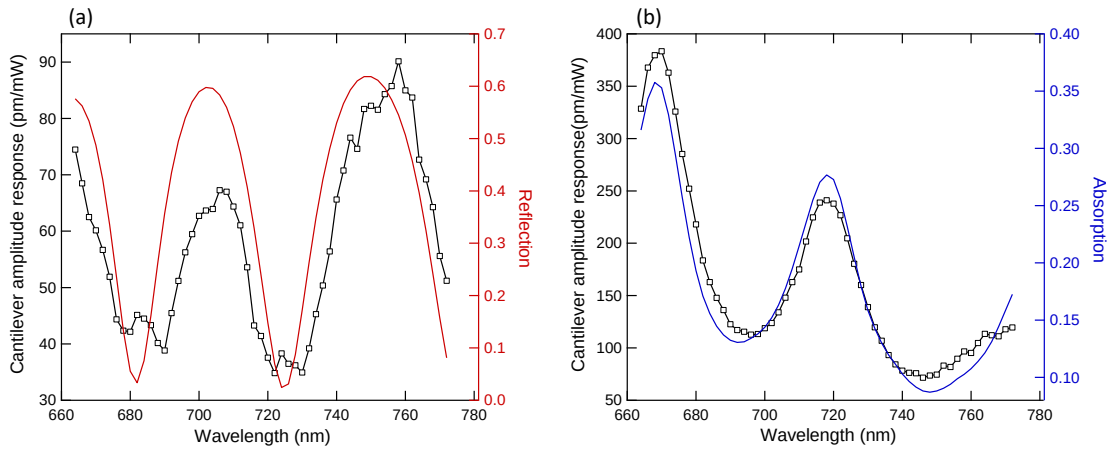

Figure 2.8: Cantilever response for laser excitation (a) near the free end and (b) near the base of the cantilever. Left axis: Cantilever amplitude response (fitted zero-frequency amplitude A_0) normalized by the incident optical power. Right axis: (a) reflection spectrum and (b) absorption spectrum. (a) For excitation near the free end, the maxima in the amplitude response occur when the reflection is also a maximum, showing a radiation pressure dominated behavior. (b) Correlation between absorption maxima and cantilever response for excitation near the base shows behavior is dominated by photothermal effects.

cating the radiation pressure is the dominant driving mechanism. On the contrary, the normalized cantilever oscillation amplitude is proportional to the absorption spectrum when the excitation is near the base, indicating the driving mechanism is the photothermal bending moment caused by photon absorption [55] (Figure 2.8b). The conclusion matches what we discovered in previous work [60].

In summary, we have demonstrated the first measurement of wavelength dependent radiation pressure due to thin film interference of a silicon cantilever over a continuous wavelength range. We developed a technique to obtain the local reflection and absorption spectrum from the in-situ transmission spectrum measurement by fitting the cantilever thickness and incident angle as an intermediate step. We also showed that the tunable wavelength excitation measurement is a good way to

distinguish photothermal driven oscillation (base excitation) from radiation pressure driven oscillation (free end excitation) based the comparison of the normalized cantilever amplitude spectrum and the reflection or absorption spectrum.

2.3 Fano-like resonances in optically driven cantilevers

So far we have discussed two measurements of radiation pressure and photothermal effects. In both experiments, the excitation laser is steered some distance away from the detection laser in order to get a relatively symmetric tuning curve that can be well presented by the simple harmonic oscillator model. When the two laser spots come close to each other, asymmetric cantilever resonances are observed and become a significant road block for the radiation pressure measurement. In this section, we show that the asymmetric resonance can be explained as a Fano resonance, an interference between a resonant component and a continuous component. When the continuous component is small, we show that it is still possible to retrieve the resonance information through fitting of the complex Fano expression.

The frequency response of the cantilever oscillation can become more complex complicated under optical excitation due to various coupling mechanisms, and it is necessary to go beyond the simple harmonic oscillator model. Asymmetric resonance curves often appear when the excitation and detection laser spots are close in space, regardless of whether it is driven by photothermal effects or radiation pressure. The asymmetric amplitude resonance and abnormal phase change either larger or less than π can be explained by a Fano resonance, which is the interference between a

resonant term and a non-resonant/continuum term [62]:

$$A(\omega) = \frac{A_r \omega_0^2}{\omega_0^2 - \omega^2 + i\omega\omega_0/Q} + A_c, \tag{2.10}$$

where A is the total complex amplitude phaser, A_r is the zero-frequency amplitude of the resonance term and A_c is the amplitude of the continuum term, both of which can be complex numbers.

Equation 2.10 can be used to fit both the amplitude and phase of the asymmetric resonance to retrieve A_r and A_c. ω_0 and Q are also used as variable parameters in the fitting. The parameters can be well-determined by the fit as long as the continuum term A_c is not too large compared with A_r. The comparison of A_r and A_c can be visualized by projecting the cantilever response $A(\omega)$ in a Nyquist plot (2.9(c)). A Nyquist plot is a parametric plot of the complex amplitude as a function of modulation frequency where the real component is on the x-axis and the imaginary component is on the y-axis. Each point on the Nyquist plot represents the complex cantilever vibration amplitude at a given modulation frequency. The radius of the resonance circle on the Nyquist plot represents the magnitude of the resonant term A_r and the offset of the circle's center in x-axis (from zero) represents the magnitude of the non-resonant term A_c.

The origin of the non-resonant term A_c is complicated and can result from a variety of phenomena as described below. For a typical AFM experimental setup, there is no narrow band-pass filter in front of the detection laser, so A_c mainly comes from the stray light of the excitation laser scattered into the quadrant photodetector.

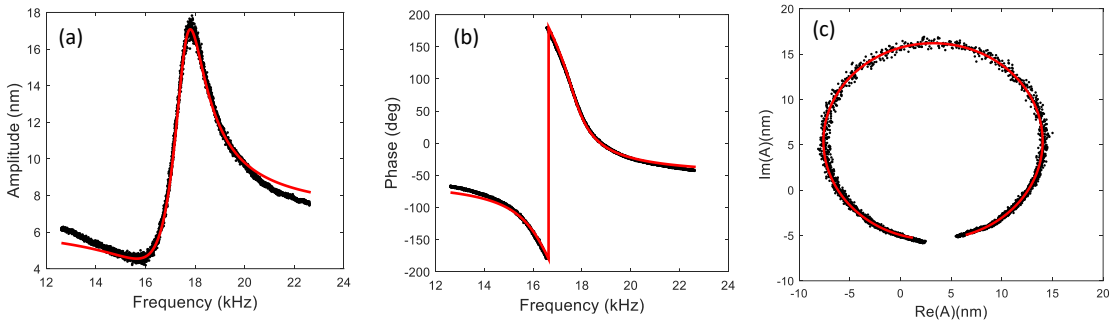

Figure 2.9: Fitting of the experimental tuning curve using the Fano expression. Black dots are the measured data and the red line is the fit.

This light is the dominant contribution to A_c even when the excitation laser is far away from the detection laser. When a narrow band-pass filter is added in front of the photodetector, stray light from the excitation laser is reduced to a negligible level. However, a Fano resonance still exists when the excitation laser comes close to the detection laser. One possible explanation is that there is some local thermal bulging that deflects the deflection laser, which is not coupled to the cantilever beam oscillation. A supporting evidence for this hypothesis is that when the excitation laser spot is swept across the detection laser spot, the A_c term from the Fano fitting changes sign.

The cantilever's amplitude of oscillation depends on the position of the excitation beam on the cantilever, which also affects whether the bending is due to photothermal effects or radiation pressure. In order to show that the oscillation of cantilever is dependent on the excitation positions, the excitation laser spot is swept from near the base to the free end of a silicon nitride cantilever. The detection laser spot is fixed near the middle of the cantilever. Fano resonances exist for nearly all excitation positions on the cantilever, besides the two extremes (near the base and

free ends). Therefore fitting to the Fano resonance expression is necessary to reveal the actual cantilever oscillation when the excitation is in the middle. Figure 2.10 shows the fitting of the experimental tuning curve to the Fano resonance expression in the Nyquist plot format as the excitation laser position moves from the base (top left) to the free end (bottom right). From the radius of the Nyquist plot, it is easy to see the trend of the magnitude of the resonant term Ar, which is also shown in Figure 2.11. The amplitude trend with excitation position follows what we predicted in previous sections and what is found in the literature [55], resulting in cantilever bending that is a combination of photothermal and radiation pressure effects. The influence of the photothermal phenomenon is strongest when the excitation position is near the base while radiation pressure is dominant for excitation near the free end.

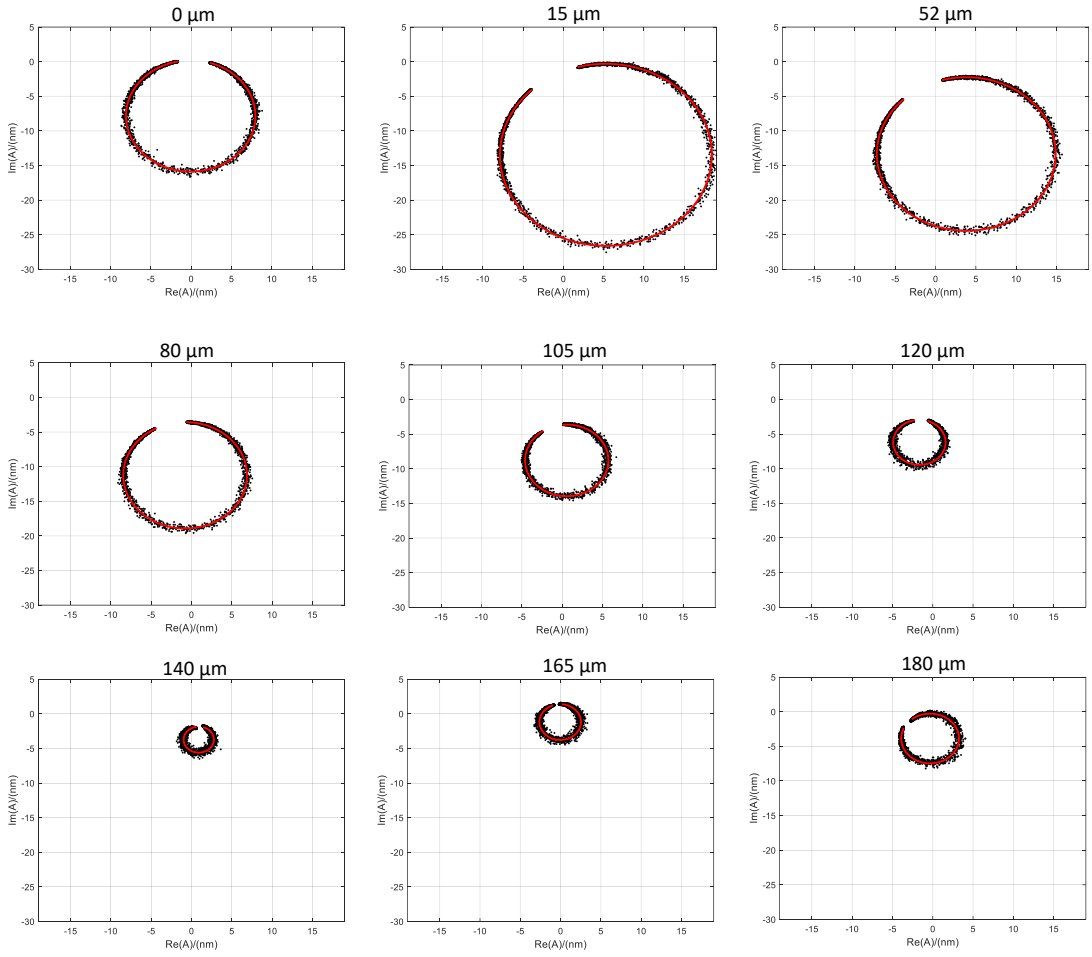

Figure 2.10: Nyquist plots showing the fitting of the complex cantilever oscillation amplitude using the Fano expression under different laser excitation positions on the cantilever (0 μm corresponds to the base and 180 μm corresponds to the free end). Black dots are the measured data and the red lines are the fit.

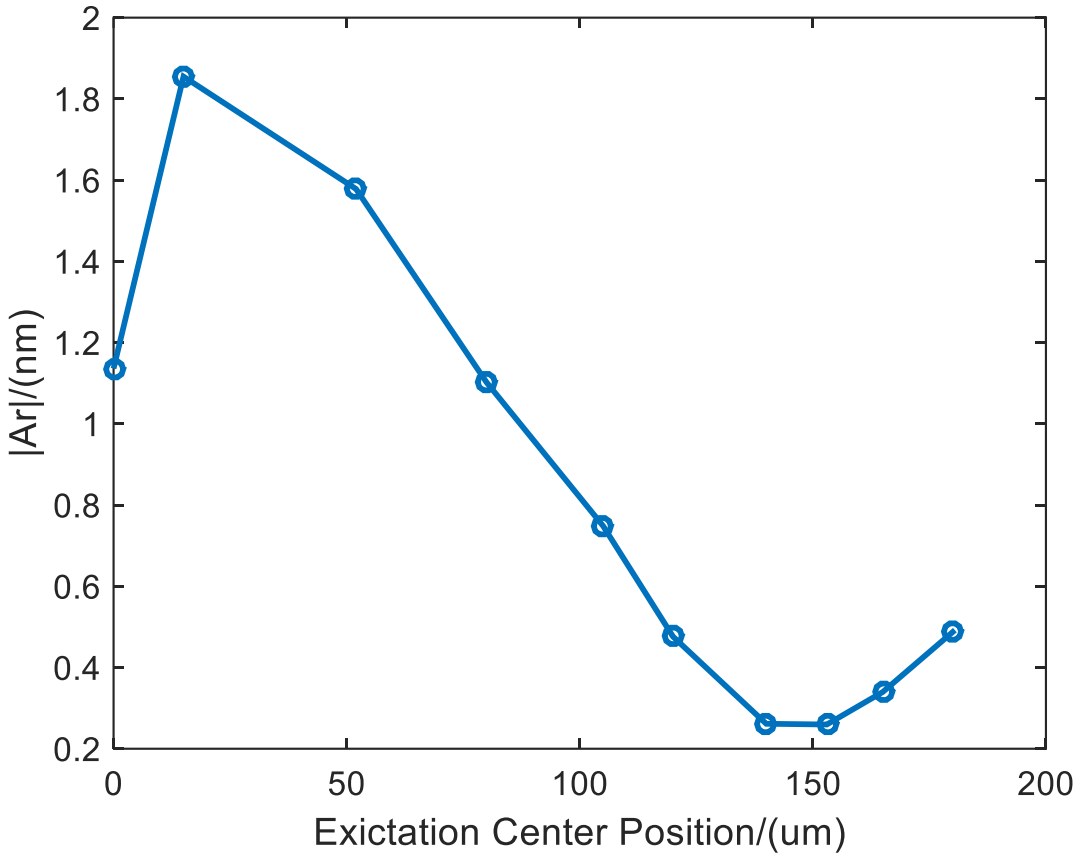

Figure 2.11: Magnitude of the fitted resonant amplitude in the Fano expression as a function of excitation position.

Chapter 3: Cantilever beam theory

3.1 Static bending

Before discussing the dynamics of the cantilever beam's oscillation we calculate the cantilever bending under a static load. Figure 3.1 shows a typical rectangular cantilever. The moment-curvature relationship for a homogeneous beam when the

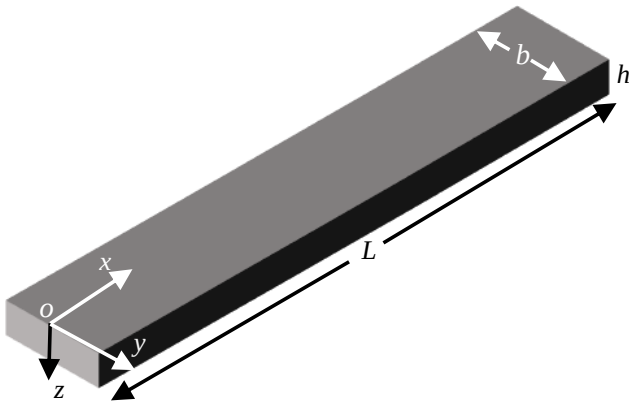

Figure 3.1: A cantilever with length L, width b, and thickness h,

deflection is small compared to its length is given by

$$M(x) = -EI\frac{d^2w(x)}{dx^2}, \tag{3.1}$$

where $M(x)$ is the bending moment (*i.e.* the sum of the moments/torques about position x caused by all the forces and moments on one side of x) [65], E is the Young's modulus of cantilever material, I is the area moment of inertia and $w(x)$ is the cantilever deflection in the z-direction. For a homogeneous beam along the x axis, E and I are independent of x. Because the rotation is about the y-axis, I is given by

$$I = \int_A y^2 dA = \int_A y^2 dz dy = \frac{1}{12} b h^3. \tag{3.2}$$

The total bending moment is a linear combination of the mechanical moment and the thermal moment:

$$M = M_M + M_T, \tag{3.3}$$

where M_M is the mechanical moment due to external forces and reaction forces at the boundary of the beam, and M_T is the thermal moment due to a temperature gradient or a carrier gradient in the thickness direction (z) of the cantilever. Positive bending moment is defined to be counter-clockwise in Figure 3.2. Using the moment-curvature relationship and the boundary conditions for a cantilever, *i.e.* $w(0) = 0$ and $\frac{dw}{dx}|_{w=0} = 0$, it is possible to obtain analytical solutions of beam deflection under different loading conditions.

Here we consider one simple example: a point force is applied to the cantilever at position x_0 (Figure 3.2). The bending moment is:

$$M(x) = \begin{cases} F_0(x - x_0), & x \leq x_0 \\ 0, & x > x_0 \end{cases}. \tag{3.4}$$

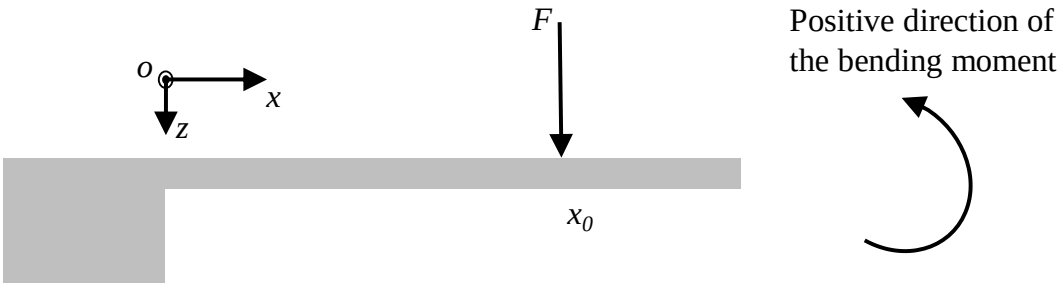

Figure 3.2: A simple load: a point force is applied to the cantilever at position x_0. The positive direction of the bending moment is defined to be counterclockwise.

After integration of Equation 3.1 and applying the boundary conditions, the deflection is

$$w(x) = \begin{cases} \frac{F_0 x^2}{6EI}(3x_0 - x), & x \leq x_0 \\ \frac{F_0 x_0^2}{6EI}(3x - x_0), & x > x_0 \end{cases}. \tag{3.5}$$

If the force is applied to the free end of the cantilever, *i.e.* at $x_0 = L$, the deflection at the free end is $w(L) = \frac{F_0 L^3}{3EI}$.

3.2 Cantilever vibration and eigenmodes

Small flexural deflection and vibration of cantilevers can be calculated with Euler–Bernoulli beam theory [66]. Below is a derivation of the equation of motion of the cantilever under an external force and thermal moment, starting with the force analysis of an infinitesimal cantilever section (Figure 3.3). From Newton's second law of motion, we have:

$$V(x + \Delta x, t) - V(x, t) + f(x, t) = (\mu \Delta x)\frac{\partial^2 w(x, t)}{\partial t^2}, \tag{3.6}$$

where $V(x,t)$ is the internal shear force on the infinitesimal element, $f(x,t)$ is the linear density of the shear force along x axis, and μ is the linear mass density of the beam along x axis. Dividing by Δx on both sides of the equation and in the limit of $\Delta x \to 0$, we obtain:

$$\mu \frac{\partial^2 w}{\partial t^2} = \frac{\partial V(x,t)}{\partial x} + f(x,t). \tag{3.7}$$

Because the mechanical bending moment and the shear force are related by $\frac{dM_M}{dx} = V$, and the moment-curvature relationship is $M_M + M_T = -EI\frac{d^2w}{dx^2}$, Equation 3.7 becomes the governing equation of motion:

$$EI\frac{\partial^4 w}{\partial x^4} + \mu\frac{\partial^2 w}{\partial t^2} = f(x,t) - \frac{\partial^2 M_T}{\partial x^2}. \tag{3.8}$$

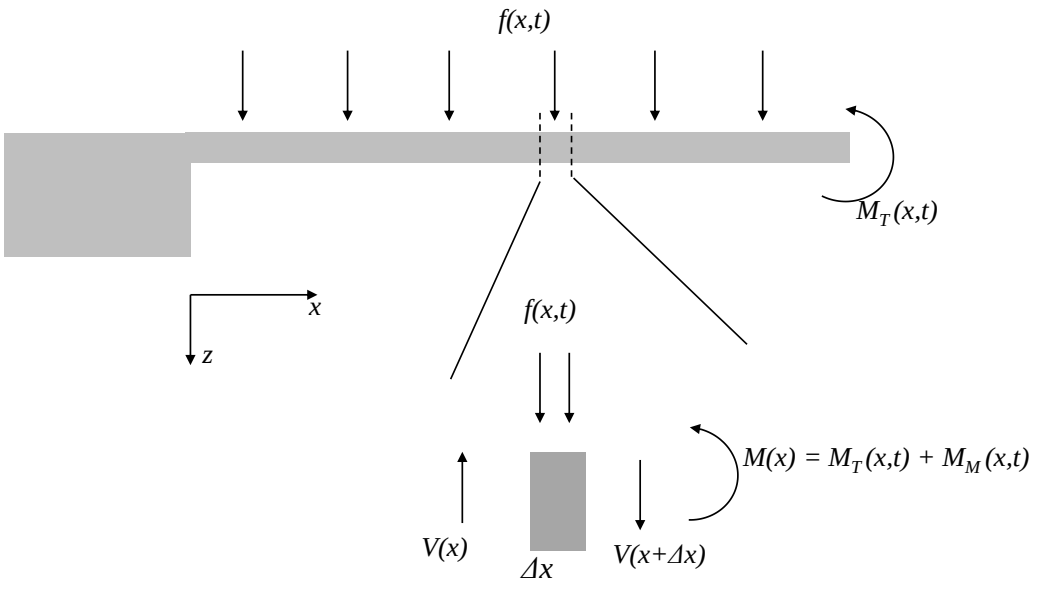

Figure 3.3: Force analysis of an infinitesimal cantilever section under a linear transverse force density $f(x,t)$ and a thermal moment $M_T(x,t)$.

In the absence of a transverse load ($f(x,t) = 0$) and thermal moment ($M_T(x,t) =$

0), we have the free vibration equation:

$$EI\frac{\partial^4 w}{\partial x^4} + \mu\frac{\partial^2 w}{\partial t^2} = 0. \tag{3.9}$$

To solve equation 3.9 using the eigenmode expansion method, we assume the vibration is in the form of $w(x,t) = \mathrm{Re}[w(x)e^{-i\omega t}]$, where ω is the angular frequency of vibration. This leads to an ordinary differential equation:

$$\frac{d^4 w(x)}{dx^4} - \beta^4 w = 0, \tag{3.10}$$

where $\beta^4 = \mu\omega^2/EI$. The general solution to the above equation is

$$w(x) = A_1\cosh(\beta x) + A_2\sinh(\beta x) + A_3\cos(\beta x) + A_4\sin(\beta x) \tag{3.11}$$

The boundary conditions for a cantilever beam of length L (fixed at $x = 0$) are

$$\begin{aligned} &w(0) = 0, \\ &\tfrac{dw}{dx}|_{x=0} = 0, \\ &\tfrac{d^2w}{dx^2}|_{x=L} = 0, \\ &\tfrac{d^3w}{dx^3}|_{x=L} = 0. \end{aligned} \tag{3.12}$$

The last two boundary conditions are due to the fact that both the bending moment and shear force at the cantilever's free end are zero. By applying the boundary conditions and the orthorganality condition: $\int_0^L \phi_m^0\phi_n^0 dx = \delta_{mn}$, we obtain the normalized

eigenmode of vibration for the nth flexural mode:

$$\phi_n^0(x) = \frac{1}{\sqrt{L}}\{\cos(\beta_n x) - \cosh(\beta_n x) - \frac{\cos(\beta_n L) + \cosh(\beta_n L)}{\sin(\beta_n L) + \sinh(\beta_n L)}[\sin(\beta_n x) - \sinh(\beta_n x)]\}, \tag{3.13}$$

where $\beta_1 L = 1.875$, $\beta_2 L = 4.694$, and $\beta_3 L = 7.855$. From the eigenfunction, we know that the nth flexural mode has $n-1$ nodes ($\phi_n^0(x) = 0$), and the first three eigenfrequencies have ratios: $\omega_1 : \omega_2 : \omega_3 = 1 : 6.25 : 17.55$.

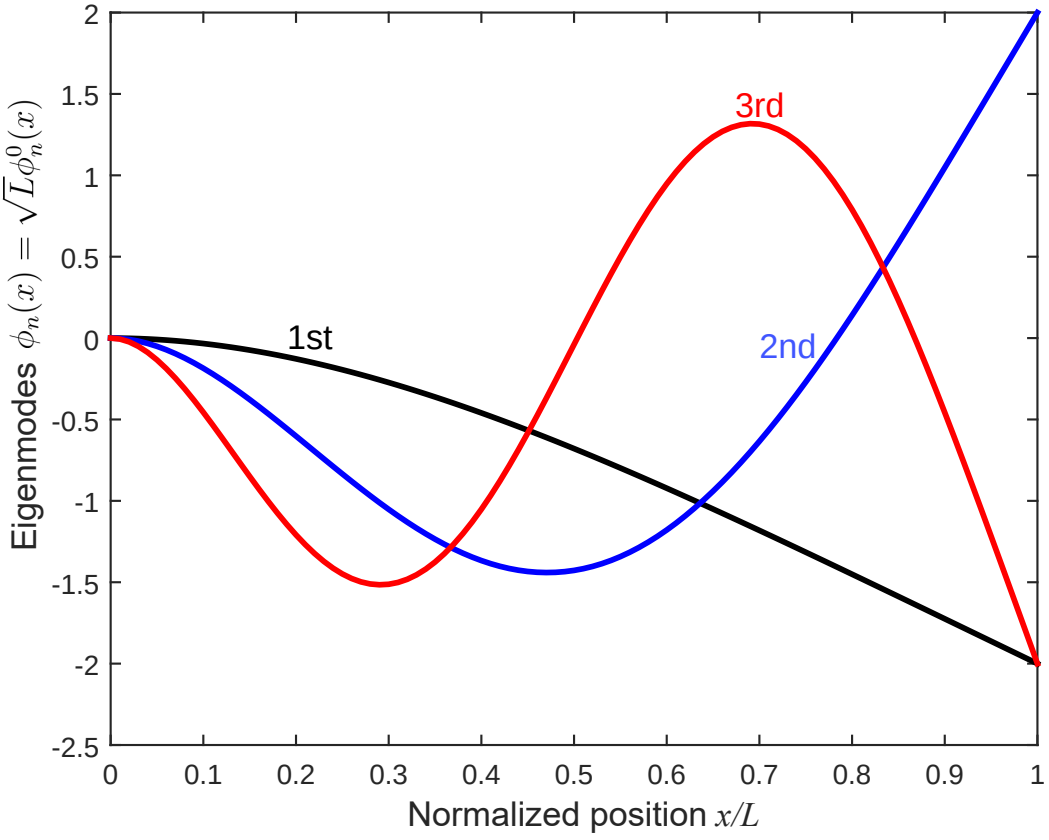

Figure 3.4: First three flexural vibration eigenmodes of the cantilever.

3.3 Forced vibration under an external force

If the cantilever is forced to vibrate under a harmonic transverse force $f(x,t) = \mathrm{Re}[f(x)e^{i\omega t}]$, Equation 3.8 becomes

$$\frac{d^4w(x)}{dx^4} - \beta^4 w(x) = \frac{f(x)}{EI}. \tag{3.14}$$

We assume a solution of the form $w(x) = \sum A_n(x) = \sum C_n\phi_n^0(x)$, where $A_n(x)$ is the oscillation amplitude of the nth mode. Inserting this solution into Equation 3.8, we obtain:

$$\sum C_n \frac{d^4\phi_n^0(x)}{dx^4} - \beta^4 \sum C_n\phi_n^0(x) = \frac{f(x)}{EI}. \tag{3.15}$$

Because the eigenfunctions follow the eigenequations:

$$\frac{d^4\phi_n^0(x)}{dx^4} - \beta_n^4\phi_n^0(x) = 0, \tag{3.16}$$

Equation 3.14 turns into:

$$\sum C_n(\beta_n^4 - \beta^4)\phi_n^0(x) = \frac{f(x)}{EI}. \tag{3.17}$$

Integrating on both sides:

$$\int_0^L \phi_m^0(x) \sum C_n(\beta_n^4 - \beta^4)\phi_n^0(x)dx = \int_0^L \phi_m^0 \frac{f(x)}{EI}dx,$$

and applying the orthogonality condition, we obtain:

$$C_n = \frac{1}{EI}\frac{\int_0^L \phi_n^0(x) f(x) dx}{\beta_n^4 - \beta^4}. \tag{3.18}$$

We can replace E with a complex elastic modulus $\hat{E} = E(1 + i\eta)$, where the imaginary part η is responsible for the dissipation in the cantilever system [58]. We then get:

$$\beta^4 = \mu\omega^2(1 - i\eta)/EI, \tag{3.19}$$

and

$$C_n = \frac{\int_0^L \phi_n^0(x) f(x) dx}{\mu[\omega_n^2(1 - i\eta) - \omega^2]}. \tag{3.20}$$

Therefore, the amplitude of cantilever oscillation in the nth mode is:

$$A_n(x) = C_n\phi_n^0(x) = \frac{[\int_0^L \phi_n^0(x) f(x) dx]\phi_n^0(x)}{\mu[\omega_n^2(1 - i\eta) - \omega^2]}. \tag{3.21}$$

Because the physical mass of the cantilever $m = \mu L$ and the quality factor $Q = 1/\eta$, and we let $\phi_n(x) = \sqrt{L}\phi_n^0(x)$, we obtain:

$$A_n(x) = \frac{[\int_0^L \phi_n(x) f(x) dx]\phi_n(x)}{m[\omega_n^2 - \omega^2 - i\omega_n^2/Q]}. \tag{3.22}$$

The above equation enables us to calculate the amplitude of oscillation along the cantilever in the nth mode given the distribution of the external transverse force. However, the physical mass of the cantilever m is usually not known *a priori* nor can it be measured easily, so we need to transform it into quantities we can actu-

ally measure and calibrate in the experiment, *e.g.* resonance frequency and spring constant.

We know that for a simple point-mass-on-spring system, mass m_p, spring constant k_p and resonance frequency ω_p are related by:

$$m_p = k_p/\omega_p^2. \tag{3.23}$$

The equivalent point mass of a cantilever is related to the physical mass of the cantilever m based on an equivalent principle developed in [67]. For a uniform rectangular cantilever, it is given by:

$$m_n^{eq} = m/4, \tag{3.24}$$

and the equivalent mass follows the relationship:

$$m_n^{eq} = k_n/\omega_n^2, \tag{3.25}$$

where k_n and ω_n are the spring constant and resonant frequency of the nth mode respectively. By substitution into Equation 3.22, we have:

$$A_n(x) = \frac{\omega_n^2[\int_0^L \phi_n(x)f(x)dx]\phi_n(x)}{4k_n(\omega_n^2 - \omega^2 - i\omega_n^2/Q)}. \tag{3.26}$$

Because $\phi_n(L) = \pm 2$, the equation becomes:

$$A_n(x) = \frac{\omega_n^2[\int_0^L \phi_n(x) f(x) dx]\phi_n(x)}{\phi_n^2(L) k_n(\omega_n^2 - \omega^2 - i\omega_n^2/Q)}. \tag{3.27}$$

For a point force exerted on the free end of the cantilever, $f(x) = F_0\delta(x - L)$, the amplitude at free end is:

$$A_n(L) = \frac{\omega_n^2 F_0}{k_n(\omega_n^2 - \omega^2 - i\omega_n^2/Q)}, \tag{3.28}$$

and near resonance $\omega \approx \omega_n$, it becomes the simple harmonic oscillator (SHO) equation:

$$A_n(L) = \frac{\omega_n^2 F_0}{k_n(\omega_n^2 - \omega^2 - i\omega\omega_n/Q)}. \tag{3.29}$$

Now that we can convert the vibration of a continuum cantilever into a SHO model when a point force is exerted at the free end, we will generalize the method to any arbitrary distributed force by introducing the effective force of the nth mode $F_{n,eff}$. This method converts any distributed load to an effective point force at the free end that causes the same oscillation of the cantilever near the nth resonant frequency. It is easier to compare the effects of different loads when they are all converted to a single point force at the free end of the cantilever. From Equation 3.27 and Equation 3.28, we get:

$$A_n(L) = \frac{\omega_n^2[\int_0^L \phi_n(x) f(x) dx]\phi_n(L)}{\phi_n^2(L) k_n(\omega_n^2 - \omega^2 - i\omega_n^2/Q)}. \tag{3.30}$$

We define the effective force of the nth mode as:

$$F_{n,eff} = \frac{\int_0^L \phi_n(x) f(x) dx}{\phi_n(L)}. \tag{3.31}$$

Therefore the amplitude of oscillation under this effective force excitation near the nth resonant frequency is:

$$A_n(x) = \frac{\omega_n^2 F_{n,eff} \phi_n(x)}{k_n(\omega_n^2 - \omega^2 - i\omega\omega_n/Q)}. \tag{3.32}$$

3.4 Forced vibration under an external bending moment

If the beam is forced to vibrate under an external bending moment, such as a thermal moment caused by a temperature gradient, still assuming harmonic excitation ($M_T(x,t) = Re[M_T(x)e^{i\omega t}]$), Equation 3.8 becomes:

$$\frac{d^4 w(x)}{dx^4} - \beta^4 w(x) = -\frac{1}{EI}\frac{d^2 M_T(x)}{dx^2}. \tag{3.33}$$

Replacing $f(x)$ with $-\frac{d^2 M_T}{dx^2}$ in Equation 3.31, we get the effective force of the nth mode from the thermal moment:

$$F_{n,eff} = -\frac{1}{\phi_n(L)} \int_0^L \phi_n(x) \frac{d^2 M(x)}{dx^2} dx, \tag{3.34}$$

and the amplitude of oscillation can be calculated from Equation 3.32.

Chapter 4: Photon absorption induced bending

4.1 Introduction

There are many other mechanisms by which a modulated laser could excite vibration in micromechanical structures beside radiation pressure. These mechanisms involve situations where the electromagnetic energy from light is first transferred to other forms of energy by means of photon absorption, not directly to the mechanical kinetic energy of microstructures. Silicon or silicon nitride AFM cantilevers are typically coated with a thin layer of metal (*e.g.* aluminum) to improve reflectivity. In this case, the dominant photothermal excitation mechanism is the bimorphic/bimetallic bending effect caused by the different thermal expansion coefficients between Si/SiN_x and the coating layer [52, 68]. For uncoated cantilevers, thermal gradients through the cantilever thickness creates a bending moment, often referred to as photothermal/thermal-elastic bending (TE) [55, 69, 70]. Furthermore, for uncoated cantilevers made of semiconductors (*e.g.* silicon), excess photo-generated carrier will cause electronic strain within the structure known as photostriction effect [71]. Carrier density gradients through the cantilever thickness will generate a bending moment, often referred to as electronic-elastic bending or electronic deformation (ED) [71–73]. Besides bending generated by stress and strain within the

cantilever itself, cantilevers in rarified gas environment may experience radiometric forces resulting from thermally driven gas flow caused by non-equilibrium temperature gradients in a fluid [53]. This force is also known as Knudsen force within the AFM community [74]. It becomes noticeable in vacuum systems where the mean free path is comparable to the flow gradient length scale. However, because our measurement is conducted in the ambient environment, where the mean free path of the gas is much smaller than the characteristic length between the cantilever and other surfaces, the radiometric force is not dominant [74]. Therefore, this chapter focuses on the discussion of the three optical absorption induced bending effects: bimorphic, thermal-elastic and electronic deformation.

4.2 Bimetallic bending of a coated cantilever

Most materials expand when they are heated. For isotropic materials, the thermal strain ε_{th} is calculated by:

$$\varepsilon_{th} = \alpha \Delta T, \tag{4.1}$$

where α is the thermal expansion coefficient and ΔT is the temperature increase. For a coated cantilever, two materials with different thermal expansion coefficients tend to expand different amount. However, when they are bonded together, they cannot expand freely. This will generates a longitudinal stress that causes a bending moment (Figure 4.1).

The calculation of bimetallic/bimorphic excitation can be divided into two

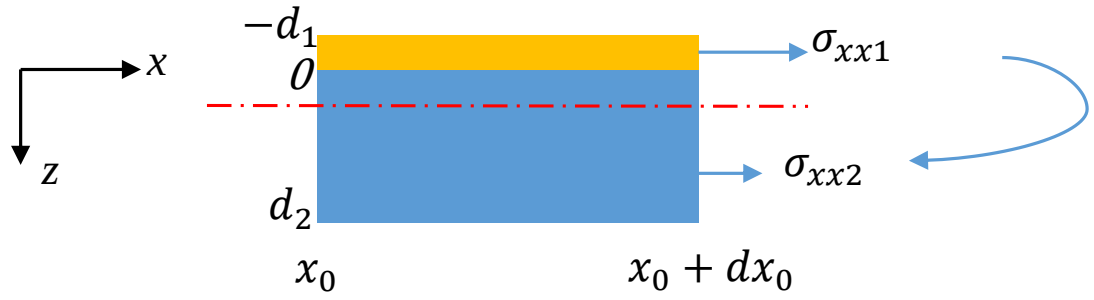

Figure 4.1: Infinitesimal length of the cantilever generates a bending moment due to the longitudinal thermal stress caused by a thermal expansion difference between two different materials. Dash-dot line is the neutral axis of the composite beam (where the stress is zero). $\sigma_{xxi}(i = 1, 2)$ is the normal stress of the cross section in x-axis for each material respectively.

stages. The first stage is to calculate the temperature profile along the cantilever caused by the local periodic heating due to absorption of the optical energy. The second stage is to calculated the bending moment due to the difference in the thermal expansion coefficients between the coating layer and the cantilever material. The bending moment is then converted to a excitation position dependent effective force for the fundamental mode using the method developed in Chapter 3 in order to compare directly with the radiation pressure.

4.2.1 Temperature distribution upon illumination

An intensity modulated laser causes periodic local heating through photon absorption and temperature increase of the cantilever. Because the thermal diffusion length is much larger than the thickness and the bimetallic effect is the dominant driving mechanism of coated cantilevers, it is reasonable to assume the temperature gradient along the cantilever thickness is negligible (thermal diffusion length is much larger than the thickness), and the temperature is also assumed to be the same

across the width direction as the laser spot is comparable to the cantilever width W. Therefore, the time-dependent temperature distribution $T(x,t)$ can be described by the one-dimensional heat diffusion equation [68]:

$$\frac{\partial T}{\partial t} = K\frac{\partial^2 T}{\partial x^2} - \beta T, \tag{4.2}$$

where K and β are given by:

$$K = \frac{\kappa_1 d_1 + \kappa_2 d_2}{c_{p1}\rho_1 d_1 + c_{p2}\rho_2 d_2} \tag{4.3}$$

and

$$\beta = \frac{h_1 + h_2}{c_{p1}\rho_1 d_1 + c_{p2}\rho_2 d_2}, \tag{4.4}$$

where κ is the thermal conductivity, ρ is the mass density, c_p is the specific heat, h is the heat transfer coefficient of convective cooling in air and the subscript 1 and 2 represent the aluminum coating and the silicon cantilever respectively. (Note that the expression of K in [68] is incorrect.) Because the temperature oscillates with the light intensity, it has the harmonic form $T(x,t) = T_0 + \Delta T(x)e^{i\omega t}$, which modifies Equation 4.2 to:

$$K\frac{\partial^2 \Delta T(x)}{\partial x^2} - (\beta + i\omega)\Delta T(x) = 0, \tag{4.5}$$

with the boundary condition:

$$\frac{\partial T}{\partial x}|_{x=L} = -\frac{h_1 d_1 + h_2 d_2}{\kappa_1 d_1 + \kappa_2 d_2}(T(L) - T_0). \tag{4.6}$$

The full solution to Equation 4.5 is shown in [68], however, the effect of the reflected thermal wave is negligible in further calculations, so our solution is simplified to:

$$\Delta T(x) = \Delta T(x_0) exp[-(\frac{1}{\delta_{th}} + i\frac{2\pi}{\lambda_{th}})|x - x_0|], \tag{4.7}$$

where

$$\delta_{th} = \sqrt{\frac{2K}{\beta + (\beta^2 + \omega^2)^{1/2}}} \tag{4.8}$$

and

$$\lambda_{th} = 2\pi\sqrt{\frac{2K}{-\beta + (\beta^2 + \omega^2)^{1/2}}}, \tag{4.9}$$

and x_0 is the laser illumination position and $\Delta T(x_0)$ is the amplitude of the thermal wave at x_0 deduced by making a heat balance at x_0, as given in [68]. Here it is assumed that the optical power is uniformly distributed along the thickness of the cantilever.

To visualize the results of this derivation, numerical parameters are used in following plots with incident laser power of 5 mW. At a wavelength of 660 nm, about 10% of the optical power is absorbed and turned into heat, while the other 90% is reflected by the 30 nm Al coating and 1 μm-thick silicon cantilever.

Figure 4.2 shows the temperature increase (amplitude) when the laser modulation frequency is at 10 kHz, close to the cantilever's first resonant frequency. The temperature change decreases exponentially as the position moves away from the excitation center. How fast the temperature change drops with the position is determined by the thermal diffusion length, which is a function of frequency.

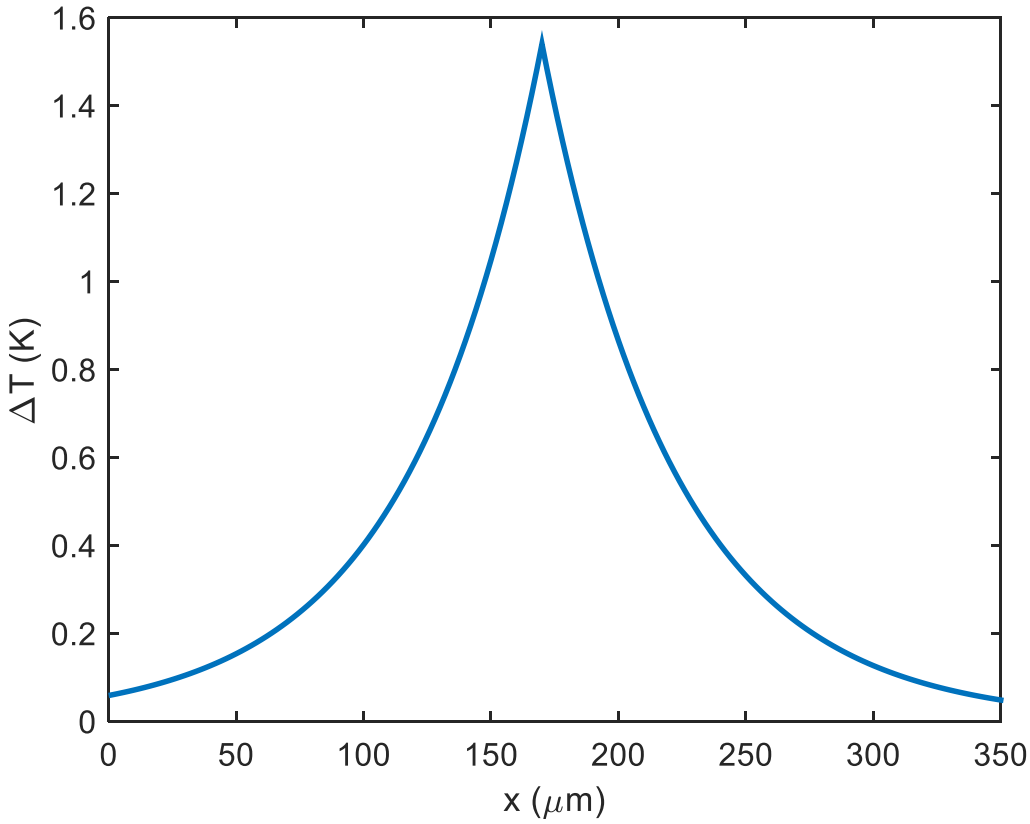

Figure 4.2: Calculation of the temperature increase distribution along the x-axis for a 350 μm-long Al coated silicon cantilever when the intensity modulated laser is focused at the middle of the cantilever ($x_0 = 175$ μm). The modulation frequency is 10 kHz.

Increasing the laser modulation frequency will decrease the temperature increase because the thermal equilibrium can not keep up with the fast change of laser power. Figure 4.3 shows the frequency response of the peak temperature change (at the excitation position). The temperature increase drops significantly when the modulation frequency reaches about 1 kHz. This coincide with the rough estimate of the thermal relaxation time given by [75]:

$$\tau = \frac{L^2}{3}\frac{c_{p1}\rho_1 d_1 + c_{p2}\rho_2 d_2}{\kappa_1 d_1 + \kappa_2 d_2} = 0.5 \text{ ms}. \tag{4.10}$$

However, the drop of temperature increase with frequency does not ensure that the bimetallic effect completely goes away at higher frequency because even small temperature increases can still generate large amounts of bending.

As a side note, at low frequencies the temperature increase seems to be quite high; however, this echoes with what we observed in experiments. High laser power (about 50 mW) on an uncoated Si cantilever (which can has higher absorption than the calculated case) for an extended period of time could cause noticeable damage to the cantilever (Figure 4.4). In reality the temperature increase at the center of the beam is higher than the calculation because the power is also confined to a small spot in the width direction rather than the assumed uniform distribution in the calculation.

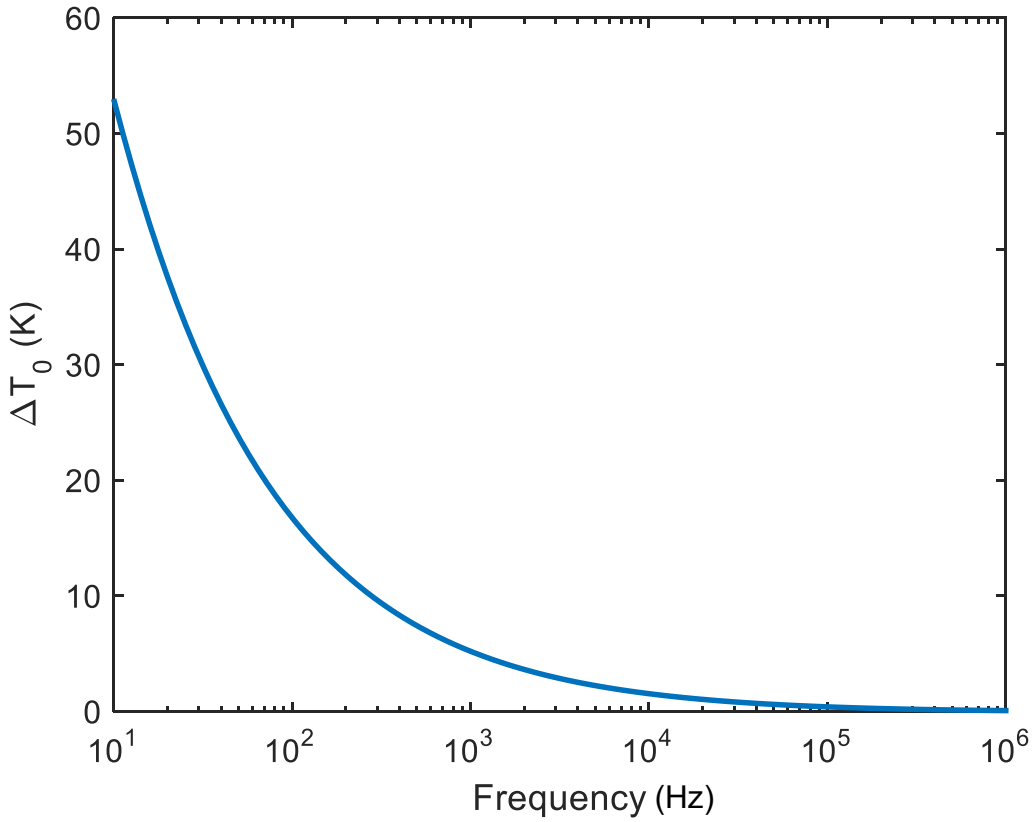

Figure 4.3: Calculation of the frequency response of the temperature increase at the illumination position.

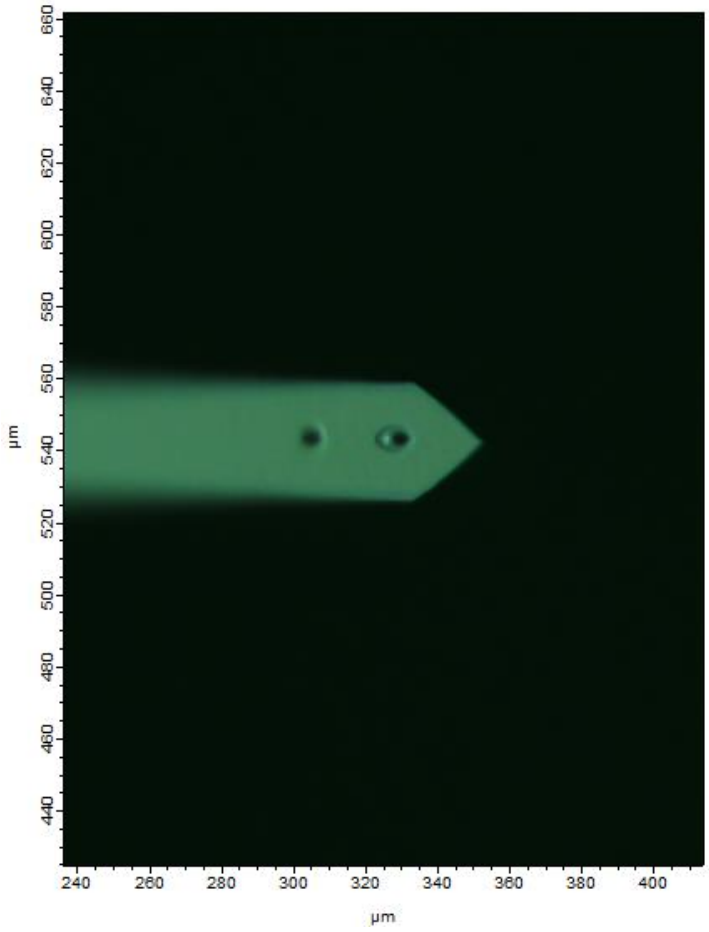

Figure 4.4: Image of damages to a Si cantilever under extended high laser power illumination during an experiment.

4.2.2 Bending moment and effective force

To calculate the bending moment and the effective force based on the temperature distribution, we go back to Figure 4.1. The bending moment at x (observation) caused by the thermal stress at position x_0 (source) is:

$$M(x;x_0) = \Delta T(x_0) W [\int_{-d_1}^{0} \alpha_1 E_1 (z - z_0) dz + \int_{0}^{d_2} \alpha_2 E_2 (z - z_0) dz] H(x - x_0), \quad (4.11)$$

where W is the width of the cantilever, d_i,α_i,E_i are the thickness, thermal expansion coefficient and Young's Modulus of the coating layer ($i = 1$) and cantilever material ($i = 1$), $H(x - x_0)$ is the Heaviside step function, and z_0 is the neutral axis of the composite beam. The location of the neutral axis depends on the relative stiffness and size of each of the material sections [76]:

$$z_0 = \frac{E_2 d_2^2 - E_1 d_1^2}{2(E_1 d_1 + E_2 d_2)}. \quad (4.12)$$

The Heaviside function implies that the stress at x_0 only affects positions where $x > x_0$ because the cantilever is singlely clamped at the base. Now consider the bending moment caused at x by an infinitesimal thermal expansion at x_0 (Figure 4.1), because $\Delta T(x_0) \approx \Delta T(x - x_0)$, we get:

$$dM(x;x_0) = M(x;x_0 + dx_0) - M(x;x_0) = c_{th} \Delta T(x_0) \delta(x - x_0) dx_0, \quad (4.13)$$

where

$$c_{th} = W[\alpha_2 E_2 d_2(\frac{d_2}{2} - z_0) - \alpha_1 E_1 d_1(\frac{d_1}{2} + z_0)].$$

Integrating the bending moment contribution from the whole cantilever gives:

$$M(x) = \int_{x_0} dM(x; x_0) = c_{th} \int_0^L \Delta T(x_0)\delta(x - x_0)dx_0. \tag{4.14}$$

Inserting this expression into Equation 3.34, the effective force of the nth mode due to bimorphic bending is:

$$F_{n,eff} = -\frac{c_{th}}{\phi_n(L)} \int_0^L \Delta T(x_0)dx_0 \int_0^L \phi_n(x)\frac{d^2}{dx^2}\delta(x - x_0)dx, \tag{4.15}$$

and using the properties of the Delta function, the mode-dependent effective force leads to:

$$F_{n,eff} = -\frac{c_{th}}{2} \int_0^L \Delta T(x_0)\frac{d^2\phi_n(x_0)}{dx_0^2}dx_0. \tag{4.16}$$

Figure 4.5 shows the effective photothermal force due to the bimetallic effect of the 1st eigenmode and compares it to that of the radiation pressure. (Definition of the mode effective force can be found in Chapter 3.) The photothermal effective force for a given vibration mode is maximized when the cantilever is optically excited at regions where maxima of the curvature of the beam vibration eigenmodes lie (Figure 3.4). For the first eigenmode, the maxima of the curvature is at the base of the cantilever, but the peak is slightly away from the base. That is because as the laser move closer to the base (which acts as a heat sink), heat is more quickly

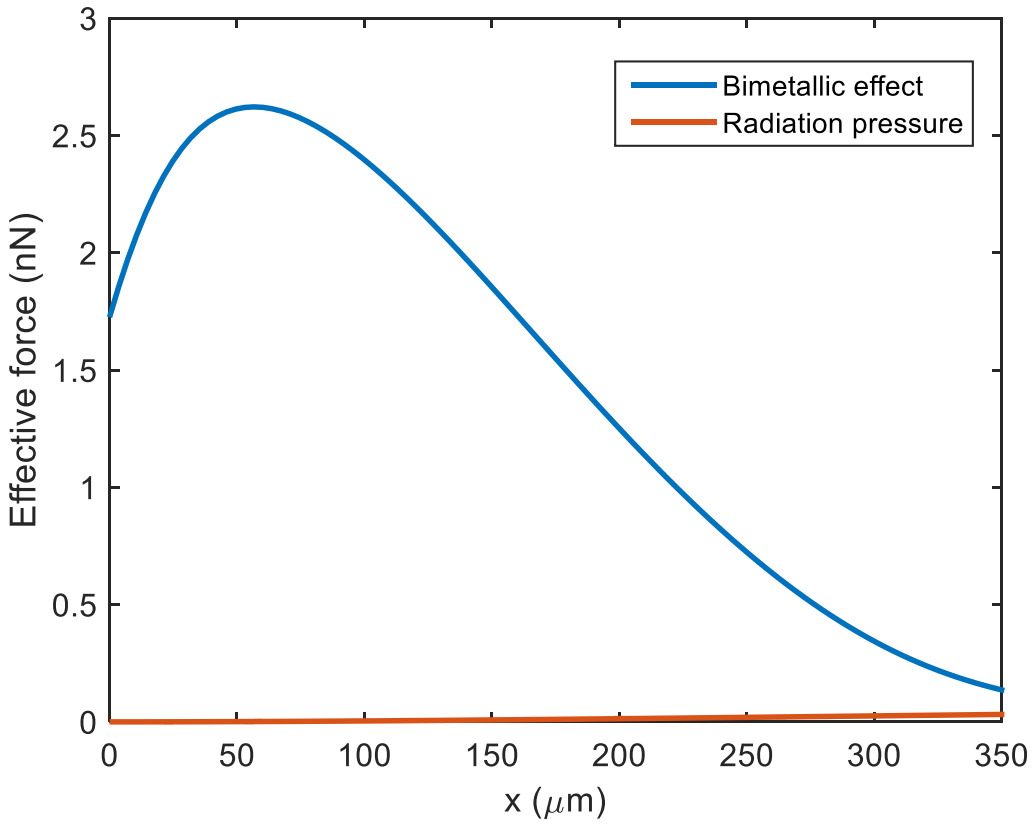

Figure 4.5: Calculation of the first-eigenmode effective force of bimetallic effect (blue) and radiation pressure (red).

dissipated and the temperature increase lessens. Also, the laser has a spot size of 10 μm in the calculation, so as it move close to the base, the actual power falling on the cantilever is reduced. Through the comparison with radiation pressure, it is clearly to see that the bimetallic effect dominates over the radiation pressure by at least an order of magnitude, and it is not possible to measure the radiation pressure with a coated cantilever. In our experiments, we observed an even stronger bimetallic effect, about 2-3 orders of magnitude larger than the radiation pressure.

4.3 Temperature and carrier density gradient induced bending

The periodic generation of excess carriers in semiconductors produce heat due to carrier thermalization and recombination processes. The generated heat can produce thermal-elastic (TE) strain as shown in Equation 4.1. Besides that, the photogenerated plasma (excess carriers) can also produce electronic strain, often referred to as electronic deformation (ED). It is linearly proportional to the excess carrier density

$$\varepsilon^{ED} = d_n \Delta n, \tag{4.17}$$

where d_n is the coefficient of electronic elastic deformation and Δn is the excess carrier density [73]. Because d_n is negative in silicon and some other materials, this effect is also referred to as photo-striction.

For uncoated cantilevers made of a semiconductor (*e.g.* silicon), in principle, a pure temperature increase will not generate a bending moment, nor will the temperature gradient in the longitudinal direction. However, a gradient of excess carrier

density and temperature in the thickness direction (z-axis) could lead to a bending moment. In this section, we first calculate the carrier density distribution in z-axis and its effective force. Then we calculate the temperature distribution in z-axis and its effective force because the heat generation depends on the excess carrier densities.

4.3.1 Electronic elastic bending from carrier density gradient

In order to calculate the electronic strain induced bending, we first need to solve the excess carrier density distribution upon illumination. This is a two-dimensional (2D) diffusion problem with carrier generation inside the cantilever. However, an equation-based simulation using finite element solver in Comsol shows that the carrier diffusion in x-axis is negligible in terms of this calculation because the Gaussian profile of the carrier distribution in x-axis is not much different from that of the input Gaussian heat generation profile. Therefore, the 2D carrier diffusion problem can be reduced to a 1D diffusion problem. Assume the input light intensity is in the form of $I(x,t) = Re[I_0(x)e^{-i\omega t}]$. The excess carrier density is $\Delta n(x,z,t) = Re[\Delta n(x,z)e^{-i\omega t}]$. The excess carrier density distribution in z-axis can be determined by the 1D carrier diffusion equation [73]:

$$\frac{\partial \Delta n(x,z,t)}{\partial t} = D_n \frac{\partial^2 \Delta n(x,z,t)}{\partial z^2} - \frac{\Delta n(x,z,t)}{\tau} + G(x,z,t), \tag{4.18}$$

where D_n is the diffusivity of electrons in Si, τ is the bulk recombination life time of Si and $G(x,z,t)$ is the carrier generation rate within the Si cantilever. Substi-

tuting with the harmonic form of the excess carrier density, it becomes an ordinary differential equation:

$$\frac{\partial \Delta n(x,z)}{\partial z^2} - \frac{1+i\omega\tau}{D_n\tau}\Delta n(x,z) = -\frac{G(x,z)}{D_n}. \tag{4.19}$$

If we assume that the light intensity decrease exponentially inside the thin film, $I(x,z) = I_0(x)e^{-\alpha z}$ and that the quantum efficiency of carrier generation is 1, then the generation rate is:

$$G(x,z) = -\frac{A}{h\nu}\frac{\partial I(x,z)}{\partial z} = \frac{AI_0(x)}{h\nu}\alpha e^{-\alpha z}, \tag{4.20}$$

where A is the absorption coefficient (ratio of the total power absorbed). If we consider uniform illumination along the y-axis (width) and a Gaussian distribution along the x-axis (longitudinal), we get:

$$I_0(x) = \frac{P_0}{\sqrt{\pi}\sigma_x W}e^{-(x-x_0)^2/\sigma_x^2}, \tag{4.21}$$

where P_0 is the total incident power, x_0 is the excitation position, σ_x is the radius of the laser spot size, and W is the width of the cantilever. Letting $L_n(\omega) \equiv \sqrt{\frac{D_n\tau}{1+i\omega\tau}}$, Equation 4.19 becomes:

$$[\frac{\partial^2}{\partial^2 z} - \frac{1}{L_n(\omega)}]\Delta n(x,z) = \frac{AI_0(x)}{D_n h\nu}\alpha e^{-\alpha z}. \tag{4.22}$$

Solutions to this equation have the form:

$$\Delta n(x,z) = A_+ e^{z/L_n} + A_- e^{-z/L_n} + A_\alpha e^{-\alpha z}, \tag{4.23}$$

where A_+, A_- and A_α are constants need to be determined. Inserting this ansatz into Equation 4.22, we get:

$$A_\alpha = -\frac{AI_0(x)}{h\nu}\frac{\delta}{1-\delta^2}\frac{L_n}{D_n},$$

where $\delta \equiv \alpha L_n$. By applying the boundary conditions:

$$D_n \frac{\partial \Delta n}{\partial z}|_{z=0} = s_1 \Delta n(x,0), \tag{4.24}$$

and

$$D_n \frac{\partial \Delta n}{\partial z}|_{z=h} = -s_2 \Delta n(x,h), \tag{4.25}$$

where s_1 and s_2 are surface recombination velocities of the top and bottom surfaces of the cantilever, we get an matrix equation for A_+ and A_-:

$$\begin{bmatrix} 1-\sigma_1 & 1+\sigma_1 \\ (1+\sigma_2)e^{h/L_n} & (1-\sigma_2)e^{-h/L_n} \end{bmatrix} \begin{bmatrix} A_+ \\ A_- \end{bmatrix} = \begin{bmatrix} -(1+\sigma_1\delta) \\ -(1-\sigma_2\delta)e^{-\alpha h} \end{bmatrix} A_\alpha \tag{4.26}$$

where $\sigma_i = \frac{D_n}{s_i L_n}$, for $i = 1, 2$. The solutions to above matrix equation are:

$$A_+ = [(1+\sigma_1)(1-\delta\sigma_2)e^{-\alpha h} - (1-\sigma_2)(1+\delta\sigma_1)e^{-h/L_n}]\frac{A_\alpha}{A_L} \tag{4.27}$$

and

$$A_{-} = -[(1-\sigma_1)(1-\delta\sigma_2)e^{-\alpha h} - (1+\sigma_2)(1+\delta\sigma_1)e^{-h/L_n}]\frac{A_\alpha}{A_L}, \tag{4.28}$$

where

$$A_L = (1-\sigma_1)(1-\sigma_2)e^{-h/L_n} - (1+\sigma_1)(1+\sigma_2)e^{h/L_n}. \tag{4.29}$$

To estimate and simulate this effect, we assume an incident laser power of 5 mW, a laser spot of is 5 μm, a cantilever thickness is 1 μm. Figure 4.6 shows the solution of the excess carrier density distribution at a 10 kHz excitation frequency. The surface recombination velocities play a significant role in the carrier density distribution as well as the frequency response. The difference of the photogenerated carrier density along the z-axis is quite small, but as long as there is difference, it will generates thermal moment.

The carrier density distribution transforms to a bending moment through photostriction effect and stress-strain relation. The differential bending moment at x due to a carrier gradient at x' is

$$dM(x;x') = EWd_n \int_0^h \Delta n(z,x')(z-h_n)dz\delta(x-x')dx', \tag{4.30}$$

where E is the Young's modulus of silicon and h_n is the position of the cantilever's neutral axis. For a cantilever with rectangular cross section, the neutral axis is in

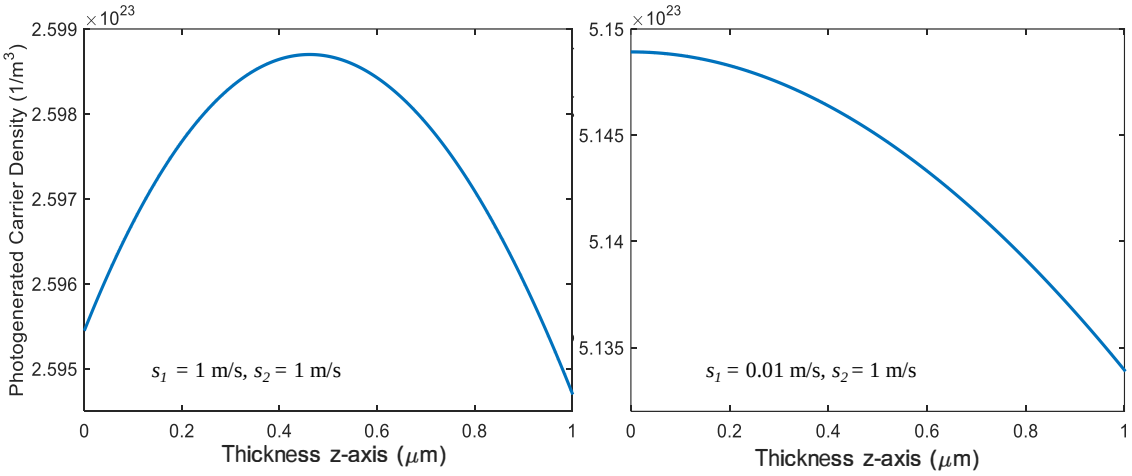

Figure 4.6: Magnitude of photogenerated carrier density along the thickness of a 1-μm-thick cantilever $\Delta n(x_0, z)$ at the center of laser spot ($x = x_0$). Two different combination of surface recombination rates are shown. s_1 is surface recombination rate at top surface ($z = 0$), and s_2 is surface recombination rate at bottom surface ($z = h$). Light intensity modulated at frequency of 10 kHz and The bulk recombination lifetime is set to 5×10^{-5} s

the middle ($h_n = h/2$). The total moment at x is

$$M(x) = \int_{x_0} dM(x; x') = EWd_n \int_0^h \Delta n(z, x)(z - h_n)dz. \tag{4.31}$$

Because we assume the light intensity has a 1D Gaussian distribution along the x-axis (Equation 4.21) and the carrier diffusion in x can be neglected, the bending moment at x when the laser excitation is at x_0 is given as

$$M(x; x_0) = EWd_n \int_0^h \Delta n(z, x_0) e^{\frac{(x-x_0)^2}{\sigma_x^2}} (z - h_n)dz. \tag{4.32}$$

To estimate the effect of electronic deformation, the effective force is calculated by inserting the bending moment into Equation 3.34. Given the same parameters as previous calculations and sweeping the excitation position, we get the position

dependent effective force from electronic deformation. The peak of the effective force is very close to the base of the cantilever as the laser spot is tight and no diffusion in x-axis. From the calculated phase, the effective force is out of phase with the radiation pressure (causing the cantilever to bend up instead of down when the laser is on) because of the negative coefficient d_n, which is how photo-striction gets its name.

Figure 4.8 shows the magnitude of the calculated effective force from electronic deformation compared with that of the radiation pressure. It shows that, except for laser excitation near the base, the effective force due to a carrier density gradient in the thickness is much smaller than the radiation pressure.

4.3.2 Thermal-elastic bending from a temperature gradient

The temperature gradient distribution can be determined by solving the heat diffusion equation along the z-axis, assuming the heat diffusion along the x-axis has negligible contribution to the total bending moment, which is a reasonable assumption because in this it is the difference in temperature distribution along the thickness that generates the bending moment. The diffusion equation needs to be solved in different regions (air above the cantilever, within the cantilever and below the cantilever) with matched boundary conditions. The heat source within the cantilever has three sources: thermalization of excited carriers, bulk recombination, and surface recombination. Here we utilize the results derived in [71, 77] and use parameters from our experiment to see how this effect compares

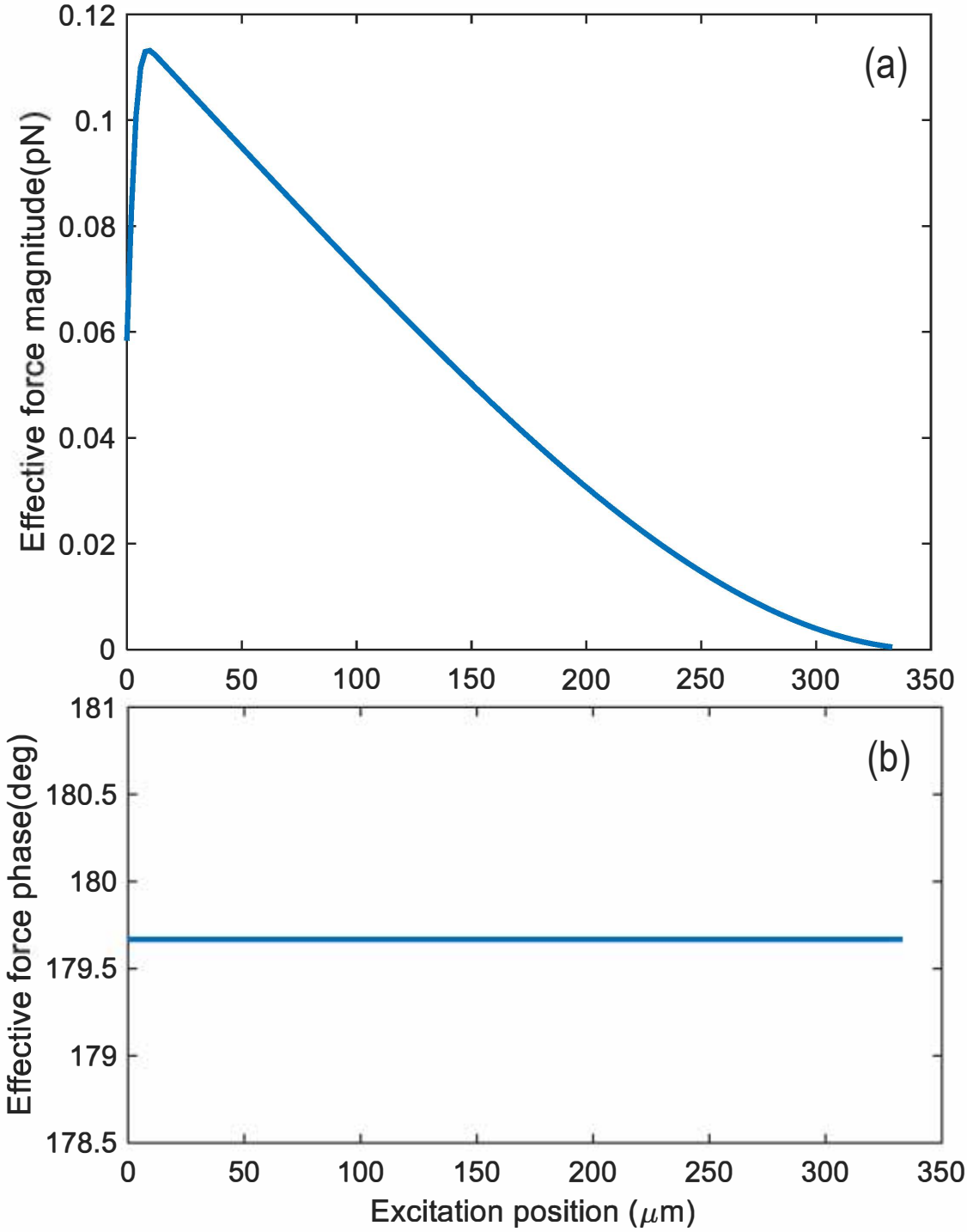

Figure 4.7: Effective force (a) magnitude and (b) phase of the fundamental mode due to electronic deformation. The incident power is 5 mW, laser sport radius 5 μm, absorption coefficient is 0.15, and excitation frequency 10 kHz, the top surface recombination rate 0.01 m/s, the bottom surface recombination rate 1 m/s and the bulk recombination lifetime 5×10^{-5} s.

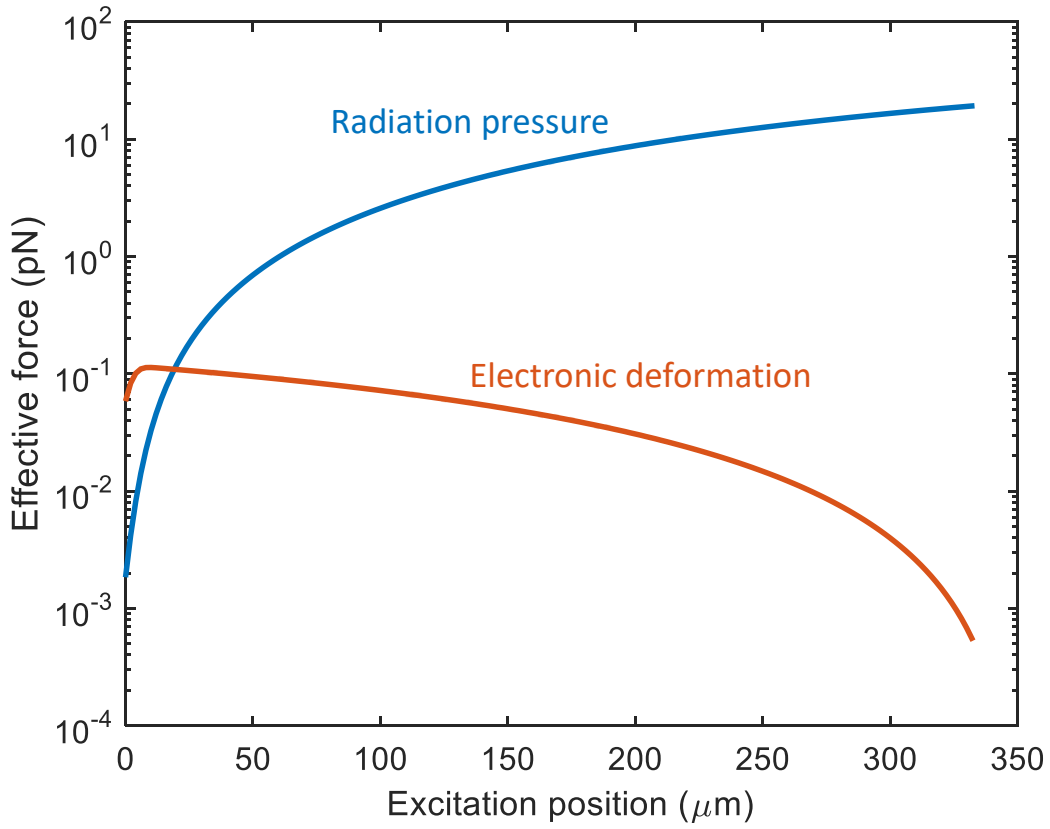

Figure 4.8: Comparison of the effective force of the fundamental mode due to radiation pressure and electronic deformation at different excitation positions along the cantilever.

with the radiation pressure. Following a similar procedure as the calculation of the electronic deformation, the temperature increase distribution along the z-axis is shown in Figure 4.9.

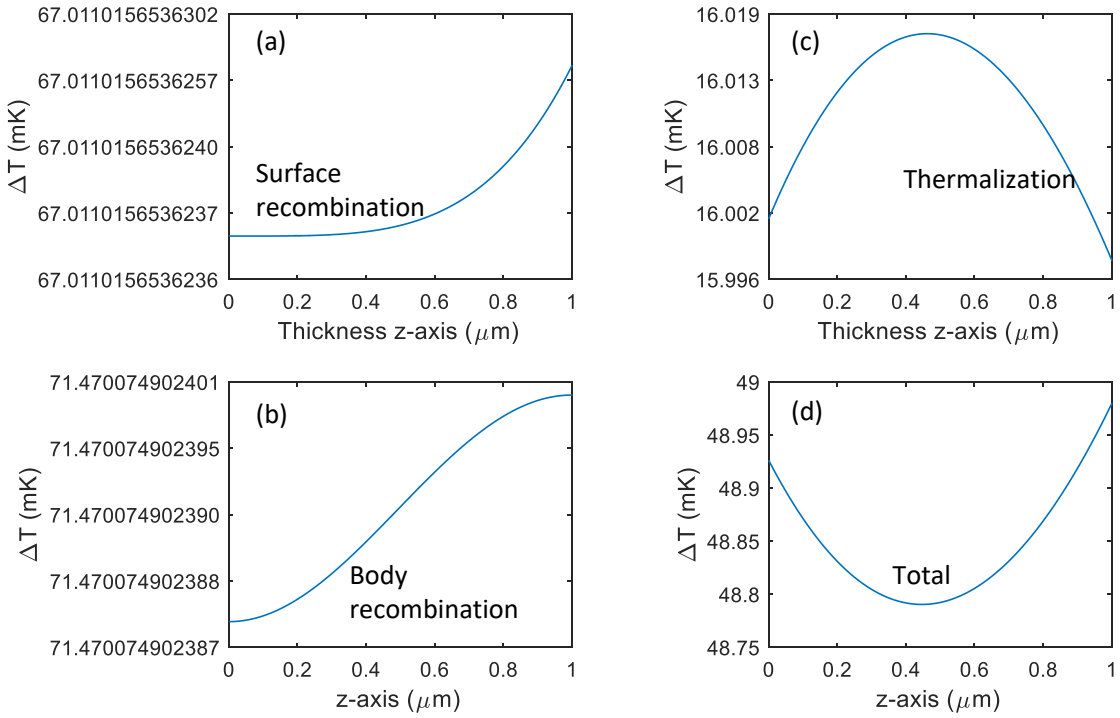

Figure 4.9: Magnitude of temperature increase distribution along the thickness of a 1-μm-thick cantilever $\Delta T(x_0, z)$ at the center of laser spot ($x = x_0$) at the center of laser excitation. Contributions from three heat sources are shown: (a) surface recombination, (b) body recombination, and (c) thermalization. (d) is the their sum. The incident power is 5 mW, laser sport radius 5 μm, absorption coefficient 0.15 and excitation frequency 10 kHz, the top surface recombination rate 0.01 m/s, the bottom surface recombination rate 1 m/s and the bulk recombination lifetime 5×10^{-5} s

The bending moment due to a temperature gradient along the z-axis when laser excitation is at x_0 is calculated by:

$$M(x; x_0) = EW\alpha \int_0^h \Delta T(z, x_0) e^{\frac{(x-x_0)^2}{\sigma_x^2}} (z - h_n) dz. \tag{4.33}$$

The bending moment is then inserted into Equation 3.34 to calculate the effective force, shown in Figure 4.10. The thermal-elastic deformation from the temperature gradient in thickness is even smaller than the electronic deformation, and is much smaller than the radiation pressure.

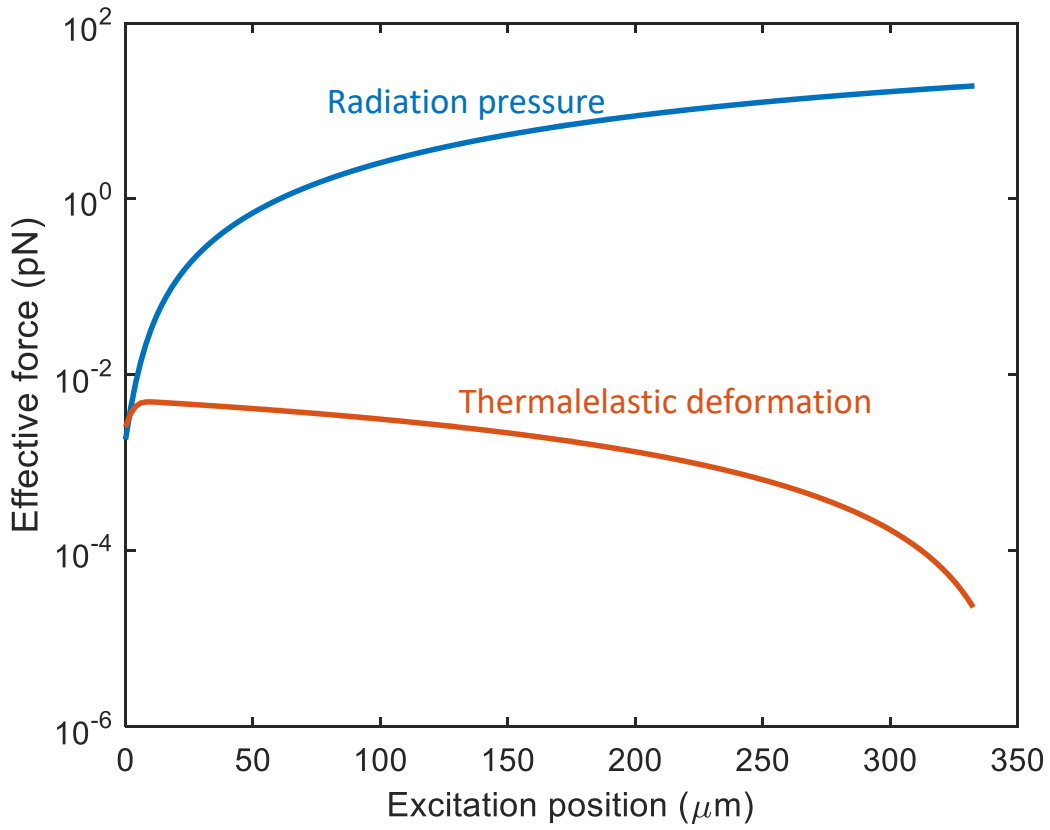

Figure 4.10: Comparison of the effective force of the fundamental mode due to radiation pressure and thermal-elastic deformation at different excitation positions along the cantilever.

4.3.3 Conclusion from electronic and thermal calculations

The above calculations show that neither the electronic deformation due to excess carrier density gradient along the z-axis nor the thermal-elastic deformation

due to temperature gradient along the z-axis can explain the photothermal effects we observed in the experiment. One possible explanation is that although the cantilever is uncoated, there could be a material difference between the cantilever and the chip, causing bimorphic effect at the base. For example, we confirmed with the manufacture of the silicon nitride cantilever that the silicon nitride is deposited on top of a thin layer of silica, which is on top of the silicon chip. It is also very common for silicon cantilevers to be fabricated out of silicon-on-insulator (SOI) wafers, where the cantilever is on top of silicon dioxide on top of silicon. A more delicate study of the heat transfer process coupled with stress and strain within micromechanical/nanomechanical structures is needed to find the root cause of the thermal effects observed experimentally in uncoated cantilever. A detailed finite element method (FEM) calculation as in [54] would be very helpful in the future.

4.4 Polarization dependent photothermal bending based on nanophotonic gratings

Because the photothermal bimetallic bending is the predominant bending mechanism for coated cantilevers, which are frequently used in atomic force microscopy (AFM) to boost the reflectivity and thus the detection sensitivity, people have started to utilize photothermal excitation to replace the traditional piezoelectric excitation. It is especially useful for AFM imaging in liquids when the damping is high and the piezoelectric excitation suffers from the notorious "forest of peaks" problem [78]. Efficiency of the photothermal excitation is important in these appli-

cations because we would like to achieve the largest amplitude of oscillation with the smallest laser power. So here we proposed the idea of using nanophotonic gratings to achieve a polarization dependent photothermal bending that can increase the photothermal excitation efficiency when the laser polarization is set to one particular polarization.

The cantilever used for this experiment is the same as in the previous section, 1 μm thick Si with a 30 nm Al coating. Figure 4.11(a) shows a schematics of the design where a small grating area is to be fabricated near the base of the cantilever to maximize the photothermal effect. Because the bimetallic bending is directly related to the absorption, a full-wave finite difference time domain (FDTD) simulation is conducted for the grating structure under TE and TM polarizations to calculate the absorption. The grating period and duty cycle (the ratio of the width of the Al to the width of the period) are varied to find the parameters that maximize the absorption difference between the TE and TM polarization. The optimal parameters are a period of 450 nm and an Al width of 240 nm. The grating structure is fabricated by Dr. Henri Lezec's group at NIST using focused ion beam (Figure 4.12).

The experimental setup for measuring the polarization dependent photothermal bending is similar to Figure 2.1 but with an extra half-wave plate between the laser and the hot mirror. The half-wave plate can be rotated to change the polarization of light hitting the cantilever. The photothermal cantilever tuning curve (frequency sweep) is recorded at each polarization and fitted to the SHO model as in [60]. Figure 4.13 shows the fitted off-resonant amplitude A_0 as a function of polarization angle at two excitation positions. It can clearly be seen that when the laser

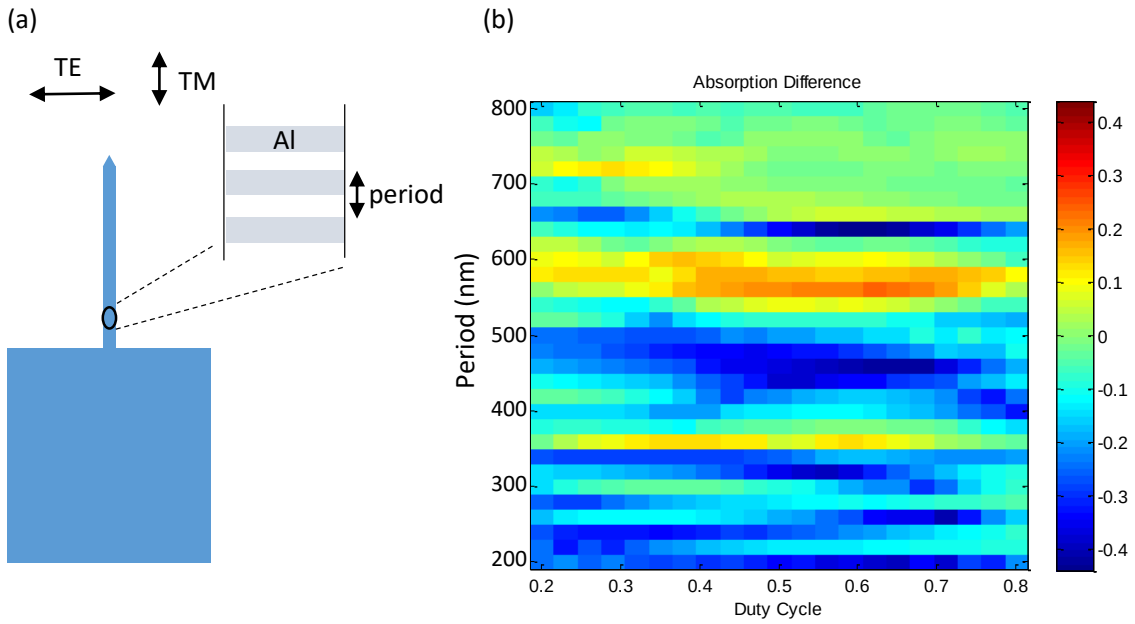

Figure 4.11: (a) Schematic illustration of fabricating grating structures near the base of the cantilever and the definition of TE and TM polarization. (b) Absorption difference (TE minus TM polarization) at 660 nm illumination given different combination of grating period and duty cycles.

is focused on the grating area, the cantilever oscillation amplitude changes when the light polarization is varied. The photothermal bending under TM polarization is more than three times larger than under TE polarization. The Al grating structures enhanced the absorption for TM polarization at 660 nm, providing a larger photothermal excitation efficiency compared with the planar Al coating. Thus, this structure operates as a polarization dependent optomechanical transducer.

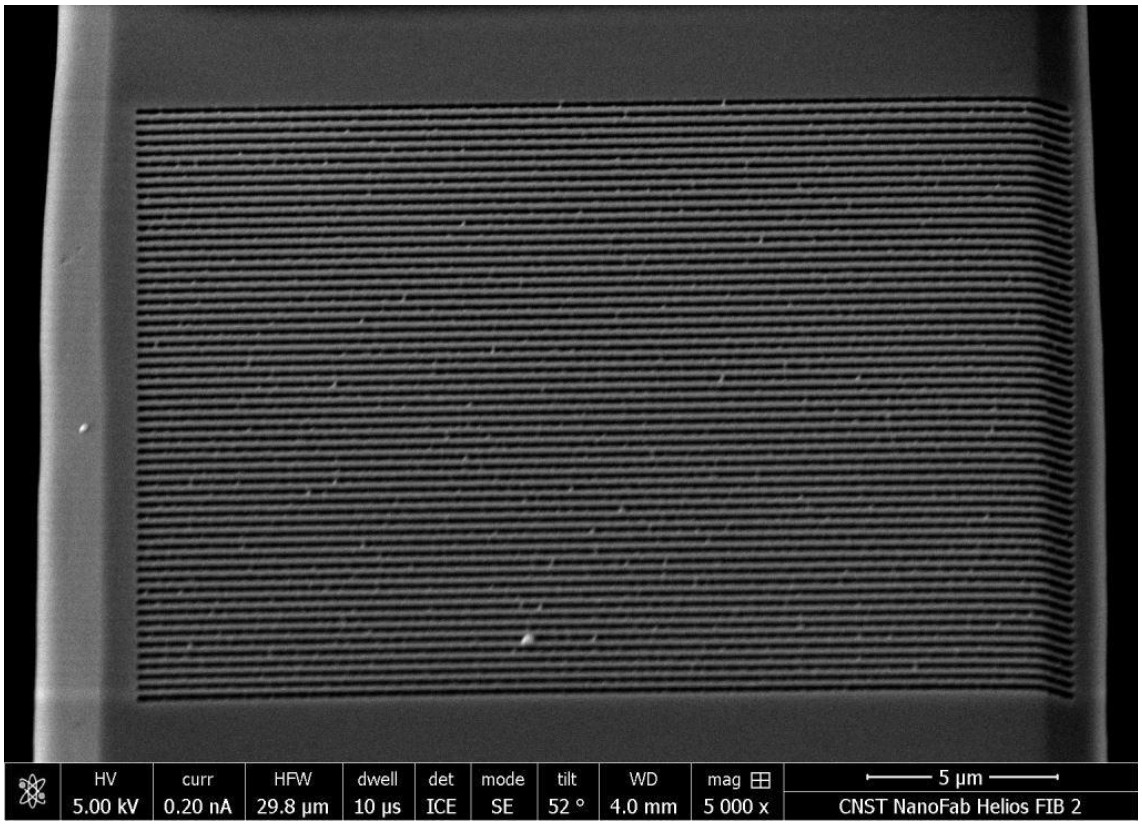

Figure 4.12: SEM image of the grating structures fabricated by focused ion beam. The camera is tilted at an angle of 52°, the actual grating area is a 35 μm $\times$ 35 μm square.

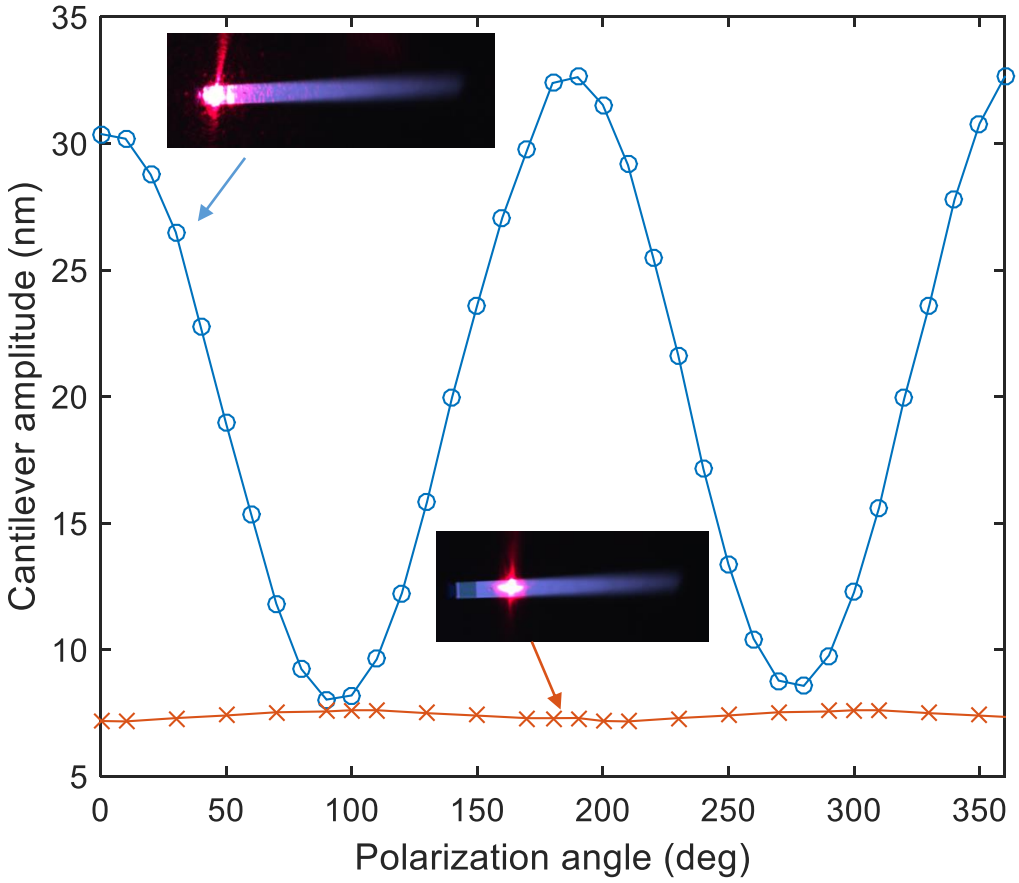

Figure 4.13: Measured cantilever amplitudes (A_0) with changing laser polarization at two different excitation positions. Blue: laser is focused on the grating area. Red: laser is focused on planar Al coating area. 0° corresponds to the TM polarization and 90° corresponds to the TE polarization.

Chapter 5: Switchable optical materials for attitude control

5.1 Attitude control of a solar sail

Spacecraft attitude is the angular orientation of a spacecraft body vector with respect to an external reference frame [79]. Attitude control system (ACS) is critical to stabilize the spacecraft and make changes of the spacecraft's orientation when necessary [80]. Although solar sails alleviate the need for chemical propellant, attitude control subsystems in current solar sail missions at NASA, *e.g.* NEA Scout and Lunar Flashlight missions, are still performed using traditional propellant ejection gas system. The use of the gas thruster has limited the lifetime of the mission. A propellant-less attitude control mechanism would reduce weight and cost while improving performance and lifetime for solar sail missions. One way to achieve attitude control is to incorporate materials whose optical properties can be altered electronically, so that radiation pressure on different parts of a solar sail can be controlled individually and actively during operation. The IKAROS (Interplanetary Kite-craft Accelerated by Radiation Of the Sun) mission from the Japan Aerospace eXploration Agency (JAXA) successfully demonstrated the use of a reflective control device (RCD) to achieve limited attitude control of a spinning-type solar sail [81]. The ideal material for attitude control should have significant momentum transfer

difference between on and off states over a broad range of solar spectrum.

5.2 Overview of switchable optical materials

In order to achieve attitude control of a solar sail without moving parts, materials whose optical properties can be switched under external stimuli need to be applied. We researched different types of switchable optical materials such as electrochromic materials, phase change materials and tunable metamaterials. Here we discuss briefly their principles and the pros and cons of applying them in the solar sail application.

5.2.1 Electrochromic materials

Electrochromic materials change color due to the difference in absorption spectrum before and after an electron-transfer (redox) process. Many transition metal oxides are electrochromic, such as tungsten, molybdenum, iridium, nickel, etc. They are the most studied and popular electrochromic materials for several good reasons. First of all, both of their redox states are solid, making it possible to use them as thin films on electrodes. Secondly, once their redox state has been switched, no further charge injection is needed to retain the new electrochromic state, which is quite efficient from a power consumption perspective. Last but not the least, they provide large contrast in color between the two states. Current commercial applications of electrochromic materials mainly focus on smart windows for automobiles, buildings, and aircrafts. The most commonly used electrochromic material

is tungsten trioxide. The coloration process is usually described in terms of the double-charge-injection model [82]: $WO_3 + xA^+ + + xe^- = A_xWO_3$, where A^+ represents small cations like H^+ and Li^+. WO_3 is colorless while A_xWO_3 is deep blue. The WO_3 thin film can be fabricated using RF sputtering of a tungsten target under oxygen flow. To test whether we get tungsten trioxide, we colored the WO_3 film by touching an indium wire to the surface covered by dilute H_2SO_4 acting as an acid electrolyte [83] (Figure 5.1). The optical transmission spectrum of the film before and after coloration is measured using an optical microscope and spectrometer (Figure 5.2). After coloration, the transmission above 550 nm decreases much more than the spectral region below 550 nm, indicating that the strong absorption of longer wavelengths after coloration results in the film's deep blue appearance.

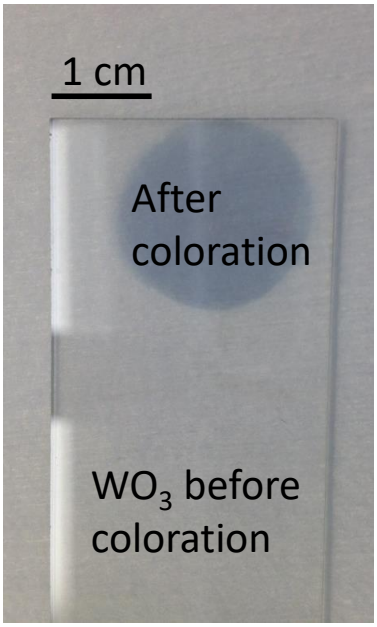

Figure 5.1: Coloration of the WO_3 thin film sputtered on glass slide using chemical H^+ injection.

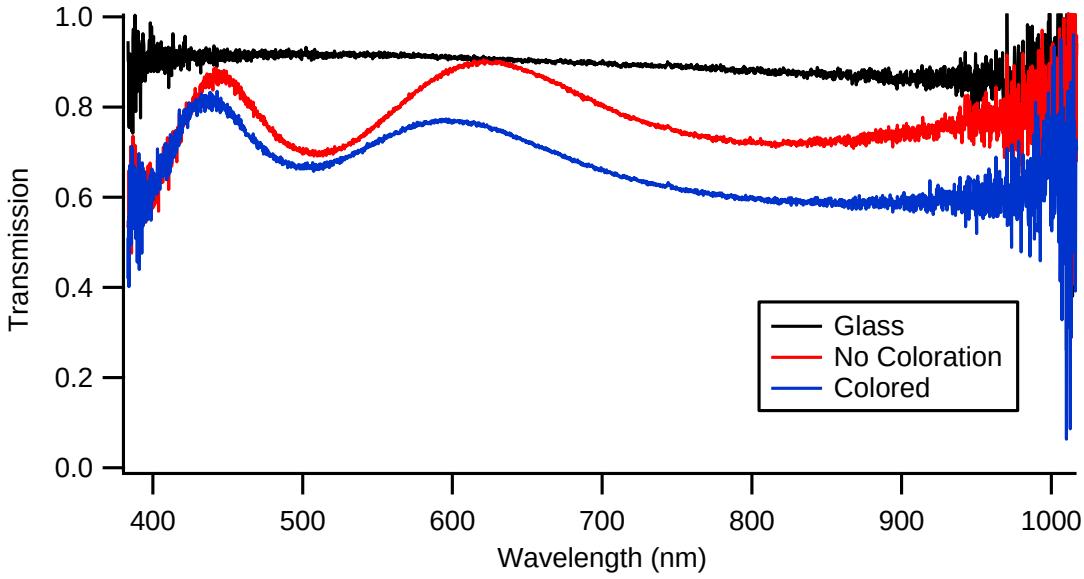

Figure 5.2: Optical transmission spectrum of a WO_3 film before and after coloration. The coloration process reduces long wavelength transmission.

It is worth noting that WO_3 is also a photochromic material, meaning that it will change color under UV illumination, a "non-contact" way of changing color. However, the wavelength of incident light needs to be smaller than 380 nm, and the efficiency of photochromic response is very low so that either a very high power light source is needed or the sample need to be exposed for a long period of time. In the lab, we achieved the coloration of WO_3 film by exposing it under high-power mercury lamp of several watts for 20 minutes, which is not a very practical coloration method.

In order to achieve electronically controlled coloration and the reverse bleaching, an electrochromic device (EMD) needs to be constructed to allow the flow of ions. The basic structure of an EMD is similar to a battery device, shown in Figure 5.3.

The advantages of an electrochromic device include: 1) it can achieve a rel-

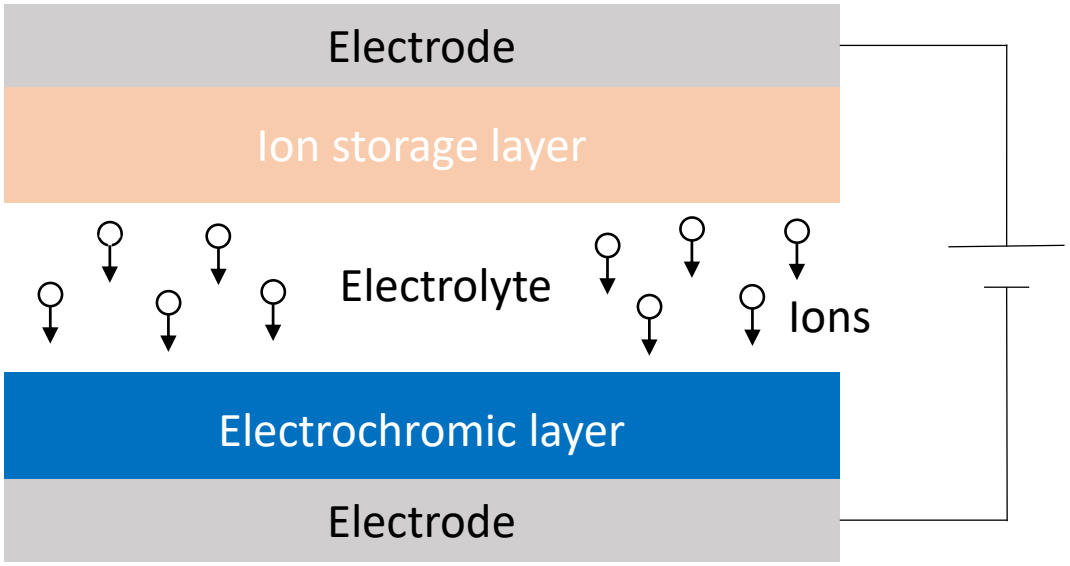

Figure 5.3: Schematic of the working principle of an electrochromic device. When a positive voltage is applied as shown in the figure, ions transport from the ion storage layer to the electrochromic material through the electrolyte, causing coloration.

atively large change in optical properties throughout visible spectrum under small applied voltages, and 2) once the state is changed,there is no need to apply a voltage to maintain the state. The main disadvantage of an electrochromic device is its slow switching speed, because the device operation is based on ion diffusion and transportation. The switching time also scales with the surface area, so the larger the area the slower the switching speed.

5.2.2 Thermochromic phase change materials

Thermochromic materials refer to materials that change color due to a change in temperature. Broadly speaking, thermochromic liquid crystals, thermochromic dyes and many inorganic compounds are all thermochromic materials [84]. Among

these, vanadium dioxide, VO_2, stands out and receives significant attention due to its reversible semiconductor-to-metallic phase transition at a relatively low transition temperature ($T_c \approx 68°C$). Although the phase change mainly refers to the change in electrical properties, it is also accompanied by a dramatic change in the optical properties, especially in the infrared regime, making it an appealing thin film thermochromic material. The transition temperature can be further lowered by doping the VO_2 with tungsten [85]. Besides temperature, the phase transition of VO_2 coatings can be controlled by other external parameters such as pressure, photo-excitation, photo-carrier injection into a VO_2 heterostructure, and electric field [86]. These properties make VO_2 a good candidate as a smart coating material for a number of applications such as smart windows [87], smart radiators [88] and switchable metamaterials [89].

VO_2 is also an attractive material for switchable solar sail applications, because unlike electrochromic materials that require building a bulky cell to achieve reversible change in color, tens of nanometers of a VO_2 thin film is all it needs, which can reduce the added mass of the solar sail. In order to predict and optimize the performance of thin film VO_2, we used the optical properties of VO_2 derived from the dispersion model provided in [90] to calculate the reflection and absorption coefficients. Then we define the weighted average fraction of momentum transfered to the solar sail across the AM0 spectrum, given by

$$f_p = \frac{\int [2R(\lambda) + A(\lambda)] S(\lambda) d\lambda}{\int S(\lambda) d\lambda}, \tag{5.1}$$

where $R(\lambda)$, $A(\lambda)$ and $S(\lambda)$ are reflection coefficient, absorption coefficient and AM0 solar irradiance at wavelength λ, respectively. The difference of f_p between the semiconductor phase (S) and the metallic phase (M) is our figure of merit, given by

$$\Delta f_p = |f_s - f_m|. \tag{5.2}$$

Here we considered two situations: VO_2 film on transmissive substrate(glass) and VO_2 film on a 100 nm Al coating (common in current solar sail designs). In the first situation, the optimal VO_2 thickiness is 30 nm, providing $\Delta f_p = 0.06$, shown in Figure 5.4. We can see that although the material has a large change in the optical properties for the infrared regime, the majority of the solar power lies below 1 μm, where the difference is small for VO_2. For the second situation (VO_2 on Al), the optimal VO_2 thickness is 25 nm, giving $\Delta f_p = 0.09$.

From the calculation we see that the momentum switchability of VO_2 film is not very good under the weighted solar spectrum in space. The film is too absorbing in the visible spectrum and does not provide much switchability in this regime where the peak of the solar spectrum lies. The other drawback is that VO_2 is difficult to deposit onto flexible substrates such as Kapton. The reason is that the film needs to be crystalline in order to demonstrate the phase transition behavior. Depositing on a sapphire substrate with high substrate temperature (500°C) is a typical way to make crystalline VO_2 because of the matched lattice constants [89]. Researchers have demonstrated that it is possible to get VO_2 deposited on Kapton, but with a obvious performance degradation [91].

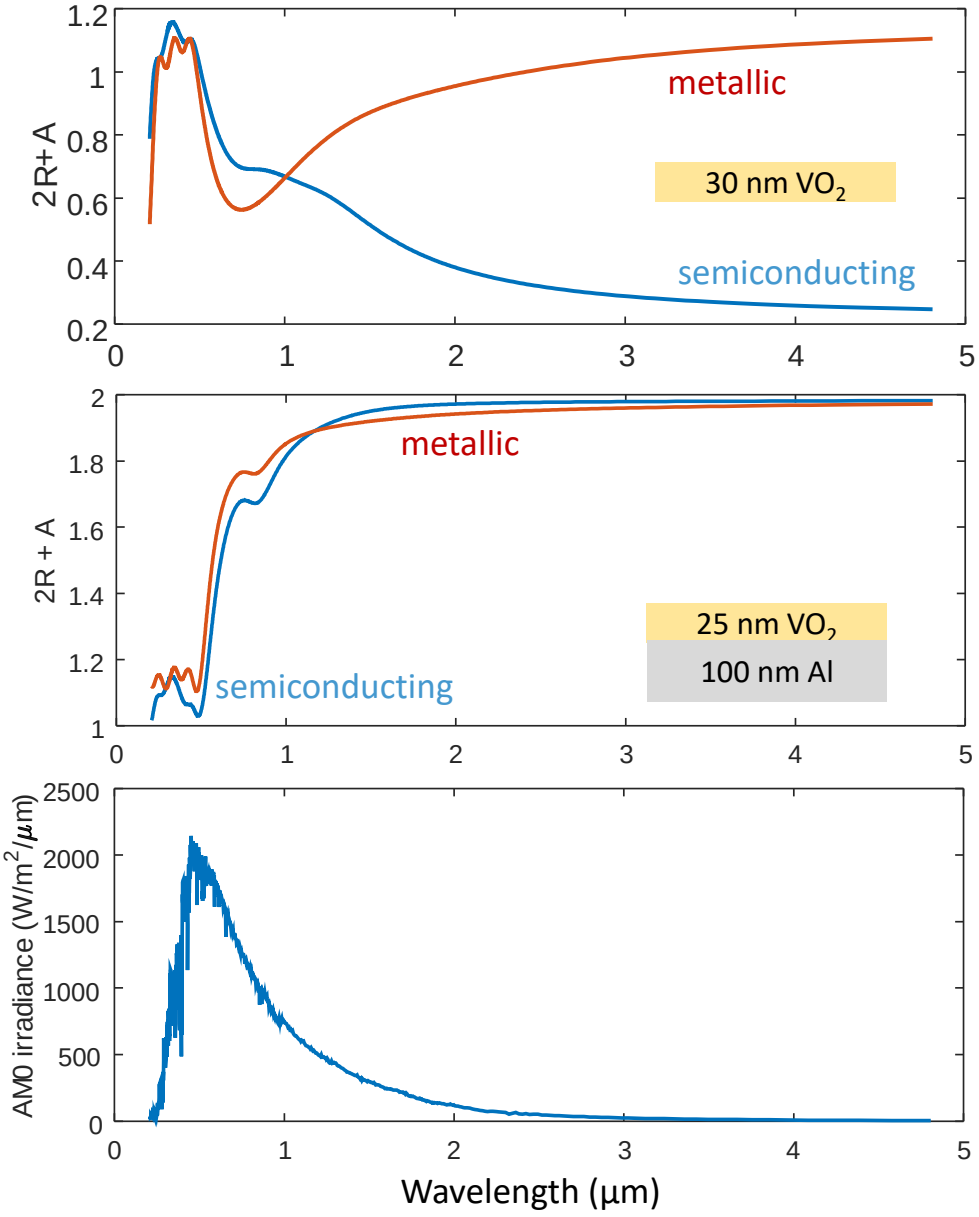

Figure 5.4: (a) Fraction of photon momentum transfered to the 30 nm VO_2 thin film. (b) Fraction of photon momentum transfered to the 25 nm VO_2 thin film on top of 100 nm Al film. (c) AM0 solar irradiance spectrum.

5.2.3 Switchable metamaterials

Metamaterials are artificially engineered media that are designed to have unique electromagnetic properties that do not exist in nature. Metamaterials are usually composed of 1D, 2D or 3D arrangements of individual elements, a.k.a "meta-atoms", whose dimensions are much smaller than the wavelength of the electromagnetic radiation [92]. One of the exotic behaviors that metamateriasl can achieve is a negative index of refraction, proposed by Veselago 50 years ago [93]. Over the last two decades, researchers have achieved a negative index of refraction over a variety of wavelength regimes [94–97]. More recently, many researchers have been focusing on metamaterials whose optical properties can be tuned by external means. This is appealing for a switchable solar sail because optical metamaterials are often made of metal thin films or nanostructures, making them very light-weight. However, the optical response of metamaterials is usually very narrow, so they are not going to provide much tunability averaged over the entire solar spectrum. For future laser propelled light-sails, on the other hand, metameterials could be extremely useful because it can be designed for specific wavelength.

Tunable metamaterials can either have a frequency shift or amplitude modulation of the resonant peak upon tuning. One way to tune the resonance is to change the physical size of the meta-atoms. Pryce *et al.* fabricated split-ring resonators on a PDMS substrate and achieved a 400 nm resonant frequency shift at a wavelength about 4 μm by mechanically stretching the substrate [98]. If the meta-atoms have no coupling, changing the physical distance between meta-atoms

results in a modulation of the amplitude of the resonance, but if the meta-atoms are strongly coupled, doing so will change both the amplitude and the resonance frequency. Ou *et al.* fabricated plasmonic metamaterials on MEMS structures such as beams and comb-drive structures, which can be deformed easily by photothermal or electrostatic actuation [99, 100]. They achieved up to 50% resonance amplitude modulation in the near-infrared regime (1 μm $\sim$ 2 μm).

For optical metamaterials, the resonance wavelength can also be tuned by changing the refractive index of the surrounding materials. Generally speaking, changing the real part of the refractive index will shift the resonant wavelength, while changing the imaginary part will affect the amplitude of the resonance and quality factor. Dicken *et al.* demonstrated temperature-tuned metamaterials in the near-IR range based on metal-to-insulator phase transition of vanadium dioxide. The resonance frequency can be tuned by about 100 nm at the wavelength around 2.5 μm [89]. Driscoll *et al.* also utilized the tunability of vanadium dioxide to obtain a memory metamaterial whose response shows hysteresis during heating and cooling [101]. Another popular switchable medium is a liquid crystal (LC). Due to their optical birefringence, different orientation of LCs under varying electric field will provide different effective refractive indices. Xiao *et al.* changed the magnetic response of metallic nanostrips from 650 nm to 632 nm by heating the liquid crystal from 20°C to 50°C [102]. In the terahertz regime, Shrekenhamer *et al.* achieved electrical modulation of the absorption of a metamaterial immersed in a LC by 30% at 2.62 THz. The absorption peak also changed over 4% compared to the center frequency [103].

For microwave or terahertz metamaterials, the meta-atoms can often be mapped to an equivalent lumped RLC circuit. The effective resistance can be altered by either electrical carrier injection [104] or photoexcited carrier injection [105]. A novel approach that generates large tunability in a meta-atom's response in the microwave regime (more than 100% in frequency) was recently reported, which was achieved by tuning the effective inductance using radio frequency superconducting quantum interference device (SQUID) [106–108].

5.2.4 Summary

The switchable materials covered in this chapter are by no means a complete list. For most cases, choosing the right switchable material is a trade-off between it being light weight and tunable. However, it is very hard to achieve switchability across a broad wavelength range. In the next chapter, we will be looking at a scattering type of switchable material, polymer dispersed liquid crystal, that shows great promise for a switchable solar sail material.

Chapter 6: Polymer dispersed liquid crystals (PDLCs)

6.1 Background and motivation

The concept of radiation pressure for space propulsion has a long history in both popular culture and as a next generation space technology [31, 32]. Most space missions are limited by the amount of chemical propellant carried on board; however, as an alternative, solar sails use solar radiation pressure as propulsion and offer an opportunity for propellant-free space travel, enabling long-term and long-distance missions that are impossible with traditional methods. Although solar sail propulsion alleviates the need to carry chemical fuel, attitude control and steering are still performed using traditional methods involving reaction wheels and propellant ejection. A propellant-less attitude control mechanism would reduce weight and cost while improving performance and lifetime for solar sail missions. One way to achieve attitude control is to incorporate materials whose optical properties can be altered electronically, so that radiation pressure on different parts of a solar sail can be controlled individually and actively during operation. The IKAROS (Interplanetary Kite-craft Accelerated by Radiation Of the Sun) mission from the Japan Aerospace eXploration Agency (JAXA) successfully demonstrated the use of a reflective control device (RCD) to achieve limited attitude control of a spinning-

type solar sail [81]. The ideal material for attitude control should have significant momentum transfer difference between on and off states over a broad range of solar spectrum.

For the past few decades, liquid crystal devices have been used in numerous light control applications [109–111]. Among those, polymer dispersed liquid crystal (PDLC) films stand out due to their ability to be switched from an opaque to a transparent state with the applied external electric field without the need for polarizers. Since its discovery [112], researchers have extensively explored the potential applications of PDLCs in the areas of flat panel displays [113], smart windows [114, 115] microlens [116], etcetera. PDLC films consist of liquid crystal microdroplets dispersed in a polymer matrix. The liquid crystal droplets are optically birefringent with ordinary refractive index n_o and extraordinary refractive index n_e, while the polymer is an optically isotropic material with refractive index n_p. In the absence of an applied electric field (off state), the optical axes of individual bipolar droplets align randomly, resulting in spatial variations of refractive indices across the film. Liquid crystal microdroplets whose refractive indices differ from polymer matrix strongly scatters light and the PDLC film appears hazy. When enough voltage is applied across the film (on state), the liquid crystal molecules, which have positive dielectric anisotropy, align their optical axes with the electric field so that light incident normal to the film experiences a refractive index n_o in the liquid crystal droplets. By choosing the appropriate liquid crystal and polymer so that n_o and n_p are equal, the film becomes highly transparent as a result of reduced light scattering in the on state [57]. Unlike traditional liquid crystal displays, which need polarizers

and waste half of the light in the bright state, PDLCs do not require polarizers, offering much higher optical/energy efficiency. PDLCs also have significant optical contrast between on and off states over a broad range of the solar spectrum and the ability to be fabricated on a flexible substrate, both of which make it an ideal material for solar sail attitude control.

In this chapter, we present a steerable solar sail concept based on a PDLC that switches between transparent and scattering states, enabling attitude control without mechanically moving parts or chemical propellant. Devices are fabricated and characterized (transmission, reflection, absorption and scattering) over the visible and near infrared range of solar spectrum (400 nm - 1100 nm) and are found to outperform previous designs by more than a factor of four in terms of over-all weighted momentum switchablility between on and off states. Devices require no power in the diffusely reflective state and dissipate less than 0.5 mW/cm^2 while in the on state, showing great potential as a low-power switching mechanism for solar sail attitude control.

Figure 6.1 shows an exemplary design of a solar sail incorporating PDLC devices. The main part of the solar sail is coated with highly reflective aluminum to provide maximum thrust from solar radiation pressure. PDLC devices are attached to the transparent edges to maximize the torque generated from the radiation pressure difference between on and off states. In Figure 6.1, PDLC devices on the left are in the off state and scatter into both the forward and backward directions, resulting in a larger radiation pressure than those on the right, which are in the transmissive on state.

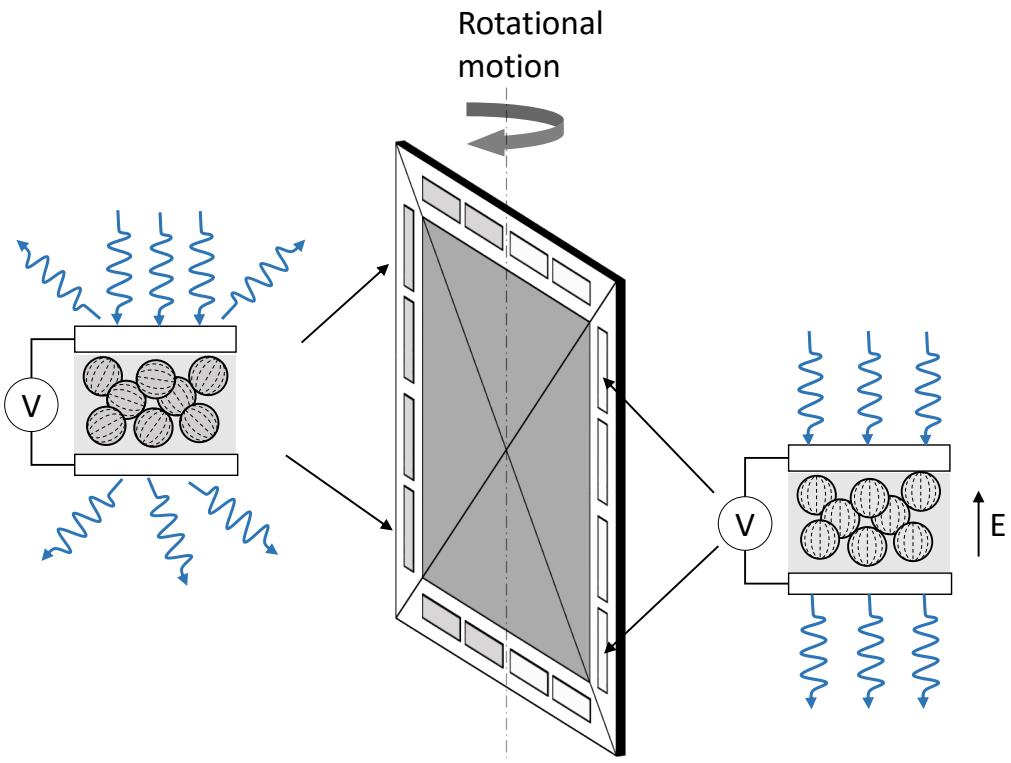

Figure 6.1: Schematic showing propellantless altitude control of a solar sail using PDLC devices. The optical properties of PDLC devices are controlled individually, which results in spatial-variation of the radiation pressure across the solar sail.

6.2 Device fabrication

To demonstrate the potential momentum switchablity of PDLCs, a 33 μm thick PDLC cell made from E7 nematic liquid crystal and Norland Optical Adhesive (NOA65) was prepared by the phase separation method. This thickness provides a good balance between high scattering in the off state and low turn-on voltage. The PDLC mixture consists of liquid crystal E7 (LC Matter Corp.) and photocurable polymer NOA65 (Norland Products) with 1:1 weight ratio. It is filled into an empty cell made with two ITO coated glass slides (Adafruit) with ITO coating facing inwards, which is separated by two polyester spacers (McMaster-Carr) on the edges. The PDLC mixture is then cured at room temperature for 1 minute with a UV lamp [117]. The two ITO layers are connected to copper wires and the electric field is applied through a custom-built high voltage AC source operating at 100 Hz. E7 has a nematic-isotropic transition temperature at 61°C and a positive dielectric anisotropy ($\Delta\epsilon = \epsilon_{\parallel} - \epsilon_{\perp}$) at 20°C, where and represent the parallel and perpendicular dielectric constants, respectively. The refractive indices of E7 at 20°C are given as $n_o = 1.5183$; $n_o = 1.7378$ ($\lambda = 632.8$ nm), leading to a birefringence of 0.2195. The melting point is 0°C [118].

6.3 Device characterization

A common method to determine the light scattering properties of a device is to measure its direct transmission with collection optics of a well-defined f-number (f/12

is commonly used, equivalent to a collection angle of 4.8°) [117]. A supercontinuum tunable laser (Fianium WhiteLase SC400UV) is used as the light source, and a homemade high-voltage driving circuit provides the square-wave AC voltages needed to turn the PDLC cell from opaque to transparent. The direct transmission is determined as a function of both wavelength and applied voltage as the device switches between the transmissive on state and the opaque off state (Figure 6.2a).

For a typical PDLC device, the direct transmission can be varied from 0% to $> 80\%$ upon switching. As the input wavelength increases from 400 nm to 750 nm, the direct transmission increases monotonically with wavelength. Both off state and on state transmission as well as turn-on voltage is greater at longer wavelengths, because the scattering cross sections at long wavelengths are smaller than those at short wavelengths under the same degree of droplet director alignment (same electric field) based on the anomalous diffraction model of scattering [119]. Despite some wavelength dependence, the significant optical contrast provided by the switchable scattering of PDLC is broadband in nature (Figure 6.2c).

In order to calculate the momentum transferred to the PDLC device, the angular distribution of light scattering of the PDLC cell under normal incidence is measured to determine the fraction of light scattered to different angles and their corresponding contribution to the total momentum transfer (Figure 6.3a). Scattering distribution measurements are made using a custom goniometer with sample illumination by a Fianium supercontinuum laser at normal incidence. The system rotates a photodiode about the sample and the photocurrent is measured by a Keithley 2400 Source Meter. The height of the photodiode is adjusted to the same height

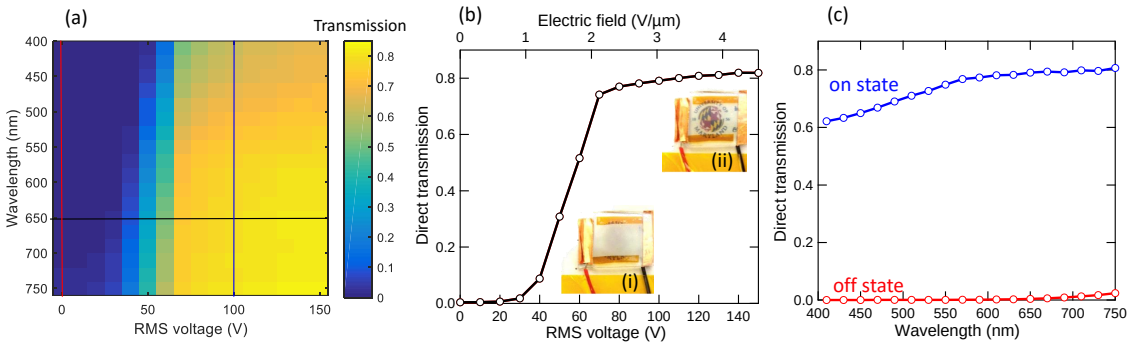

Figure 6.2: a) The direct transmission as a function of input wavelength and RMS (root mean square) voltage applied to the PDLC cell. b) The direct transmission as a function of RMS voltage at 650 nm, corresponding to the black line in a). The turn-on voltage V_{90} at this wavelength, where the transmission reaches 90% of the maximum transmission, is 70 V, and the corresponding turn-on field is 2.12 V/m. Insets: photos of the PDLC cell in the (i) off state and (ii) on state. c) The direct transmission across the visible on state (100 V) and off state (0 V), corresponding to the blue and red lines in a), respectively.

with the input laser to record the optical power along the equator of the scattering profile. The scattering is independent of azimuthal angle [110].

The angular distribution of the scattering under increasing applied voltage is shown in Figure 6.3b. In the off state (zero applied field), the scattering profile is very broad with a small amount of direct transmission ($< 0.2\%$ at 632.8 nm). The full-width-half-maximum (FWHM) of the diffusive scattering profile (after removing the direct transmission) is about 48°, larger than the 30° predicted by the anomalous diffraction approximation [110]. Multiple scattering causes the intensity to fall off much more slowly with scattering angle because the cell is quite thick compared with the size of liquid crystal microdroplets [120]. As the applied voltage increases, direct transmission and forward scattering gradually increase, and, after reaching the turn-on voltage (V_{90}), scattering reduces dramatically, and the film becomes transparent and is dominated by direct transmission. This sharp change in the scattering profile

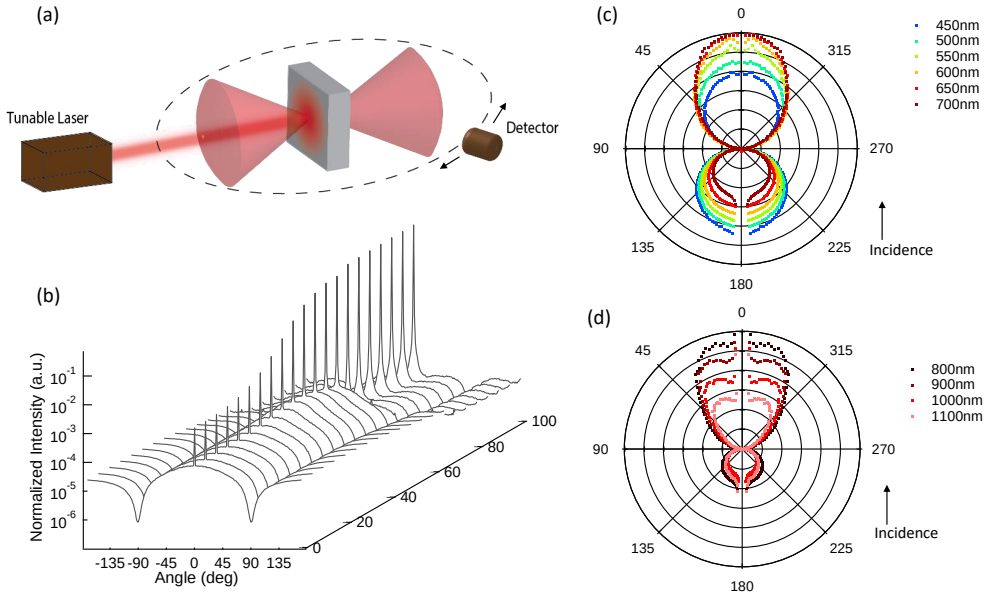

Figure 6.3: a) Experimental setup for measuring the angular distribution of light scattering for the PDLC cell. Input light is at normal incidence. b) A series of angular distribution measurements using 632.8 nm illumination with increasing voltages applied to the PDLC cell. Each curve shows the optical power measured at different scattering angles normalized to the incident laser power and is mirrored with respect to zero degrees (incident direction). Scattering distribution of the PDLC is shown in the off state under c) visible and d) infrared illumination.

originates from the strong nonlinear relationship between the applied voltage, degree of droplet director alignment, and scattering cross section [121].

The angular distributions as a function of wavelength are also measured because it is important for calculating the total momentum transfer under broadband solar illumination (Figure 6.3c and 6.3d). The scattering distribution of the PDLC in the off state shows strong wavelength dependence. As the wavelength increases, a greater fraction of scattered light goes in the forward direction rather than in the backward direction. The Lambertian scattering profile, which was used in a previous work [81], is a good approximation for scattering at short wavelengths but fails to describe the scattering distribution at longer wavelengths.

The total transmission and absorption of the PDLC in the on and off states are measured with an integrating sphere (Figure 6.4). The measurements are made using an integrating sphere (Labsphere RTC-060) illuminated by monochromatic light (5 nm bandwidth). Transmission is measured by placing the sample at an open port in the sphere and illuminating through this sample. Absorption measurements are similarly made but with the sample mounted in the center of the sphere. Measurements are made at a near-normal incidence of 13° for absorption measurements and 7° for transmission measurements, where the difference is due to the geometry of the setup. The light intensity in the sphere is detected with a photodiode. A small portion of the incident light beam is diverted to a reference photodiode to account for power variation of the light source. Second order diffuse absorption in the sample (light that is reflected or transmitted by the sample which then scatters and is re-directed toward the sample) is accounted for with a diffuse illumination measure-

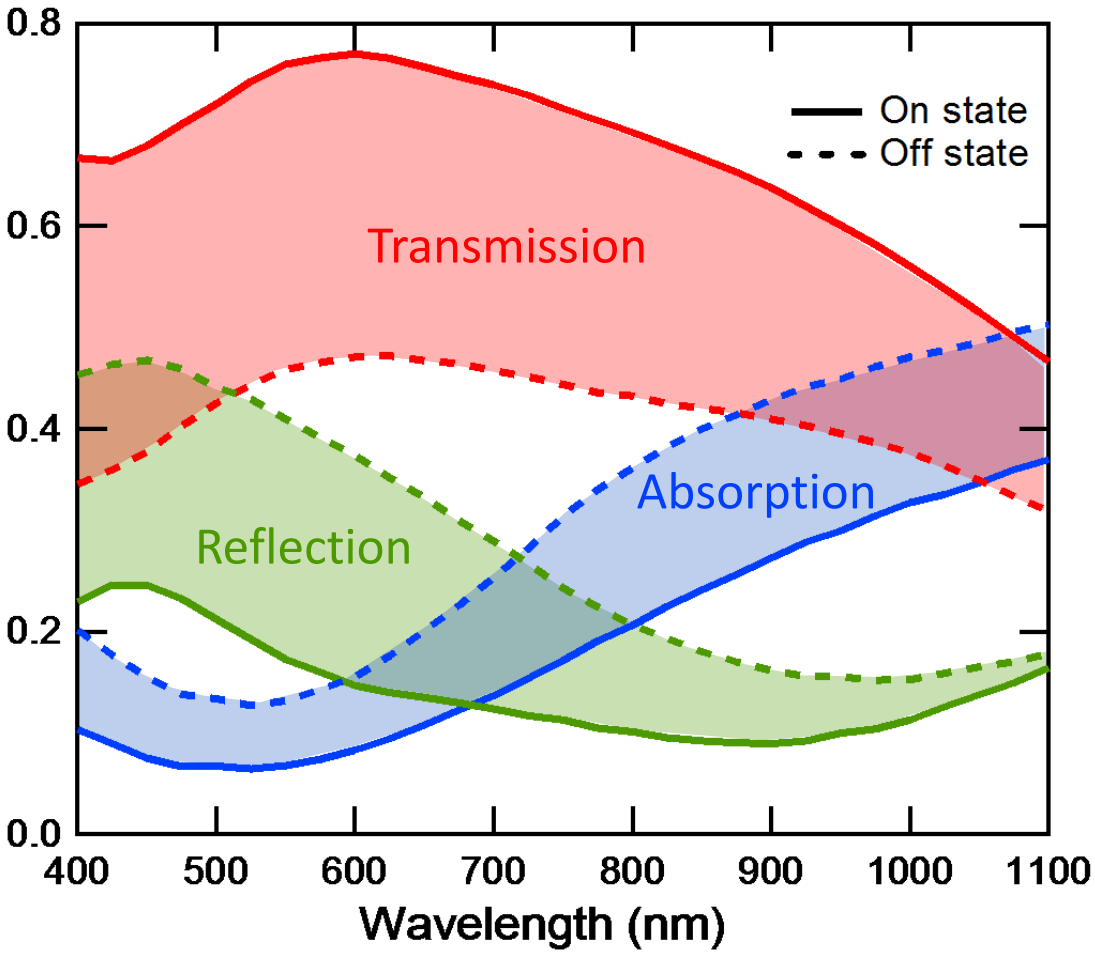

Figure 6.4: Total transmission, absorption, and reflection of the PDLC cell in the on and off states under near normal incidence measured with an integrating sphere.

ment. The signal to noise ratio is enhanced using a chopper and lock-in amplifier configuration (Stanford Research Systems 830). The total reflection is calculated from the two measurements as:

$$R(\lambda) = 1 - T(\lambda) - A(\lambda) \tag{6.1}$$

With increasing wavelength, the total transmission increases at first because of reduced scattering and then decreases due to the stronger absorption of the ITO layer at longer wavelengths. The total reflection, on the other hand, decreases (with increasing wavelength) due to the reduced scattering and is finally dominated by specular reflection at the long wavelength end of the spectrum, which is less dependent on the bias across the PDLC film. The ITO layer used in this cell has a large absorption in the near infrared because it is optimized for maximum transmission in the visible spectrum while providing good conductivity. We note that the slight difference in the transmission data between Figure 6.2 and Figure 6.4 is likely due to sample aging ($\sim$ 1 month) in ambient environment between measurements and slight differences in the measurement techniques. Effects of space environment on the device are beyond the scope of this manuscript but will be considered in future work.

6.4 Momentum calculation

With all the optical properties measured, we can calculate the momentum transferred to the PDLC device under solar illumination. The initial and final

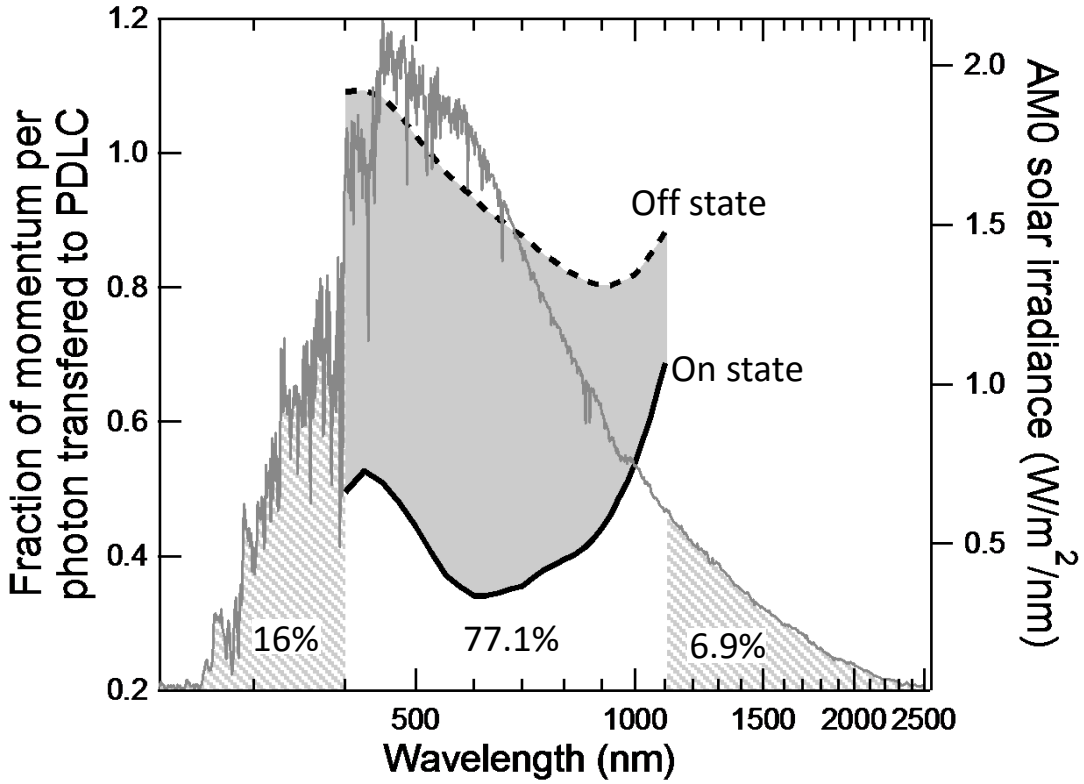

Figure 6.5: Fraction of momentum per photon transferred to the PDLC (left axis) in the on and off states at different wavelengths (400-1100 nm) overlaid with the AM0 solar irradiance spectrum (right axis). The measured data covers 77.1% of the total energy (or momentum) of the AM0 solar spectrum.

momenta of monochromatic photons with momentum magnitude of p_0 are:

$$\vec{p_i} = p_0 \hat{s},$$

and

$$\vec{p_f} = p_0[R_s \hat{s} - 2R_s(\hat{n} \cdot \hat{s} - R_d C_{Rd} \hat{n} + T_d C_{Td} \hat{n}],$$

respectively, where $\hat{n}$ is the surface normal unit vector of the PDLC device, $\hat{s}$ is the unit vector for initial photon direction, T_s is the direct transmission coefficient (i.e. the fraction of incident photons directly transmitted), R_s is the specular reflection coefficient, T_d is the diffusive transmission coefficient, R_d is the diffusive reflection coefficient and C_{Rd} and C_{Td} are the diffusive transmission and reflection momentum coefficients. C_{Rd} and C_{Td} represent the average fraction of momenta (absolute value) of diffusive transmitted or diffusive reflected photons, which are calculated from the scattering angular distribution measurement as:

$$C_{Td} = \frac{\int_0^{\pi/2} I_T(\theta) cos\theta sin\theta d\theta}{\int_0^{\pi/2} I_T(\theta) sin\theta d\theta}, \tag{6.2}$$

and

$$C_{Rd} = \frac{|\int_{\pi/2}^{\pi} I_R(\theta) cos\theta sin\theta d\theta|}{\int_{\pi/2}^{\pi} I_R(\theta) sin\theta d\theta}, \tag{6.3}$$

where $I_T(\theta)$ and $I_R(\theta)$ are the measured normalized powers in the scattering profile measurement (Figure 6.3).The difference in the initial and final momenta is the

momentum transferred to the PDLC:

$$\vec{p}_{sail} = \vec{p}_i - \vec{p}_f = p_0[(1 - T_s - R_s)\vec{s} + (2R_s(\vec{n} \cdot \vec{s}) + R_d C_{Rd} + T_d C_{Td})\vec{n}]. \tag{6.4}$$

The maximum thrust and greatest switchability occurs when the solar sail is directly facing the sun (normal incidence illumination), which is the case that we will consider. Thus, at normal incidence, $\vec{n} \cdot \vec{s} = 1$, and the equation above reduces to:

$$\vec{p}_{sail} = p_0(1 + R_s - T_s + R_d C_{Rd} - T_d C_{Td})\vec{n}. \tag{6.5}$$

Here we define a wavelength dependent coefficient:

$$f_p(\lambda) = 1 + R_s(\lambda) - T_s(\lambda) + R_d(\lambda) C_{Rd}(\lambda) - T_d(\lambda) C_{Td}(\lambda), \tag{6.6}$$

which gives the fraction of momentum per photon transferred to the PDLC, shown in Figure 6.5. Because a solar sail would be illuminated by a broadband solar spectrum in space, the weighted average fraction of momentum transferred to the PDLC (in either state) is calculated by

$$f_{avg} = \frac{\int f_p(\lambda) S(\lambda) d\lambda}{\int S(\lambda) d\lambda}, \tag{6.7}$$

where $S(\lambda)$ is the AM0 solar irradiance. The change of the fraction of the weighted average momentum transferred to PDLC between the on state and the off state is:

$$\Delta f_{avg} = f_{avg,on} - f_{avg,off} \tag{6.8}$$

$|\Delta f_{avg}|$ is a primary figure of merit for a switchable solar sail, where larger values of correspond to greater switchability of the momentum transfer. Over our measurement range, from 400 nm to 1100 nm, $|\Delta f_{avg}| \approx 0.5$.

Compared with the RCD devices on IKAROS that are switched from diffusive scattering in the off state to specular reflection in the on state, our transmissive-type PDLC devices that are switched from diffusive scattering in the off state to direct transmission in the on state provide a larger momentum transfer difference, Δf_{avg}. Figure of merits of the RCD devices on IKAROS are also calculated based on the data provided in [81], where a Lambertian scattering profile is assumed for all wavelengths rather than measured as in this paper (Table 6.1). Although our measurement range was limited to 400∼1100 nm, it covers 77.1% of the energy/momentum available from the AM0 solar spectrum. If the device had no switchability between 300∼400 nm and 1100∼2000 nm (which is unlikely), the device would still outperform the RCD devices on IKAROS by nearly a factor of four.

	RCD on IKAROS (300 to 2000 nm)	Our device (400 to 1100 nm)
$f_{avg,on}$	1.51	0.43
$f_{avg,off}$	1.40	0.93
$\lvert\Delta f_{avg}\rvert$	0.11	0.50

Table 6.1: Comparison of figure of merits between our device and IKAROS.

Because the orientations of the liquid crystal droplet directors are determined by the electric field, we further explore the possibility of reducing the turn-on voltage and power consumption of the PDLC device by thinning the PDLC layer. However, a thinner PDLC device potentially has less scattering in the off state and thus will compromise its momentum switchability. To demonstrate the tradeoff, five PDLC cells with different thicknesses but the same PDLC mixture and ITO coated glasses (SPI Supplies) are made and tested. The visual images of these PDLC cells in the on and off states show that the direct transmission in the on states do not change much with thickness but in the off state, thinner cells start to appear more transparent, indicating less scattering and more direct transmission (Figure 6.6a). Optical properties of the five cells are measured following the procedures described above, and the fractions of the weighted average momentum transferred to the PDLCs are calculated (Figure 6.6b). As expected, momentum transferred to the PDLC in the off state decreases for thinner cells, while the momentum transferred to the PDLC in the on state change very little.

To measure the power consumption of the PDLC device, a load resistor of 1.2 kΩ is connected in series with the PDLC. When the cell is in the on state, the current through the resistor and the voltage across the PDLC device are recorded in the time domain. The product of the current and voltage is then averaged over a period to determine the average power consumption of the PDLC in the on state. Their turn-on voltages are determined (Figure 6.6c). They both follow an approximate linear relationship with cell thickness over the voltage range consider in these experiments. Therefore, reducing the PDLC thickness is an effective way to re-

duce power consumption. Ohmic loss in the TCO and leakage current throughout the device eventually limit the minimum power consumption; however, the reduced switchability for films below a few microns will likely restrict how thin these devices can be made for useful solar sail applications.

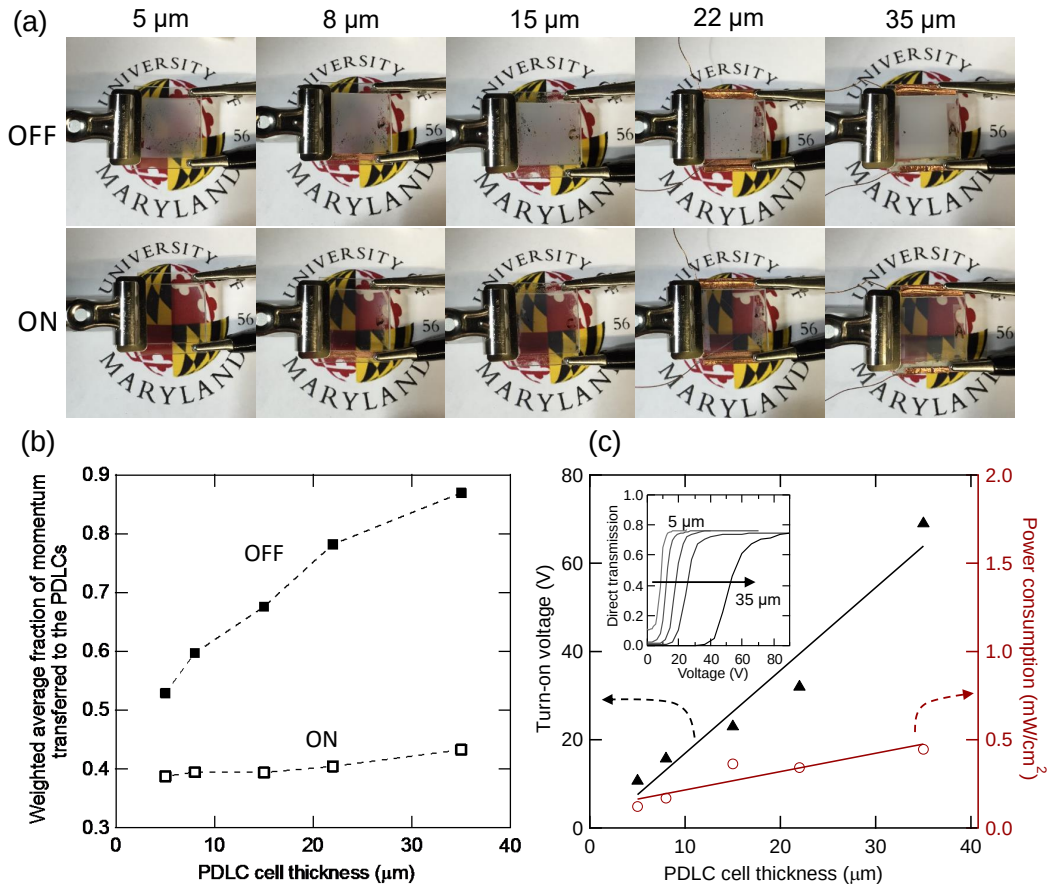

Figure 6.6: a) Optical images of (1 in x 1 in) devices in the off state (1st row) and the on state (2nd row) of five PDLC cells with increasing thickness from left to right. Cell thickness is measured by optical interferometry. b) Average fraction of momentum transferred to the PDLCs weighed by the AM0 solar spectrum over the measurement range (400 nm to 1100 nm) for the five devices. c) Turn-on voltages (left), determined by 90% transmission at 650 nm incident illumination, and power consumption per unit area (right) in the on state as a function of PDLC thickness. The black and red lines are linear fits to the turn-on voltage and power consumption data, respectively. Inset: direct transmission under 650 nm illumination versus applied RMS voltage.

In summary, we fabricated and characterized a transmissive-type PDLC de-

vice for use as an electrically tunable radiation pressure modulator for propellantless attitude control of a solar sail. The PDLC device provides large, broadband differences in the optical properties between on and off states without the need for polarizers. The measured optical properties (transmission, reflection, absorption, and scattering) are combined to calculate the expected momentum transferred to the device as a function of incident wavelength. The difference in weighted average momentum per photon over the measurement range (400 nm to 1100 nm, covering 77.1% of the total energy/momentum of the AM0 solar spectrum) between the on and off states can be as large as 0.5, approximately 4 times higher than previous reflective-type devices. The approach of calculating the momentum transfer of light based on measured data can be applied to other types of scattering materials and devices. Lastly, we showed the impact of PDLC thickness on the optical momentum transfer and electrical power consumption and discussed the trade-off between optical switchablity and power consumption. Thinner cells enable reduced operating voltages and power consumption while thicker cells provide larger momentum difference between the on and off states. The desired thickness of the PDLC device will depend on mission specific requirements but can easily be modified using these techniques. The development of an electrically switchable radiation pressure modulator will enable new functionality for solar sail missions and will expedite the development of long-term and long-distance, propellant-free space flight.

Chapter 7: Conclusions and outlook

This thesis presents research endeavors into two distinct fields that are deeply connected by radiation pressure. In Chapter 2-4, the challenge of measuring radiation pressure in an ambient environment is addressed through two novel experimental methods. In Chapter 5-6, the concept of using switchable optical materials as a way of solar sail attitude control without moving parts is proposed and polymer dispersed liquid crystal devices are made and characterized, which shows great momentum transfer switchability under entire solar spectrum.

7.1 Radiation pressure measurements

With the rise of optomicromechanical devices and cavity optomechanics, measuring the radiation pressure has become an important problem due to accompanying photothermal effects. The first part of the thesis demonstrates that it is possible to measure the radiation pressure in an ambient environment quantitatively with great accuracy. Two different methods are used to separate radiation pressure and photothermal effects in two different experiments. The first experiment measures radiation pressure on an uncoated silicon nitride microcantilever under a single wavelength illumination (660 nm). The radiation pressure and photothermal effects are

separated through cantilever's frequency response and found to cause the cantilever to bend in opposite directions. The measured radiation pressure matches theoretical calculations, finding agreement within the calculated errors.

The second experiment demonstrates the first measurement of a wavelength dependent radiation pressure due to thin film interference of a silicon cantilever over a continuous wavelength range. A technique to obtain the local reflection and absorption spectrum from the in-situ transmission spectrum measurement is determined, which is essential to obtaining the predicted magnitude of radiation pressure. The tunable wavelength excitation measurement is a good way to distinguish photothermally driven oscillations from radiation pressure driven oscillations. For photothermally driven oscillations, the normalized cantilever amplitude response under different wavelength excitation aligns with the absorption spectrum while for radiation pressure driven oscillation, the normalized cantilever amplitude response under different wavelength excitation aligns with the reflection spectrum. This has been verified by exciting near the base and the free end of the cantilever.

Besides experimental methods, this thesis also presents a theoretical framework based on cantilever beam theory to transform any distributed force or bending moment at any position along the cantilever to a mode-dependent effective force analytically. This makes it easy to compare the deformation caused by photothermal effects and radiation pressure. First principle derivations of an effective force from photothermal effects such as bimetallic, thermal elastic and electronic deformation are also discussed. Although the thermal elastic and electronic deformation effects calculated for uncoated cantilevers are too small compared to what is ob-

served in the experiments, it brought insight into the complexity of thermal effects in a semiconductor micromechanical structure.

This thesis also presents other findings related to the radiation pressure measurement. Fano resonances have been observed when the excitation laser and detection laser beams are in close proximity. A model is given and able to fit the complex amplitude signal to extract resonant and non-resonant terms. Despite being an artifact in the radiation pressure experiment, polarization dependent photothermal bending based on nanophotonic gratings on a cantilever is demonstrated and shows great contrast in deflection between two different polarizations.

7.2 Polymer dispersed liquid crystals for solar sail attitude control

With the goal of utilizing switchable optical devices to achieve attitude control of a solar sail, various types of materials are discussed in this thesis in terms of performance and feasibility for application in a fully functioning solar sail. Among all candidates, the polymer dispersed liquid crystal (PDLC) device stands out and becomes the focus of this thesis due to its substantial and broadband differences in the optical properties between on and off states without the need for polarizers. They are also much easier to fabricated on large flexible substrates. Transmissive-type PDLC devices are fabricated and characterized. The thesis presents a formula to calculated the expected momentum transfered to the device at each wavelength based on measured optical properties (transmission, reflection, absorption, and scattering). A figure of merit is also defined in terms of momentum switchability as the

difference in the weighted average momentum per photon over the AM0 solar spectrum between on and off states. Due to the available light source and detectors , the measurement range is limited to between 400 nm to 1100 nm, covering 77.1% of the total energy/momentum of the AM0 solar spectrum. The figure of merit can be as large as 0.5, approximately 4 times higher than previous reflective-type devices. This approach of calculating the momentum transfer from light based on measured data can be applied to other types of scattering materials and devices. Further, the impact of PDLC thickness on the optical momentum transfer and electrical power consumption is also discussed. There is a trade-off between optical switchablity and power consumption. Thinner cells enable reduced operating voltages and power consumption, while thicker cells provide a larger momentum difference between the on and off states. The desired thickness of the PDLC device will depend on mission specific requirements but can easily be modified using these techniques. The development of an electrically switchable radiation pressure modulator will enable new functionality for solar sail missions and will expedite the development of long-term and long-distance, propellant-free space flight.

7.3 Future work for PDLCs

To further achieve applying the PDLCs to the solar sails, we first need to look into fabrication of PDLC devices on flexible substrates and how to characterize the device performance. Preliminary results have been achieved by fabricating the PDLC device on ITO coated PET material. The fabricated PDLC device shows

good performance in terms of switchability under a large bending curvature (Figure 7.1).

Further improvement of PDLC devices for solar sail applications can come from two aspects. Firstly, the optical switchability of the PDLC layer and its turn-on voltage could be improved by exploiting different combinations of liquid crystals and polymer matrices. Furthermore, the total area density of the PDLC devices could be reduced if lighter transparent electrodes are used, such as silver nanowires, carbon nanotubes and graphene.

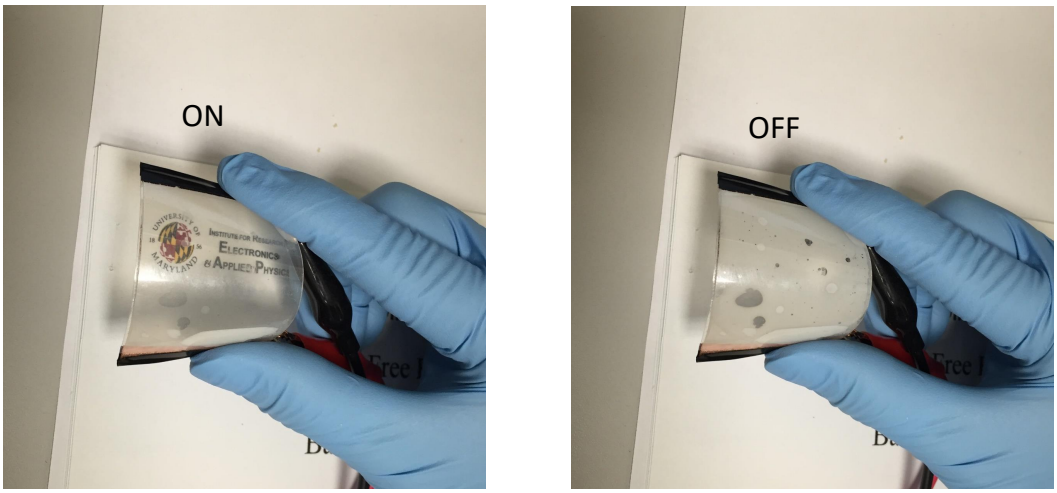

Figure 7.1: Images of flexible PDLC devices made on ITO coated PET material with a thickness of 200 μm.

7.4 Potential experiments to solve the Abraham-Minkowski controversy

In previous chapters, we demonstrate that our experimental setup is capable of measuring radiation pressure as small as a few pico-newtons in an ambient environment. However, the current setup cannot resolve the Abraham-Minkowski controversy for the following reasons. Our setup measures the radiation pressure caused by reflection and absorption, but these photons do not give us any information about the momentum of light inside the medium. As shown in Figure 7.2, reflected photons do not enter the medium at all and absorbed photons have zero momentum after they have been absorbed. Photons transmitted at the first air-cantilever interface will generate a impulse on the medium due to the change of photon momentum inside the medium ($p_n = \alpha\hbar k$, where $\alpha = n$ or $\alpha = 1/n$). This impulse will cause the medium to move up (if $\alpha = n$) or down (if $\alpha = 1/n$). However, this movement is soon stopped by the counteractive impulse when the photon leaves the medium. Under a constant illumination power, for a lossless cantilever, the photon fluxes at the top and bottom interfaces are equal at any given time, therefore, no net force is generated on the medium from transmitted photons.

In order to measure the photon momentum inside the medium, we first need to have a perfect anti-reflection coating and a lossless material to minimize the radiation pressure because it is considered a background offset to the experiment and it is hard to detect a small change on a large background. Secondly, we need to measure

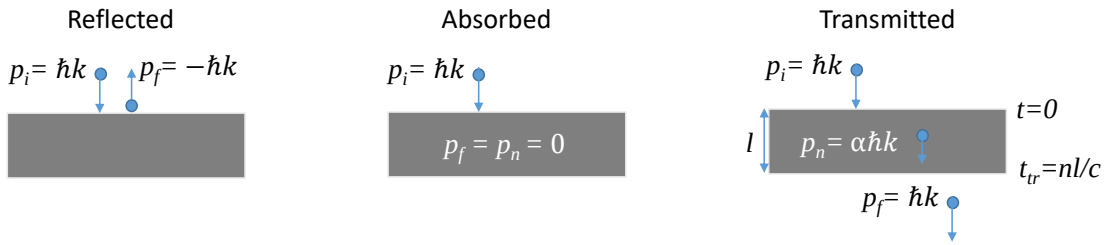

Figure 7.2: Schematics of the momenta of reflected, absorbed and transmitted photons at each stage when interacting with a medium with refractive index n which is free to move (*e.g.* a cantilever). The gray slab represents the cantilever. p_i is the initial photon momentum in air, p_n is the photon momentum in the medium and p_f is the final momentum of that photon.

the movement of the cantilever when the photons transmitted into the medium are still inside the medium and no counteractive impulse have been generated yet. We can achieve this by increasing the transit time of light traveling inside the medium and using a short laser pulse that is shorter than the transit time. However, increasing the thickness of the cantilever will decrease the measurement sensitivity. Using material with strong polaritonic effects as suggested in [30] is a potential solution.

So far we have been discussing about light entering from the air into the medium. What if the light is generated inside the medium? Here we propose an interesting experiment that incorporate a cantilever with direct bandgap material and a p-n junction in it. On top the cantilever, a photogenic bandgap material is designed to restrict light from escaping upward. An anti-reflection coating is deposited on the other side of the cantilever so that light can transmit through without any reflection. When a voltage is applied to the junction, photons generated can only exit through the bottom of the cantilever. If the photon inside the medium has a momentum $n\hbar k$, the cantilever will bend down as a recoil and if the photon

inside the medium has a momentum $\hbar k/n$, the cantilever will bend down.

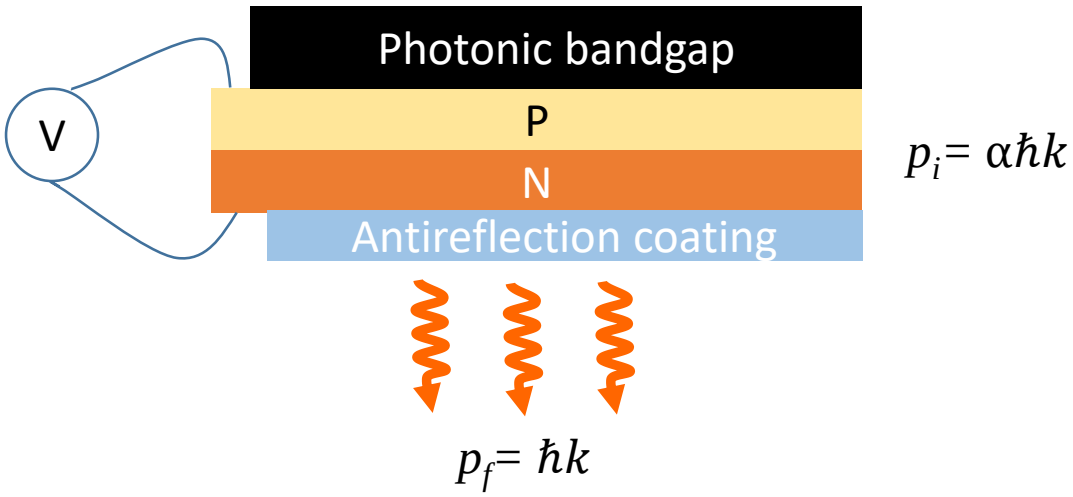

Figure 7.3: Proposed cantilever schematic for measuring the photon momentum inside the cantilever.

Appendix A: Modifications of the Cypher AFM

A.1 Free space optical path through the side window

The major modification of the Cypher AFM (Asylum Research) for the single wavelength radiation pressure measurement (660 nm) is shown in Figure A.1. Before the addition of the RainbowDrive, the light was introduced into the Cypher from the side. There are two advantages of this approach: (1) low optical loss along the optical path (about a quarter of the optical power reaching the cantilever) and (2) the measurement can be done with the Cypher door closed, which minimizes the noise level. The disadvantage of this approach is that it is very hard to align the laser beam onto cantilever because it is not possible to do fine manual adjustments of the optics inside the Cypher chamber.

A.2 Free space coupling into the RainbowDrive

RainbowDrive is an add-on module Asylum Research made for us to aid the process of coupling external light onto the cantilever. It consists of a motorized mirror that can be connected to the mother board and be controlled by the software. It greatly reduces our time of the initial alignment and makes it possible to micro-

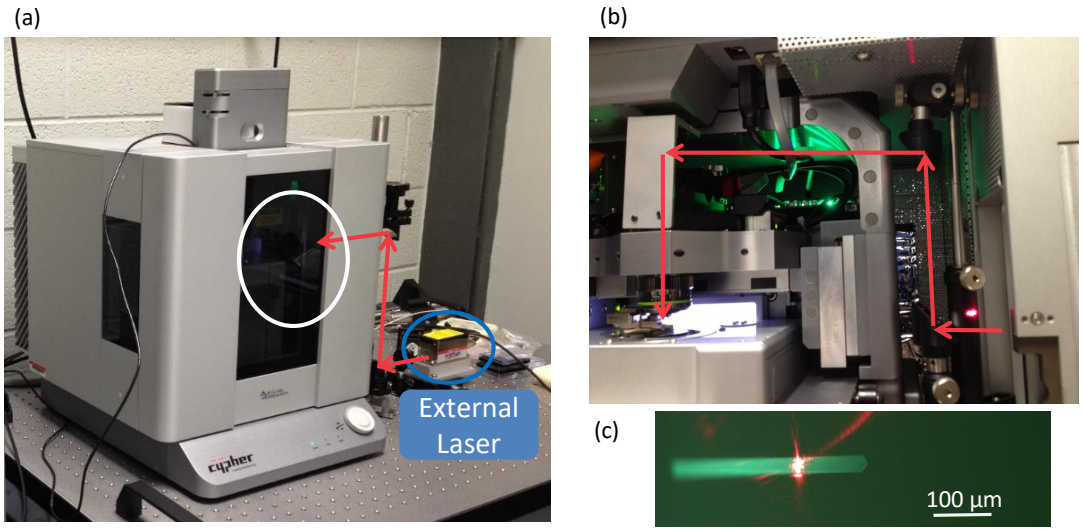

Figure A.1: (a) External laser coupled into the atomic force microscope through a customized transparent window on the side of the Cypher. (b) Optics inside the Cypher chamber (the area in the white circle in (a)). A 45° diachronic hot mirror is placed above the objective using a custom designed holder to reflect the external laser beam down while letting pass the light for imaging. (c) Image of the cantilever with the focused external laser beam. The actual spot size of the focused light is much smaller than it seems in the photo because many pixels in the photodetector are saturated, appearing white thus making the spot bigger.

adjust the beam position with a few mouse clicks. However, several drawbacks exist in this approach. Firstly, the optical loss is high due to multiple elements inside the RainbowDrive. Secondly, the RainbowDrive's optics, with the original C560TME aspherical lens in place, is designed for a laser beam with a divergence of 71 mrad (the divergence of the laser diode used in the BlueDrive). It is not designed for a collimated input beam. In order to get a decently focused spot size on the cantilever, light coming out of the RainbowDrive (before the objective) need to be collimated. Lastly, RainbowDrive requires the input light coming from the front of the Cypher, which forces the door to be left open during the measurement (Figure A.2).

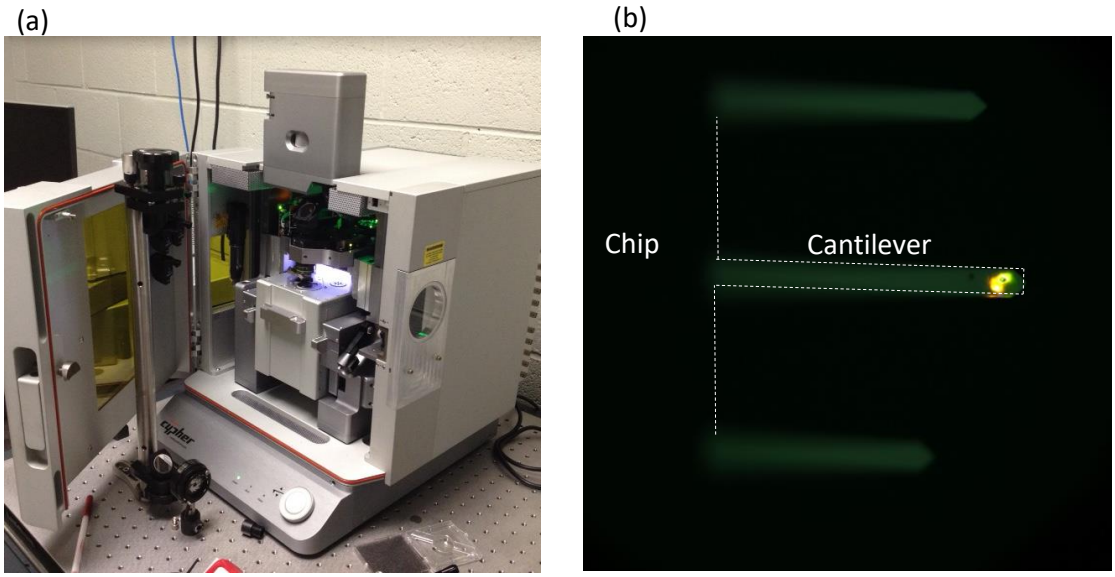

Figure A.2: (a) External laser coupled into the atomic force microscope through the RainbowDrive from the front of the Cypher. (b) Image of the cantilever with the focused external infrared laser beam.

A.3 Fiber coupling into the RainbowDrive

It is possible to couple light into the RainbowDrive through an optical fiber (Figure A.3 and A.4). Depending on the requirement, either multi-mode (MM) fiber or single-mode (SM) fiber can be used. The MM fiber is used when a broad spectrum needs to be launched into the Cypher at once. A parabolic right-angle mirror is used as a fiber coupler to couple light into the MM fiber because the focal length of a parabolic mirror is independent of the wavelength. The coupling efficiency to a MM fiber is high, but it is not possible to focus the output light from a MM fiber to a diffraction limited spot because the Gaussian mode and wavefront are lost during coupling. The SM fiber can be used to couple a narrow band of wavelengths into the Cypher, and the output beam quality is very good and can be focused down to a small spot. However, the coupling efficiency is low. The comparison of different coupling method is shown in Table A.1.

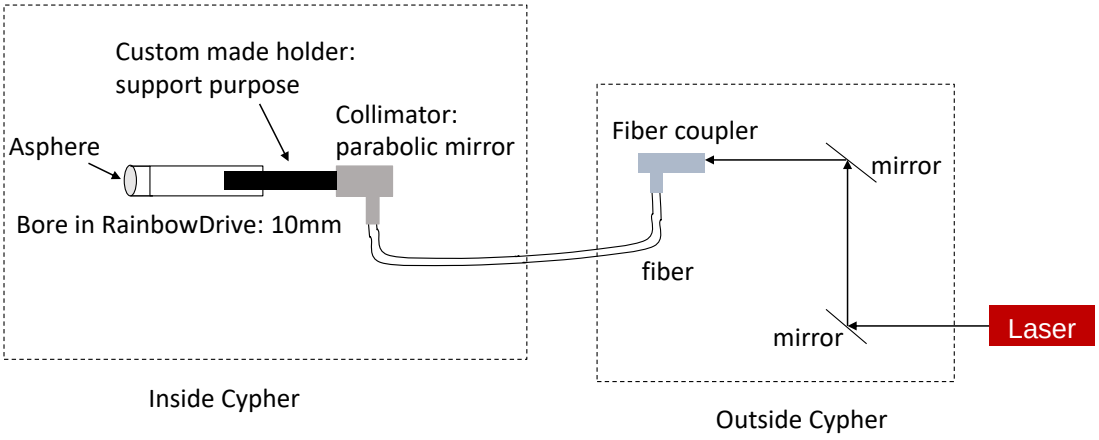

Figure A.3: Design schematic of the fiber optic coupling system that launches the laser beam into the RainbowDrive.

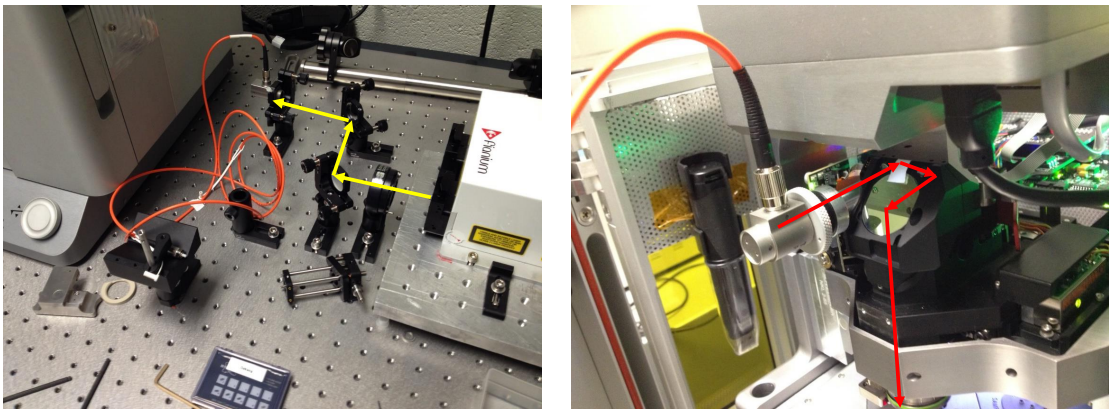

Figure A.4: Actual images of the fiber coupling setup.

Power loss at each step (for 1060 nm)	SM fiber	MM fiber	Free space
Steering mirrors	5%	5%	40%
Fiber coupler	83%	30%	0%
RainbowDrive	50%	50%	50%
Extended hot mirror	10%	10%	10%
"Notch" mirror	40%	40%	40%
Objective	40%	40%	40%
Focusing on cantilever	0%	70%	0%
Total coupling efficiency	2.62%	3.23%	9.85%
Final beam wavefront	Good	Bad	OK

Table A.1: Percentage of optical power loss at each optical element in the fiber coupling optical path for a wavelength of 1060 nm. The total end-to-end coupling efficiency and the final beam wavefront quality are also listed in the table.

A.4 Determining the spot size of a laser beam focused by an objective

In the radiation pressure measurement setup, the excitation laser is focused by the same imaging objective (Olympus LUCPLFLN 20X) as the detection laser. In order to estimate the focusing spot size and divergence angle (to validate the normal incidence approximation), it is important to know the effective focal length of the objective. Most objectives are designed for infinite optical systems where the image distance is set to infinity, and a tube lens is strategically placed between the objective and the eyepieces to produce the final image. Infinity optical systems allow introduction of auxiliary components, such as filters, polarizers, into the parallel optical path between the objective and the tube lens with only a minimal effect on focus and aberration corrections [122]. Typical specifications of the objective include its working distance, magnification factor, and numerical aperture (NA). The relationship between magnification (M), focal length of the objective (f) and reference focal length of the tube lens (L) is [123]:

$$M = \frac{L}{f}. \tag{A.1}$$

Manufacturers have different tube lens focal lengths for their microscopes and for Olympus, L =180 mm [122]. So the focal length of the 20x objective should be 9 mm according to equation A.1.

To calculate the spot size d (diameter) and the divergent angle θ (maximal half-angle of the cone of light that exit the objective), it is tempting to use equations

$d = 1.22/NA$ and $\theta = \arcsin(NA)$. However, these are only valid when light rays cover the entire pupil of the objective, which is not satisfied in our space-limited laser focusing system. In this case, the actual f-number, the focal length of the objective divided by the diameter of input laser beam (D), is needed and the equations become $d = 2.44\lambda(f/\#)$ and $\theta = \arcsin(\frac{1}{2f/\#}) = 9.6°$, where $f/\#$ is the f-number. The diameter of the input laser beam is about 1.5 mm when entering the objective, corresponding to $f/6$, so the spot size is 9.7 μm and the divergence angle is 4.8°.

The analysis above treats the laser beam as conventional uniform spherical waves. However, the laser's Gaussian beam could diverge enormously from geometric optics in extreme cases. So a more accurate way is to use the lens formula for a Gaussian beam [124]:

$$\frac{1}{s + z_R^2/(s-f)} + \frac{1}{s'} = \frac{1}{f}, \tag{A.2}$$

where s is the distance of the waist of the input beam (object), s' is the distance of the waist of the output beam (image), f is the focal length of the objective and z_R is the Rayleigh range. Regarding s'/f as a function of s/f, we can write:

$$(s'/f) = 1 + \frac{(s/f) - 1}{[s/f - 1]^2 + (z_R/f)^2}. \tag{A.3}$$

The magnification is given by:

$$M = \frac{w_0'}{w_0} = \frac{1}{\sqrt{[1 - (s/f)]^2 + (z_R/f)^2}}, \tag{A.4}$$

where w_0 is the beam radius at the waist of the input beam and $w_0^{'}$ is beam radius

at the waist of the output beam.

The Vortran laser used in the experiment has a Rayleigh range of 2.12 m (from the manufacture's spec sheet) and the input beam waist is about 0.5 m away from the objective. Because $s/f \gg 1$ and $z_R \gg f$, the output beam waist is at the focal plane $s' \approx f$ and the spot size $2w_0' = m \times 2w_0 = 1/242 \times 1.5$ mm $= 6.2$ μm.

A.5 Wavelength-dependent force measurement procedure

Below we list the steps needed to perform wavelength-dependent radiation pressure measurements:

1. Replace BlueDrive with RainbowDrive.

2. Load the cantilever, focus the detection laser beam on the middle of the cantilever. Mark down the detection laser location. (Do not move the objective from now on.)

3. Calibrate the invOLS and the spring constant by engaging to contact with a substrate mounted on the bottom illumination holder.

4. Make coarse alignment of the external laser into RainbowDrive and made the laser spot visible in the field of view of the camera.

5. Make fine alignment by using the computer controlled RainbowDrive to focus the external laser on to the cantilever.

6. Remove the substrate holder.

7. Start cantilever tuning under optical excitation. (The AOTF needs to be in analog modulation mode.)

8. Measure the power transmitted under the cantilever.

9. Take out the cantilever holder and measure the power hitting the cantilever.

Appendix B: Additional information about the PDLC

B.1 Estimation of droplet size from SEM image

We can estimate the liquid crystal droplet size within the PDLC by the SEM image. The PDLC device is soaked in acetone for overnight so that the top substrate/electrode is removed and so are the liquid crystal droplets. The PDLC film with holes previously occupied by the droplets is then imaged in the scanning electron microscope (SEM) and processed with ImageJ to find the droplet size (Figure B.1). From the image, the PDLC has a mean droplet diameter of 444 nm with a standard deviation of 230 nm. The actual size of the droplets are larger because the cross section might not cut through the equator of every droplet (note: the maximum measured diameter is 868 nm).

To convert the pixels into an actual size, we need to know the pixel density, a.k.a pixel per inch (ppi). If the image is from an SEM, the metadata file associated with it will have the information. Without metadata, if there is a scale bar on the image, you can easily calibrate the ppi in ImageJ. Here are the steps:

1. Draw a line on top of the scale bar.
2. Go to 'Analyze' - 'Set Scale' and enter the known distance.
3. Further measurement or profile plot will be in actual units.

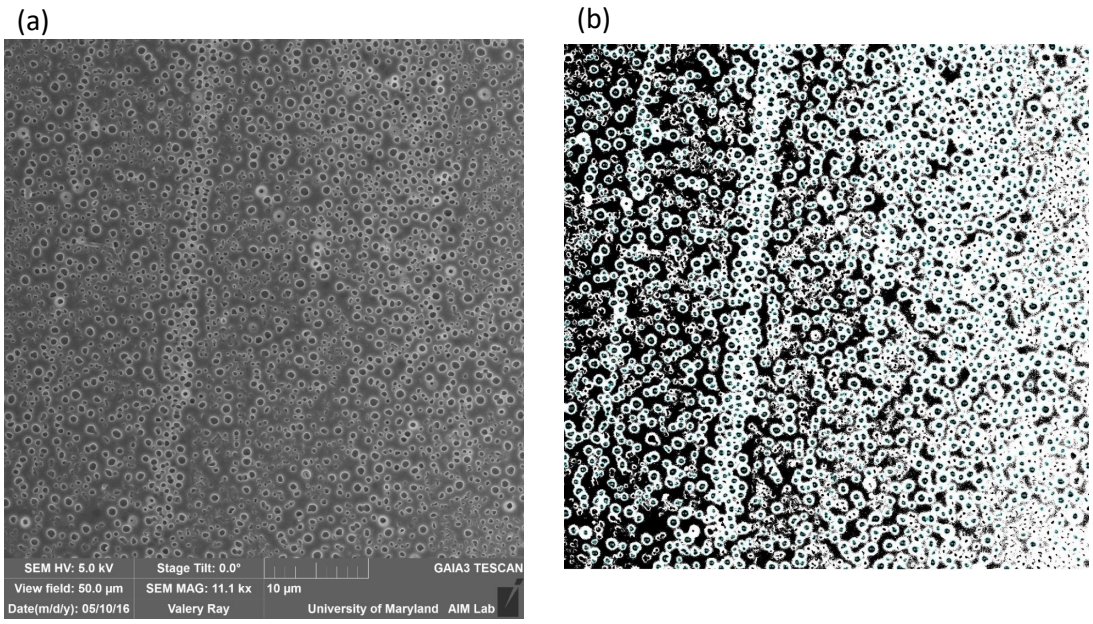

Figure B.1: (a) An SEM image of the surface of the PDLC film. (b) Circle detection within ImageJ to determine the droplet size.

B.2 PDLC device made with flexible substrate

We successfully demonstrate that PDLC devices can be made on flexible PET substrates. The PET substrate is 200 μm thick and coated with ITO. Glass beads with diameters of about 25 μm are used as spacers and spread onto the substrate before putting down the PDLC mixture and lamination. The device's switchable performance does not degrade due to bending as shown in Figure B.2.

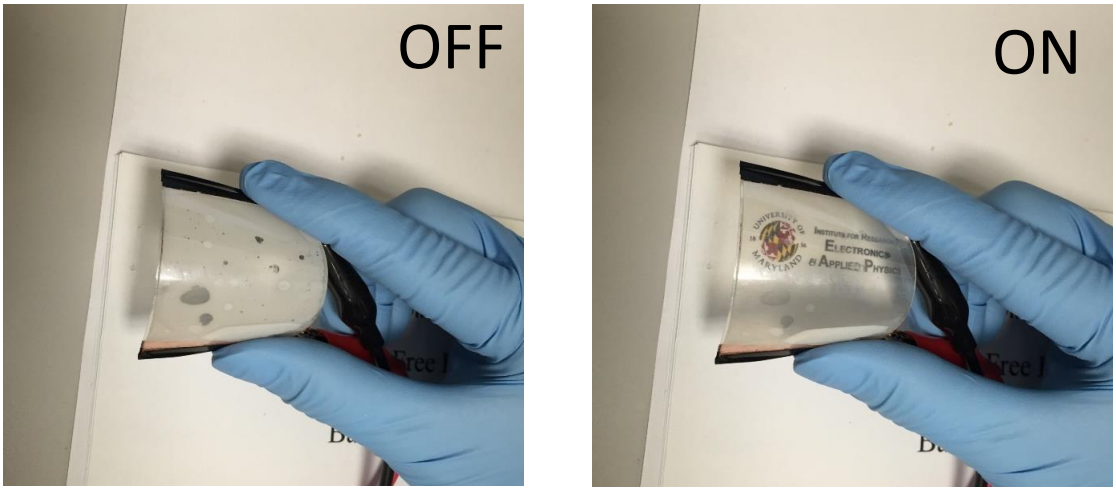

Figure B.2: PDLC device made with ITO-coated PET substrate (200 μm thick) shows good optical switchability even when it is bent significantly.

Bibliography

[1] Ulf Leonhardt. Momentum in an uncertain light. *Nature*, 444(December):823, 2006.

[2] Johannes Kepler. De cometis libelli tres, 1619.

[3] J. C. Maxwell. *A Treatise on Electricity and Magnetism*. Oxford University, 1st edition, 1873.

[4] Philip Gibbs. How does a light-mill work? https://en.wikipedia.org/wiki/Crookes_radiometer#cite_note-1. Accessed: 2016-11-06.

[5] Osborne Reynolds. On certain dimensional properties of matter in the gaseous state. part i. experimental researches on thermal transpiration of gases through porous plates and on the laws of transpiration and impulsion, including an experimental proof that gas is not a continuous plenum. part ii. on an extension of the dynamical theory of gas, which includes the stresses, tangential and normal, caused by a varying condition of gas, and affords an explanation of the phenomena of transpiration and impulsion. *Philosophical Transactions of the Royal Society of London*, 170:727–845, 1879.

[6] Philip Gibbs. How does a light-mill work? http://math.ucr.edu/home/baez/physics/General/LightMill/light-mill.html. Accessed: 2016-11-06.

[7] J. Clerk Maxwell. On stresses in rarified gases arising from inequalities of temperature. *Philosophical Transactions of the Royal Society of London*, 170:231–256, 1879.

[8] P N Lebedev. Investigations on the pressure forces of light. *Ann. Phys*, 6:433–445, 1901.

[9] E F Nichols and G F Hull. The Pressure Due to Radiation. (Second Paper.). *Phys. Rev. (Series I)*, 17(1):26–50, 1903.

[10] Dillon Lee. A celebration of the legacy of physics at dartmouth. *Dartmouth Undergraduate Journal of Science. (10TH ANNIVERSARY EDITION) Dartmouth College*, 2008.

[11] J.C.S Jones, R.V ; Richards. The Pressure of Radiation in a Refracting Medium. 221(1147):480–498, 1954.

[12] R.V Jones and B Lesie. Radiation pressure of light in a dispersive medium. *Proceedings of the Royal Society of London*, 360(1702):365–371, 1978.

[13] Gretchen Campbell, Aaron Leanhardt, Jongchul Mun, Micah Boyd, Erik Streed, Wolfgang Ketterle, and David Pritchard. Photon Recoil Momentum in Dispersive Media. *Physical Review Letters*, 94(17):170403, 2005.

[14] N. L. Balazs. The energy-momentum tensor of the electromagnetic field inside matter. *Phys. Rev.*, 91:408–411, 1953.

[15] G. B. Walker, D. G. Lahoz, and G. Walker. Measurement of the Abraham Force in a Barium Titanate Specimen. *Canadian Journal of Physics*, 53(23):2577–2586, 1975.

[16] Weilong She, Jianhui Yu, and Raohui Feng. Observation of a Push Force on the End Face of a Nanometer Silica Filament Exerted by Outgoing Light. *Physical Review Letters*, 101(24):243601, 2008.

[17] Iver Brevik. What Do Experiments in Optics tell us about Photon Momentum in Media? *arXiv preprint arXiv:1310.3684*, (x):11, 2013.

[18] Masud Mansuripur. Comment on Observation of a Push Force on the End Face of a Nanometer Silica Filament Exerted by Outgoing Light. *Physical Review Letters*, 103(1):019301, 2009.

[19] Stephen M. Barnett. Resolution of the Abraham-Minkowski Dilemma. *Physical Review Letters*, 104(7):070401, 2010.

[20] C. Baxter and Rodney Loudon. Radiation pressure and the photon momentum in dielectrics. *Journal of Modern Optics*, 57(10):830–842, 2010.

[21] Peter W. Milonni and Robert W. Boyd. Momentum of Light in a Dielectric Medium. *Advances in Optics and Photonics*, 2(4):519, 2010.

[22] John Jackson. *Classical Electrodynamics*. Wiley, New York, 3rd edition, 1998.

[23] Author A F Gibson, M F Kimmitt, A O Koohian, D E Evans, and G F D Levy. A study of radiation pressure in a refractive medium by the photon drag effect. *Proceedings of the Royal Society of London*, 370(1742):303–311, 1980.

[24] Kenneth J Chau and Henri J Lezec. Revisiting the Balazs thought experiment in the case of a left-handed material : displacement of a dispersive , dissipative negative-index slab Abstract :. *Optics Express*, 20(9):10138, 2012.

[25] Iver Brevik. Comment on Observation of a Push Force on the End Face of a Nanometer Silica Filament Exerted by Outgoing Light. *Physical Review Letters*, 103(21):219301, 2009.

[26] A Ashkin and M Dziedzic. Radiation Pressure on a Free Liquid Surface. *Physical Review Letters*, 30, 1973.

[27] Nelson G C Astrath, Luis C Malacarne, Mauro L Baesso, Gustavo V B Lukasievicz, and Stephen E Bialkowski. Unravelling the effects of radiation forces in water. *Nature communications*, 5:4363, 2014.

[28] Li Zhang, Weilong She, Nan Peng, and Ulf Leonhardt. Experimental evidence for Abraham pressure of light. *New Journal of Physics*, 17(5):053035, 2015.

[29] Iver Brevik and Simen Å. Ellingsen. Detection of the Abraham force with a succession of short optical pulses. *Physical Review A*, 86(2):025801, 2012.

[30] M. Labardi. Direct measurement of laser momentum transfer to dense media by means of atomic force microscopy cantilevers. *Journal of Vacuum Science & Technology B: Microelectronics and Nanometer Structures*, 14(2):868, 1996.

[31] CR McInnes. *Solar Sailing: Technology, Dynamics and Mission Applications*. Springer, 2004.

[32] Giovanni Vulpetti, Les Johnson, and Gregory L Matloff. *Solar sails: a novel approach to interplanetary travel*. Springer, 2014.

[33] Jason Davis. Sailing to the worlds most famous comet. http://sail.planetary.org/story-part-1.html. Accessed: 2016-11-12.

[34] Cosmos 1. https://en.wikipedia.org/wiki/Cosmos_1. Accessed: 2016-11-12.

[35] Ikaros. https://en.wikipedia.org/wiki/IKAROS. Accessed: 2016-11-12.

[36] Nanosail-d2. https://en.wikipedia.org/wiki/NanoSail-D2. Accessed: 2016-11-12.

[37] Crookes radiometer. https://en.wikipedia.org/wiki/Sunjammer_(spacecraft). Accessed: 2016-11-12.

[38] Lightsail 2. https://en.wikipedia.org/wiki/LightSail_2/. Accessed: 2016-11-12.

[39] Lightsail-a satellite overview. http://spaceflight101.com/spacecraft/lightsail-a/. Accessed: 2016-11-12.

[40] Near-earth asteroid scout. https://en.wikipedia.org/wiki/Near-Earth_Asteroid_Scout. Accessed: 2016-11-12.

[41] Dustin Kleckner and Dirk Bouwmeester. Sub-kelvin optical cooling of a micromechanical resonator. *Nature*, 444(7115):75–8, 2006.

[42] S Gigan, H R Böhm, M Paternostro, F Blaser, G Langer, J B Hertzberg, K C Schwab, D Bäuerle, M Aspelmeyer, and a Zeilinger. Self-cooling of a micromirror by radiation pressure. *Nature*, 444(7115):67–70, 2006.

[43] A. Schliesser, P. Del'Haye, N. Nooshi, K. J. Vahala, and T. J. Kippenberg. Radiation pressure cooling of a micromechanical oscillator using dynamical backaction. *Physical Review Letters*, 97(December):243905, 2006.

[44] Jasper Chan, T P Mayer Alegre, Amir H Safavi-Naeini, Jeff T Hill, Alex Krause, Simon Gröblacher, Markus Aspelmeyer, and Oskar Painter. Laser cooling of a nanomechanical oscillator into its quantum ground state. *Nature*, 478(7367):89–92, 2011.

[45] Paul R. Wilkinson, Gordon A. Shaw, and Jon R. Pratt. Determination of a cantilever's mechanical impedance using photon momentum. *Applied Physics Letters*, 102(18):184103, 2013.

[46] Z. Marcet, Z.H. Hang, S.B. Wang, J. Ng, C.T. Chan, and H.B. Chan. Measurement of Enhanced Radiation Force on a Parallel Metallic-Plate System in the Microwave Regime. *Physical Review Letters*, 112(4):045504, 2014.

[47] Drew R Evans, Ponlawat Tayati, Hongjie An, Ping Koy Lam, Vincent S J Craig, and Tim J Senden. Laser actuation of cantilevers for picometre amplitude dynamic force microscopy. *Scientific reports*, 4:5567, 2014.

[48] Constanze Höhberger Metzger and Khaled Karrai. Cavity cooling of a microlever. *Nature*, 432(7020):1002–5, 2004.

[49] O. Hahtela and I. Tittonen. *Applied Physics B*.

[50] David M. Weld and Aharon Kapitulnik. Feedback control and characterization of a microcantilever using optical radiation pressure. *Applied Physics Letters*, 89(16):164102, 2006.

[51] M. Allegrini, C. Ascoli, P. Baschieri, F. Dinelli, C. Frediani, A. Lio, and T. Mariani. Laser thermal effects on atomic force microscope cantilevers. *Ultramicroscopy*, 42-44:371–378, 1992.

[52] O Marti, A Ruf, M Hipp, and H Bielefeldt. Mechanical and thermal effects of laser irradiation on force microscope cantilevers. *Ultramicroscopy*, 42:345–350, 1992.

[53] N. Selden, C. Ngalande, S. Gimelshein, E. Muntz, A. Alexeenko, and A. Ketsdever. Area and edge effects in radiometric forces. *Physical Review E*, 79(4):041201, 2009.

[54] B. Ilic, S. Krylov, and H. G. Craighead. Theoretical and experimental investigation of optically driven nanoelectromechanical oscillators. *Journal of Applied Physics*, 107(3):034311, 2010.

[55] Massimo Vassalli, Valerio Pini, and Bruno Tiribilli. Role of the driving laser position on atomic force microscopy cantilevers excited by photothermal and radiation pressure effects. *Applied Physics Letters*, 97(14):143105, 2010.

[56] John E. Sader, James W. M. Chon, and Paul Mulvaney. Calibration of rectangular atomic force microscope cantilevers. *Review of Scientific Instruments*, 70(10):3967, 1999.

[57] M. J. Higgins, R. Proksch, J. E. Sader, M. Polcik, S. Mc Endoo, J. P. Cleveland, and S. P. Jarvis. Noninvasive determination of optical lever sensitivity in atomic force microscopy. *Review of Scientific Instruments*, 77(1):013701, 2006.

[58] S. Rast, C. Wattinger, U. Gysin, and E. Meyer. Dynamics of damped cantilevers. *Review of Scientific Instruments*, 71(7):2772, 2000.

[59] S M Cook, K M Lang, K M Chynoweth, M Wigton, R W Simmonds, and T E Schäffer. Practical implementation of dynamic methods for measuring atomic force microscope cantilever spring constants. *Nanotechnology*, 17(9):2135–2145, 2006.

[60] Dakang Ma, Joseph L. Garrett, and Jeremy N. Munday. Quantitative measurement of radiation pressure on a microcantilever in ambient environment. *Applied Physics Letters*, 106(9), 2015.

[61] Andrew R Salmon, Matthew J Capener, Jeremy J Baumberg, and Stephen R Elliott. Rapid microcantilever-thickness determination by optical interferometry. *Meas. Sci. Technol. Measurement Science and Technology Meas. Sci. Technol*, 25(25):15202–7, 2014.

[62] Shahrul Kadri, Hideki Fujiwara, and Keiji Sasaki. Fano-like resonance in an optically driven atomic force microscope cantilever. *Optics express*, 19(3):2317–24, 2011.

[63] Sophocles J Orfanidis. *Electromagnetic waves and antennas*. Rutgers University, 2002.

[64] Edward D Palik. *Handbook of optical constants of solids*, volume 3. Academic press, 1998.

[65] Bending moment. https://en.wikipedia.org/wiki/Bending_moment. Accessed: 2016-11-26.

[66] Eulerbernoulli beam theory. https://en.wikipedia.org/wiki/Euler%E2%80%93Bernoulli_beam_theory. Accessed: 2016-11-26.

[67] John Melcher, Shuiqing Hu, and Arvind Raman. Equivalent point-mass models of continuous atomic force microscope probes. *Applied Physics Letters*, 91(5), 2007.

[68] D. Ramos, J. Tamayo, J. Mertens, and M. Calleja. Photothermal excitation of microcantilevers in liquids. *Journal of Applied Physics*, 99(12), 2006.

[69] Valerio Pini, Bruno Tiribilli, Cecilia Maria Cristina Gambi, and Massimo Vassalli. Dynamical characterization of vibrating afm cantilevers forced by photothermal excitation. *Phys. Rev. B*, 81:054302, 2010.

[70] Daniel Kiracofe, Kei Kobayashi, Aleksander Labuda, Arvind Raman, and Hirofumi Yamada. High efficiency laser photothermal excitation of microcantilever vibrations in air and liquids. *Review of Scientific Instruments*, 82(1), 2011.

[71] Yaqin Song, Bernard Cretin, Dragan M Todorovic, and Pascal Vairac. Study of photothermal vibrations of semiconductor cantilevers near the resonant frequency. *Journal of Physics D: Applied Physics*, 41(15):155106, 2008.

[72] Albert Prak and Theo S. J. Lammerink. Effect of electronic strain on the optically induced mechanical moment in silicon microstructures. *Journal of Applied Physics*, 71(10):5242–5245, 1992.

[73] D. M. Todorovic. Photothermal and electronic elastic effects in microelectromechanical structures. *Review of Scientific Instruments*, 74(1):578–581, 2003.

[74] A. Passian, A. Wig, F. Meriaudeau, T. L. Ferrell, and T. Thundat. Knudsen forces on microcantilevers. *Journal of Applied Physics*, 92(10), 2002.

[75] J. R. Barnes, R. J. Stephenson, C. N. Woodburn, S. J. O'Shea, M. E. Welland, T. Rayment, J. K. Gimzewski, and Ch. Gerber. A femtojoule calorimeter using micromechanical sensors. *Review of Scientific Instruments*, 65(12):3793, 1994.

[76] Kurt Gramoll. Mechanics - theory. http://www.ecourses.ou.edu/cgi-bin/ebook.cgi?doc=&topic=me&chap_sec=06.1&page=theory. Accessed: 2016-07-16.

[77] D. M. Todorovic, B. Cretin, Y. Q. Song, and P. Vairac. Electronic and thermal generation of vibrations of optically excited cantilevers. *Journal of Applied Physics*, 107(2):023516, 2010.

[78] Aleksander Labuda, Jason Cleveland, Nicholas A Geisse, Marta Kocun, Ben Ohler, Roger Proksch, Mario B Viani, and Deron Walters. Photothermal excitation for improved cantilever drive performance in tapping mode atomic force microscopy.

[79] Introduction to the spacecraft attitude concept. http://www.spacealliance.ro/articles/view.aspx?id=200903060613. Accessed: 2016-11-26.

[80] Chapter 11. typical onboard systems. https://solarsystem.nasa.gov/basics/bsf11-2.php. Accessed: 2016-11-26.

[81] Ryu Funase, Y Shirasawa, Y Mimasu, O Mori, Y Tsuda, T Saiki, and J Kawaguchi. Fuel-free and oscillation-free attitude control of ikaros solar sail spacecraft using reflectivity control device. In *28th International Symposium on Space Technology and Science*, 2011.

[82] Y. Zhao, Z. C. Feng, Y. Liang, and H. W. Sheng. Laser-induced coloration of WO3. *Applied Physics Letters*, 71(16):2227, 1997.

[83] Richard S. Crandall and Brian W. Faughnan. Measurement of the diffusion coefficient of electrons in WO3 films. *Applied Physics Letters*, 26(3):120–121, 1975.

[84] Arno Seeboth and Detlef Lötzsch. *Thermochromic and thermotropic materials*. CRC Press, 2013.

[85] Jiajia Zhang, Haiyan He, Yi Xie, and Bicai Pan. Theoretical study on the tungsten-induced reduction of transition temperature and the degradation of optical properties for vo2. *Journal of Chemical Physics*, 138(11):1–7, 2013.

[86] Mohammed Soltani, Mohamed Chaker, and Emile Haddad. Thermochromic vanadium dioxide (VO2) smart coatings for switching applications. *Applied Physics in the 21st Century*, 661(2), 2008.

[87] Ivan P. Parkin and Troy D. Manning. Intelligent thermochromic windows. *Journal of Chemical Education*, 83(3):393, 2006.

[88] Feng Yu-Dong, Wang Zhi-Min, Ma Ya-Li, and Zhang Fu-Jia. Thin film design for advanced thermochromic smart radiator devices. *Chinese Physics*, 16(6):1704, 2007.

[89] Matthew J Dicken, Koray Aydin, Imogen M Pryce, Luke a Sweatlock, Elizabeth M Boyd, Sameer Walavalkar, James Ma, and Harry a Atwater. Frequency tunable near-infrared metamaterials based on VO2 phase transition. *Optics express*, 17(20):18330–9, 2009.

[90] Hans W. Verleur, A. S. Barker, and C. N. Berglund. Optical properties of VO2 between 0.25 and 5 eV. *Reviews of Modern Physics*, 40(4):737, 1968.

[91] M Soltani, M Chaker, E Haddad, and RV Kruzelesky. Thermochromic vanadium dioxide smart coatings grown on kapton substrates by reactive pulsed laser deposition. *Journal of Vacuum Science and Technology. A, International Journal Devoted to Vacuum, Surfaces, and Films*, 24(3), 2006.

[92] Vladimir M. Shalaev. Optical negative-index metamaterials. *Nature Photonics*, 1(1):41–48, 2007.

[93] V. G. Veselago. The Electrodynamics of Substances with Simultaneously Negative Values of ϵ and μ. *Soviet Physics Uspekhi*, 10:509, 1968.

[94] Richard A Shelby, David R Smith, and Seldon Schultz. Experimental verification of a negative index of refraction. *science*, 292(5514):77–79, 2001.

[95] Jason Valentine, Shuang Zhang, Thomas Zentgraf, Erick Ulin-Avila, Dentcho a Genov, Guy Bartal, and Xiang Zhang. Three-dimensional optical metamaterial with a negative refractive index. *Nature*, 455(7211):376–9, 2008.

[96] Henri J Lezec, Jennifer a Dionne, and Harry a Atwater. Negative refraction at visible frequencies. *Science (New York, N.Y.)*, 316(5823):430–2, 2007.

[97] Ting Xu, Amit Agrawal, Maxim Abashin, Kenneth J Chau, and Henri J Lezec. All-angle negative refraction and active flat lensing of ultraviolet light. *Nature*, 497(7450):470–4, 2013.

[98] Imogen M Pryce, Koray Aydin, Yousif a Kelaita, Ryan M Briggs, and Harry a Atwater. Highly strained compliant optical metamaterials with large frequency tunability. *Nano letters*, 10(10):4222–7, 2010.

[99] Jun-Yu Ou, Eric Plum, Liudi Jiang, and Nikolay I. Zheludev. Reconfigurable Photonic Metamaterials. *CLEO:2011 - Laser Applications to Photonic Applications*, page QThK2, 2011.

[100] Jun-Yu Ou, Eric Plum, Jianfa Zhang, and Nikolay I Zheludev. An electromechanically reconfigurable plasmonic metamaterial operating in the near-infrared. *Nature nanotechnology*, 8(4):252–5, 2013.

[101] T Driscoll, Hyun-Tak Kim, Byung-Gyu Chae, Bong-Jun Kim, Yong-Wook Lee, N Marie Jokerst, S Palit, D R Smith, M Di Ventra, and D N Basov. Memory metamaterials. *Science (New York, N.Y.)*, 325(5947):1518–21, 2009.

[102] Shumin Xiao, Uday K. Chettiar, Alexander V. Kildishev, Vladimir Drachev, I. C. Khoo, and Vladimir M. Shalaev. Tunable magnetic response of metamaterials. *Applied Physics Letters*, 95(3):033115, 2009.

[103] David Shrekenhamer, Wen-Chen Chen, and Willie J. Padilla. Liquid Crystal Tunable Metamaterial Absorber. *Physical Review Letters*, 110(17):177403, 2013.

[104] Hou-Tong Chen, Willie J Padilla, Joshua M O Zide, Arthur C Gossard, Antoinette J Taylor, and Richard D Averitt. Active terahertz metamaterial devices. *Nature*, 444(7119):597–600, 2006.

[105] Hou-Tong Chen, John F. O'Hara, Abul K. Azad, Antoinette J. Taylor, Richard D. Averitt, David B. Shrekenhamer, and Willie J. Padilla. Experimental demonstration of frequency-agile terahertz metamaterials. *Nature Photonics*, 2(5):295–298, 2008.

[106] M Trepanier, Daimeng Zhang, Oleg Mukhanov, and Steven M Anlage. Realization and modeling of metamaterials made of rf superconducting quantum-interference devices. *Physical Review X*, 3(4):041029, 2013.

[107] Daimeng Zhang, Melissa Trepanier, Oleg Mukhanov, and Steven M Anlage. Tunable broadband transparency of macroscopic quantum superconducting metamaterials. *Physical Review X*, 5(4):041045, 2015.

[108] Daimeng Zhang, Melissa Trepanier, Thomas Antonsen, Edward Ott, and Steven M. Anlage. Intermodulation in nonlinear squid metamaterials: Experiment and theory. *Phys. Rev. B*, 94:174507, Nov 2016.

[109] Daniel Franklin, Yuan Chen, Abraham Vazquez-Guardado, Sushrut Modak, Javaneh Boroumand, Daming Xu, Shin-Tson Wu, and Debashis Chanda. Polarization-independent actively tunable colour generation on imprinted plasmonic surfaces. *Nature communications*, 6, 2015.

[110] Deng-Ke Yang and Shin-Tson Wu. Fundamentals of liquid crystal devices. *John Wiley&Sons, Ltd*, 2006.

[111] Joseph Murray, Dakang Ma, and Jeremy N Munday. Electrically controllable light-trapping for self-powered switchable solar windows. *ACS Photonics*, 2016.

[112] J. W. Doane, N. A. Vaz, B.G. Wu, and S. umer. Field controlled light scattering from nematic droplets. *Applied Physics Letters*, 48(4), 1986.

[113] Joel A. Firehammer, Gregory P. Crawford, and Nabil M. Lawandy. Voltage-controlled lasing pixels for projection display. *Applied Physics Letters*, 73(5):590–592, 1998.

[114] C.M. Lampert. Large-area smart glass and integrated photovoltaics. *Solar Energy Materials and Solar Cells*, 76(4):489 – 499, 2003. Photovoltaics and photoactive materials - properties, technology and applications.

[115] Hadi Hosseinzadeh, Kelvin Liew, Yining Han, Nasser Mohieddin, and Irene a Goldthorpe. Silver nanowire transparent electrodes for liquid crystal-based smart windows. *Solar Energy Materials and Solar Cells*, 132:337–341, 2015.

[116] Hongwen Ren, Yun-Hsing Fan, Yi-Hsin Lin, and Shin-Tson Wu. Tunable-focus microlens arrays using nanosized polymer-dispersed liquid crystal droplets. *Optics communications*, 247(1):101–106, 2005.

[117] Paul S. Drzaic. *Liquid crystal dispersions*, volume 1. World Scientific, 1995.

[118] Y. Derouiche, F. Dubois, R. Douali, C. Legrand, and U. Maschke. Some properties of nematic liquid crystal E7/Acrylic polymer networks. *Molecular Crystals and Liquid Crystals*, 541(October):201–210, 2011.

[119] S. Zumer. Light scattering from nematic droplets: Anomalous-diffraction approach. *Physical Review A*, 37(10):4006–4015, 1988.

[120] J. R. Kelly and Wei Wu. Multiple scattering effects in polymer dispersed liquid crystals. *Liquid Crystals*, 14(6):1683–1694, 1993.

[121] Jack Kelly, Wei Wu, and Peter Palffy-muhoray. Wavelength Dependence of Scattering in PDLC Films: Droplet Size Effects. *Molecular Crystals and Liquid Crystals Science and Technology. Section A. Molecular Crystals and Liquid Crystals*, 223(1):251–261, 1992.

[122] Goulette, Charles D. Howardand, and Michael W. Davidson. Infinity optical systems. http://www.microscopyu.com/articles/optics/cfintro.html. Accessed: 2016-05-04.

[123] Rudi Rottenfusser, Tadja Dragoo, and Michael W. Davidson. Basic principles of infinity optical systems. http://zeiss-campus.magnet.fsu.edu/tutorials/basics/objectivemagnification/indexflash.html. Accessed: 2016-05-04.

[124] Sidney A. Self. Focusing of spherical gaussian beams. *Appl. Opt.*, 22(5):658–661, 1983.